

3D Bioprinting of Complex Cellular Alignment through Pre-aligned Anisotropic Microtissues

A DISSERTATION
SUBMITTED TO THE FACULTY OF
UNIVERSITY OF MINNESOTA
BY

Caleb Darwin Vogt

IN PARTIAL FULFILLMENT OF THE REQUIREMENTS
FOR THE DEGREE OF DOCTOR OF PHILOSOPHY

ADVISED BY

Angela Panoskaltis-Mortari, Ph.D.

July 2023

© Caleb D. Vogt 2023

Acknowledgments

If all the individuals who deserved my thanks were listed here, I could very well run out of pages. There were many along the way to starting this training program without whom I would not have produced this work. I want to first thank my family and friends for sticking with me, despite the long hours and missed events. Thanks to my undergraduate advisor Dr. Feng Zhao for accepting me into her tissue engineering lab and helping me begin this journey.

Thanks to my advisor, Dr. Angela Panoskaltis-Mortari, for her guidance and enthusiasm for both my project and development as a physician-scientist. I wanted to take on an ambitious project when I joined the lab, and she struck a balance between giving me the freedom to develop the many tools and techniques required to accomplish my goals and providing a critical feedback source on the impact and rigor of my work. This project has taken many years and setbacks to finally reach the point of implementation, and I appreciate the patience and unwavering support she provided. The training in professional activities including lecturing, leading a lab course, applying for patents, managing research funds, and applying for numerous grants has contributed greatly to a unique and rich experience during my training.

Many thanks to the members of the lab and the 3D bioprinting facility, without whom this work would have been significantly more work and much less enjoyable. Dr. Zach Galliger and Dr. Iffy Akinnola were important mentors who were always ready to weigh in on my experimental plans, commiserate about the challenges of graduate school, and generally keep the spirits of the whole lab high. Dr. Steve Skolasinski helped me learn what to expect as I move forward with my medical training and was a great example of a physician-scientist who could enjoy life even during the long hours of advanced clinical training. As a medical student, Dr.

Madison Ernst quickly picked up on techniques and was instrumental in gathering preliminary data required for planning this work, and I thank her for her patience and hard work even when we did not have a clear path forward. There are a series of researchers who acted as managers of the lab, bioprinting facility, or both. All of them contributed to this work by keeping the place running, training me in new techniques, and generally being great co-workers who I will miss seeing regularly. Carolyn Meyer taught me most of the techniques that I have applied in developing this work and had a seemingly inexhaustible amount of patience for training lab members, no matter how busy she was. Daniel Sorby, Haylie Helms, and Jenae Putnam always kept the bioprinters running smoothly and were great to work with when I had new techniques I wanted to apply. Kyleigh Pacello has been a great help keeping the facility running through a lab move, equipment malfunctions, and managing cell cultures for me when I had to direct my focus elsewhere, and this work would not have progressed nearly as far as it has without her involvement. Thanks to Joe Broomhead, who joined the lab at just the right moment as I was finalizing the methods for microtissue production and printing and has been a critical resource in collecting the final data and learning the new techniques presented in this work to continue its future development. Thanks to Sid Yelwande for his efforts to find additional uses for the tissue fibers that we use in our work; it has been exciting to see these new possibilities take form. Finally, thanks to Anthony Vitale and Alex Paulsen for all the after-hours work they put in developing the next generation of the fiber spooling system.

Thanks to our collaborators in the Department of Thoracic and Foregut Surgery, Dr. Rafael Andrade and Dr. Ilitch Diaz-Gutierrez for their mentorship and support of my work through grant applications and guidance in integrating tissue engineering with surgery.

Thanks to the Medical Scientist Training program's leadership, staff, and students for the many and varied types of support provided throughout my first 7 years of training as a physician-scientist. Through this program, I am getting closer to the dream I had as an undergraduate engineer to a career applying creativity and compassion to develop new technology for patient care. Dr. Yoji Shimizu and Dr. Peter Bitterman in particular have helped me especially through grant support and providing research opportunities through the pre-MSTP program here. Many thanks to Susan Shurson and Nick Berg for always making sure the many moving parts required for this training program were meshing smoothly. I am looking forward to the next two years of clinical training.

Thanks to the Department of Biomedical engineering, whose professors and staff have worked with me through the added complexity of dual-degree training. Thanks especially to members of my committee, Dr. Pat Alford, Dr. David Wood, and Dr. Alena Talkachova, for their training through my coursework and their advice and oversight during my research. My additional thanks to Dr. Daniel Garry for his insights and review of my work as a faculty member from the Integrative Biology and Physiology program and member of my committee.

Thanks to the University of Minnesota's Visible Heart Lab for supplying research materials and tissues. Especially thanks to Renee Brigham and David Ramirez for their conversations and help coordinating.

I will express my deepest gratitude to the individuals who donated their bodies to the University of Minnesota's Anatomy Bequest Program for the advancement of education and research. Thanks to Dr. Anthony Weinhaus at the University of Minnesota for his help in planning the anatomical imaging.

Many thanks to Bonnie VanHeel and Dr. Alex Fok in the Minnesota Dental Research Center for Biomaterials and Biomechanics for their help with microCT evaluation of 3D printed constructs in this work.

Parts of this work were carried out in the Polymer Characterization and Processing Facility. Thanks especially to David Giles for his training and experimental support with the rheometry of bioinks and hydrogels.

Portions of this work were conducted in the Minnesota Nano Center, which is supported by the National Science Foundation through the National Nanotechnology Coordinated Infrastructure (NNCI) under Award Number ECCS-2025124. Many thanks to the scientists there whose training on photolithography and associated techniques was important to my preliminary work.

This work was supported by the resources and staff at the University of Minnesota University Imaging Centers (UIC). SCR_020997. I would especially like to thank Dr. Guillermo Marques, Dr. Mary Brown, and Patrick Willey for their insights and training.

This work was supported by the NHLBI, the NIBIB, and the NIGMS of the National Institutes of Health under award numbers T32HL007741, R21EB022830, and T32GM008244 (MSTP grant). Additional support was provided through the University of Minnesota through the Doctoral Dissertation Fellowship award and the Office of Technology Commercialization Early Innovation Fund award.

Dedication

To my wife, Nina, without whose support, this would not have been possible.

Abstract

The gastroesophageal junction, where the esophagus empties into the stomach, is a unique structure in the body that presents a challenge to current tissue engineering processes. In addition to the common requirements of vascularization, innervation, and precise positioning of multiple types of cells, the muscular structure itself is highly complex in its alignment of smooth muscle bundles. Although much progress has been made in engineering the alignment of muscle cells in single directions, reconstituting structures of the complexity found in the gastroesophageal junction has not been demonstrated. This work provides a review of the gastroesophageal junction from the tissue-engineering perspective and presents a novel 3D bioprinting technique that could one day address this muscle alignment issue.

Table of Contents

| | |
|---|-----|
| Acknowledgments..... | i |
| Dedication..... | v |
| Abstract..... | vi |
| Table of Contents..... | vii |
| List of Tables..... | x |
| List of Figures..... | xi |
| Conflict of Interest Disclosures..... | xii |
| 1 Introduction..... | 1 |
| 2 Considerations for Tissue Engineering of the Gastroesophageal Junction..... | 5 |
| 2.1 Clinical Significance..... | 5 |
| 2.2 Embryology..... | 7 |
| 2.3 Anatomy and Histology..... | 10 |
| 2.3.1 Histology..... | 10 |
| 2.3.2 Vascular Anatomy..... | 12 |
| 2.4 The Reflux Barrier..... | 14 |
| 2.4.1 Lower Esophageal Circular Sphincter..... | 14 |
| 2.4.2 Upper Gastric Sphincter..... | 15 |
| 2.4.3 Gastroesophageal Flap Valve..... | 15 |
| 2.4.4 Crural Diaphragm and Phrenoesophageal Ligament..... | 16 |
| 2.5 Neuromuscular Physiology..... | 18 |
| 2.5.1 Swallowing-Associated Relaxation..... | 20 |
| 2.5.2 Transient Lower Esophageal Sphincter Relaxations, Belching, and Vomiting..... | 21 |
| 2.6 Mechanical Properties..... | 22 |
| 2.7 Tissue Engineering Progress..... | 24 |
| 2.7.1 Lumen Patency..... | 26 |
| 2.7.2 Scaffolds..... | 27 |
| 2.7.3 Vascularization..... | 27 |
| 2.8 Conclusion..... | 28 |
| 3 Modalities and Materials for Tissue Engineering the Stomach and Esophagus..... | 35 |
| 3.1 Introduction..... | 35 |
| 3.2 Tissue Engineering Modalities..... | 36 |
| 3.2.1 Decellularized Scaffolds..... | 37 |
| 3.2.2 Engineered Meshes and Films..... | 37 |

| | | |
|-------|---|----|
| 3.2.3 | 3D Printing..... | 39 |
| 3.2.4 | 3D Bioprinting | 40 |
| 3.3 | Human Trials | 42 |
| 3.4 | Future Perspectives on the GEJ | 43 |
| 3.5 | Conclusion | 45 |
| 4 | State of 3D Bioprinting for the Esophagus and Hollow Muscular Organs..... | 49 |
| 4.1 | 3D Bioprinting Methodologies | 49 |
| 4.1.1 | Extrusion bioprinting | 50 |
| 4.1.2 | Droplet Jetting bioprinting | 50 |
| 4.1.3 | Laser Transfer bioprinting | 51 |
| 4.1.4 | Selective Photopolymerization bioprinting..... | 53 |
| 4.2 | Esophagus | 54 |
| 4.3 | Stomach, Intestines, and Bile ducts: | 56 |
| 4.4 | Ureter, Urethra, and Bladder:..... | 57 |
| 5 | Approaches for Microtissue Production | 63 |
| 5.1 | Introduction..... | 63 |
| 5.2 | Materials and Methods..... | 63 |
| 5.2.1 | Microscale Molding Approach | 63 |
| 5.2.2 | Mesoscale Molding Approach | 65 |
| 5.2.3 | Cast Microtissue Development..... | 66 |
| 5.2.4 | Nuclear Alignment..... | 66 |
| 5.2.5 | Wet Spinning Approach..... | 67 |
| 5.2.6 | Wet Spinning Rheology | 67 |
| 5.2.7 | Mechanical Testing for Fibers | 67 |
| 5.3 | Design Calculations | 68 |
| 5.4 | Results and Discussion | 69 |
| 5.4.1 | Casting Methods Experience | 69 |
| 5.4.2 | Casting Nuclear Alignment..... | 71 |
| 5.4.3 | Wet-Spinning Approach | 71 |
| 5.4.4 | Fiber Strength..... | 72 |
| 5.4.5 | Handling of Wet-Spun Fibers | 72 |
| 5.5 | Conclusion | 74 |
| 6 | 3D Bioprinting with Pre-Aligned Microtissues | 82 |
| 6.1 | Introduction..... | 82 |

| | | |
|--------|---------------------------------------|-----|
| 6.2 | Materials and Methods..... | 84 |
| 6.2.1 | Cell Culture..... | 84 |
| 6.2.2 | Microfluidic Spinning Device..... | 84 |
| 6.2.3 | Microtissue production | 85 |
| 6.2.4 | Unaligned Controls | 87 |
| 6.2.5 | Immunofluorescence Microscopy..... | 87 |
| 6.2.6 | Cell Viability..... | 88 |
| 6.2.7 | Bioink Formulation..... | 89 |
| 6.2.8 | Rheometry..... | 89 |
| 6.2.9 | 3D Bioprinting | 90 |
| 6.2.10 | Cell and tissue alignment | 91 |
| 6.2.11 | Statistical Analysis..... | 91 |
| 6.3 | Results..... | 92 |
| 6.3.1 | Spinning Device Characteristics | 92 |
| 6.3.2 | Fiber Shell and Core Properties | 93 |
| 6.3.3 | Fiber Spinning Parameters | 93 |
| 6.3.4 | Morphology in Cellular Fibers..... | 94 |
| 6.3.5 | Effect of Cutting on PAMs | 94 |
| 6.3.6 | 3D Bioprinting with PAMs..... | 95 |
| 6.4 | Discussion..... | 96 |
| 6.5 | Conclusion | 100 |
| 7 | Conclusion | 111 |
| 8 | References..... | 116 |

List of Tables

| | |
|---|----|
| Table 3-1. Applications of decellularized materials in gastric and esophageal tissue engineering | 46 |
| Table 3-2. Applications of synthetic fiber, film, and mesh materials in gastric and esophageal tissue engineering..... | 47 |

List of Figures

| | |
|--|-----|
| Figure 1-1: Tissue Engineering Paradigm for Patient Treatment | 4 |
| Figure 2-1: Development of the GEJ | 30 |
| Figure 2-2: Normal Histology and Gross Anatomy of the GEJ | 32 |
| Figure 2-3: Gastroesophageal High Pressure Zone Illustration. | 33 |
| Figure 2-4: Esophageal Manometry..... | 34 |
| Figure 4-1: Common Bioprinting Methods. | 61 |
| Figure 4-2: Methods of 3D Bioprinting and Biofabrication of Hollow Organs..... | 62 |
| Figure 5-1. Casting Method for Microtissue Production. | 76 |
| Figure 5-2. Nuclear Alignment of Cast Mesoscale Tissues..... | 77 |
| Figure 5-3. Drawing of Microfluidic Spinning Device..... | 78 |
| Figure 5-4. Fiber Spinning and Spooling Setup..... | 79 |
| Figure 5-5. Cell Concentration Optimization in "Harp" Molded Tissues..... | 80 |
| Figure 5-6. Wet Spinning Fluid and Solid Properties..... | 81 |
| Figure 6-1: Method for production and bioprinting of PAMs | 101 |
| Figure 6-2: Characteristics of the Fiber Spinning System. | 103 |
| Figure 6-3: Cell alignment and protein expression. | 104 |
| Figure 6-4: Properties of the PAMs after processing..... | 106 |
| Figure 6-5: Alignment of Bioprinted PAMs | 107 |
| Figure 6-6: Cell and Collagen Concentration Effect on Fiber Morphology. | 108 |
| Figure 6-7: Cutting PAMs and Combining with Bioink..... | 109 |
| Figure 6-8. Original images of phalloidin-labeled 3D bioprinted constructs. | 110 |

Conflict of Interest Disclosures

Portions of this work related to the production and application of pre-structured microscale tissues, as well as other methods of generating aligned engineered tissues, are the subject of provisional and full patent applications, including US20220064603A1.

1 Introduction

The field of tissue engineering has developed to encompass endeavors to recreate biological tissues with the goals of disease modeling, drug testing, and direct patient treatment. It is hoped that eventually the field will one day provide a source for replacement tissues and organs which will make the need for organ donation and transplantation obsolete. A common understanding for organizing the research is that tissues are fundamentally composed of three components: cells, scaffold, and signals. This “tissue engineering triad” continues to serve as an important conceptual guide in approaching problems. Scaffolding materials in particular have been an area of rapid development. The structural role of the extracellular matrix is often provided by a combination of natural and synthetic polymers, frequently in the form of a hydrogel. Within this supplied matrix, cells can interact with each other and degrade or reorganize the scaffold material to develop from a loose collection of spherical, singular cells into a structured tissue.

A significant step forward came with the development of induced pluripotent stem cells (iPSCs), which are differentiated adult cells (frequently skin fibroblasts) that are reprogrammed by a series of factors to revert to a pluripotent state [1]. Various adult lineages have been reconstituted from these reprogrammed cells, providing a potential source for patient-specific cells. This allows for individualized disease modeling and drug testing for patients, but also can address the problem of transplant rejection. If patient tissues or organs can be reconstructed from the patient’s own cells, the risk of the immune system reacting negatively towards the implant is minimized and immunomodulatory drug therapies, which are associated with significant morbidity and mortality, can be avoided. Another problem potentially solved by iPSCs is the challenge associated with culturing adult differentiated cells. These primary cells often do not

proliferate well in traditional cell culture. For example, human smooth muscle cells frequently stop dividing after only a few population doublings. Stem cells are proliferative by nature, and if provided with the correct stimuli, it is expected that expansion of the stem cell or transit-amplifying cell populations after iPSC reprogramming could generate the hundreds of millions of cells frequently found in a single cubic centimeter of human tissue. This has led to the paradigm shown in Figure 1-1 for the eventual replacement of diseased organs with patient derived, tissue-engineered substitutes.

A key challenge in tissue engineering is the organization of cells within tissues. Especially in the case of mechanically active cells, the way the cells are oriented and the structure of the extracellular matrix provides stability and functionality to the tissue. Muscle tissues are an example of this. Skeletal muscle cells are long, thin cells which shorten when they contract, generating force along the long axis of the cells. In skeletal muscle tissue, the cells are generally aligned in a parallel manner such that the micronewton forces generated by each cell are summed and macroscale deformation of the muscle is achieved. Similarly, cardiac and smooth muscle tissues have alignment necessary for changing the tissue shape to pump blood or push contents through the digestive tract. The challenge of aligning cells begins with the fact that cell culture in tissue engineering processes involves releasing the cells from their growth surface, such as a flask or petri dish, resulting in the cells taking on a spherical shape with no directionality. If these spherical cells are seeded onto a new growth surface or into a hydrogel material without guidance cues, uncontrolled alignment is often the result. Because of the importance of the alignment of cells within tissues, replicating this alignment has been a focus of many recent efforts in tissue engineering.

Much of the progress made in aligning cells has been effective in achieving uniaxial alignment. Muscle cells especially are known to align on surface cues or under stress. Surface cues can be patterns of adhesive proteins on a petri dish surface, or microgroove geometries which the cells may follow [2]. The cells may align in the direction of stretch if the substrate to which they are adhered is deformed, so long as the deformation is of a suitable amplitude and frequency [3]. Finally, muscle cells may be grown in a manner where the tissue boundaries are constrained along one axis, which results in cells aligning along this axis of increased resistance[4], [5]. While these methods for unidirectional alignment are useful in tissues like skeletal muscle, organs of the digestive and circulatory system require a more sophisticated approach. The gastroesophageal junction GEJ is the anatomical valve between the esophagus and the stomach responsible for allowing one-way passage of food into the stomach. This is accomplished by a complex set of smooth muscle bundles, which wrap around the outer walls of the junction in multiple planes and directions of cellular alignment. Achieving this type of structural complexity has previously been beyond the capability of tissue-engineering.

Here, a new method for tissue engineering of complex muscle cell alignment is presented. It is applied in the context of engineering the GEJ, as this type of muscular structure represents one of the most difficult to create. Furthermore, the GEJ has received little attention in the field despite the potential clinical implications of new treatments to affect millions of reflux disease and cancer patients worldwide. This method is a combination of techniques, which combines an approach to create unidirectionally aligned smooth muscle microtissues with a 3D bioprinting strategy to deposit these pre-aligned microtissues in macroscale alignment with each other. The result is a new tool for direct writing of complex muscle alignment which could be applied from the most challenging geometries found in the GEJ or the heart down to the simplest unidirectional alignments found in skeletal muscle.

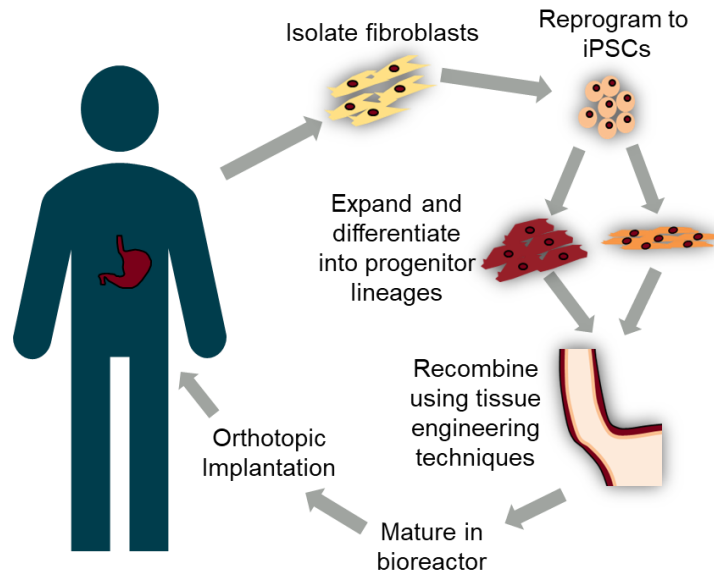


Figure 1-1: Tissue Engineering Paradigm for Patient Treatment

A theoretical process by which a replacement gastroesophageal junction could be produced from patient-derived iPSCs for direct treatment following surgical resection of the diseased tissue.

2 Considerations for Tissue Engineering of the Gastroesophageal Junction

The following chapter contains elements published in 2020 in the Journal of Tissue Engineering and Regenerative Medicine. The included material was authored wholly by Caleb D. Vogt.

Vogt, C. D., & Panoskaltsis-Mortari, A. (2020). Tissue engineering of the gastroesophageal junction. Journal of Tissue Engineering and Regenerative Medicine, 14(6), 855–868. <https://doi.org/10.1002/term.3045>

2.1 Clinical Significance

The gastroesophageal junction (GEJ) is of significant clinical interest due to its role in many disease processes. It is defined in surgical anatomy by the Z-line, a distinct transition where esophageal mucosa ends and the gastric mucosa begins. The junction contains muscle fibers from the esophagus and the stomach, which are arranged to provide the junction with a sphincteric function. Thus, the GEJ is sometimes referred to as the Lower Esophageal Sphincter (LES). For clarity throughout this review, the GEJ refers to the anatomical region and the LES refers to the anatomical structures which contribute to this barrier function. In normal physiology, the LES allows solids and liquids to pass from the esophagus and into the stomach without allowing stomach contents to reflux upward into the esophagus. As such, the LES is analogous to a one-way valve. While this anti-reflux function is the most clinically relevant role, coordinated relaxations that allow for vomiting or belching are important in normal physiology. Diseases involving the GEJ typically interfere with, or are a result of failure of, the valve function. Esophageal achalasia is a disease in which the LES fails to relax, limiting movement of food into

the stomach. Other examples of such pathologies are distal esophageal spasm, jackhammer esophagus, and esophago-gastric outflow obstruction [6]. These diseases are fairly uncommon, with achalasia having an incidence of only 1 in 100,000 [7].

Problems with the anti-reflux function of the LES, however, are much more prevalent. Gastroesophageal Reflux Disease (GERD) is a condition in which acidic stomach contents rise up into the esophagus, damaging the esophageal mucosa. The esophagus is lined with stratified squamous epithelium and few glands, unlike the gastric epithelium with its simple columnar structure and plentiful mucinous glands. As a result, the esophagus is not well-suited for acid exposure, and erosion of the esophageal epithelium can ensue. This can lead to the classic symptom of heartburn. Other associated symptoms of an incompetent LES are excessive belching and regurgitation. Years of frequent acid exposure can lead to intestinal metaplasia (Barrett's Esophagus), in which the epithelium converts its phenotype to simple columnar with glands in a physiological response to protect against the caustic fluid. This metaplastic change is reversible, but is associated with increased risk of conversion to pathological dysplasia and further progression to carcinoma, according to the classic sequence seen in many epithelial cancers. GERD has an estimated prevalence of over 18% in North America, with roughly 15% of patients showing progression to Barrett's esophagus or cancer [8], [9]. In many cases of lower esophageal or GEJ cancer, surgical resection is the standard of care [10]. Gastric pull-up is the method most frequently used to reconstruct the esophagus and close the surgical defect where the cancer was removed [11]. With the LES removed, there is nothing preventing stomach contents from refluxing upward. Because this would be detrimental to any remaining esophageal tissue, part of the stomach is formed into a tube and is attached to the remaining healthy esophagus high in the thoracic cavity. While having a large portion of the lower esophagus replaced with an acid-resistant stomach tube can help reduce recurrence of esophageal injury or cancer, other issues

persist. Patients who have had esophagectomy or who have very poorly controlled GERD are at increased risk for life-threatening aspiration pneumonia and other lung pathologies, with over 25% of patients experiencing pulmonary problems after surgery [12]–[14]. Other complications can include anastomotic leaks, strictures, or loss of normal flow mechanics through the upper gastrointestinal system [10]

An ideal solution would be to remove the tumor and replace the valve, allowing surgeons to leave as much native esophagus in place as possible. The field of tissue engineering is making steady progress in addressing challenges with vascularization of thick tissue constructs and sourcing patient-specific cells through induced pluripotent stem cells (iPSC) and adult progenitor cells. Progress is also being made in innervation to establish physiologic control over contractile tissues and incorporate neural progenitors into gut organoids [15], [16]. Tissue engineering attempts for treating defects in the esophageal body have been successful to the point of running early clinical trials [17]–[21]. Thus, a tissue engineering approach is promising for rebuilding the gastroesophageal junction. This review covers pertinent points including embryological development, adult anatomy and physiology, and insights from recent progress in tissue engineering of the esophagus and stomach.

2.2 Embryology

Understanding the embryological development of the esophagus and stomach is useful from an engineering perspective for informing choices of cells, signaling factors, and reactor conditions to harness the existing programming already within cells. Early in embryogenesis there exists a structure known as the trilaminar disc, which is made of three germ layers. These layers are the ectoderm, mesoderm, and endoderm. The trilaminar disc begins to fold into two concentric tubes during the third week. First, the mesoderm divides into two layers, one attached to the ectoderm

and one to the endoderm. The layer joined to the endoderm will develop into the visceral muscle and connective tissue, while the layer of mesoderm remaining with the ectoderm will form the bones and muscles of the body wall. The endoderm, which is now the inner layer of the gut tube, gives rise to the epithelium and associated glands in the mucosa and submucosa of both the gastrointestinal and respiratory tracts. While all this motion is occurring, ectodermal cells migrate from the vagal neural crests to the developing foregut to form the enteric nervous system (ENS) [22] (Figure 2-1A). These cells move as a wave pulled forward by glial derived neurotrophic factor (GDNF) signaling, and leave behind cells which will form the ENS [23]. Thus, substantial contribution from each of the germ layers is required for normal foregut development (Figure 2-1C).

At weeks 7-8, the developing intestines herniate physiologically into the yolk sac, perform a 270° twisting rotation, and retract into the peritoneal cavity, leading to the tortuous path seen in normal adult anatomy. This process is associated with a 90° clockwise rotation of the stomach, GEJ, and lower esophagus on the craniocaudal axis (Figure 2-1B). This rotation places the originally dorsal part of the stomach facing leftward, and the dorsal mesentery is brought forward to create the lesser omentum. The left and right trunks of the vagus nerve, which run along the esophagus, become anterior and posterior to the esophagus, respectively.

The symphony of signals which cause differentiation of the stem cells of the three germ layers and eventually lead to the formation of specialized tissues in the esophagus are still being studied. However, there are certain high-yield pathways which are worth mentioning for a more complete understanding of the development of both the stomach and esophagus. Researchers focus on the following three coordinate axes when discussing esophagus development: the

craniocaudal axis going from the head to the feet, the anteroposterior axis, and the radial direction from inside the gut lumen outward through the mucosa and muscle layers.

The craniocaudal specification of the parts of the gut tube that develop into the esophagus and stomach are in part determined by a gradient of retinoic acid (RA), which is at a low concentration near the mouth and increases to a high concentration near the cloaca [24]. The concentration of RA may help to determine the expression of many transcription factors, such as those encoded by homeobox (HOX) and parahomeobox genes [24], [25]. These master control genes are expressed in spatial sequence down the craniocaudal axis to specify the order of organs and their relationship to each other [26], [27]. Another broad pattern is the general Wnt antagonism in the foregut, with the exception of tracheal bud formation and development of the gastric fundus [28], [29]. This Wnt patterning is consistent with Sox2 expression in the foregut and Cdx-1 and Cdx-2 expression in the midgut and hindgut [28], [30]. Ectopic Sox2 expression induces stomach-like differentiation in intestinal epithelium in embryonic mice, demonstrating its importance in epithelial specification of the foregut [31].

Some of the signals that are important for delineation between the esophagus and the stomach at the GEJ are known, although it is still an active area of study. Communication between the mesenchyme and the endoderm seems to play a role in development of the squamocolumnar junction. This has been demonstrated in mouse embryos. *Hoxa5* is produced by the mesenchyme, which allows for patterned expression of the transcription factors Sonic Hedgehog (Shh) in the esophageal-like epithelium and Indian Hedgehog (Ihh) in the columnar stomach epithelium [32]. The transcription factors *Gata4* and *Pdx1* help to define the distal stomach and gastroduodenal junction and are not expressed in the GEJ [32], [33].

Radial patterning of the esophagus and stomach may be directed by a gradient of Shh. An early study with chick embryos showed that Shh could inhibit smooth muscle differentiation of nearby mesenchyme, presumably leading to development of the mucosa and submucosa while allowing muscle differentiation in the outer layers [34]. This was challenged by a more recent study in mice, however, where no smooth muscle inhibition was found [35]. Rather, the closely-related Ihh was important for muscle differentiation. Thus, it seems that hedgehog signaling in mammals is important for normal development of the muscularis externa. This is strengthened by the finding that normal smooth muscle development is dependent on the Cdo (Cell adhesion molecule-related/down-regulated by oncogenes) surface receptor, which is a co-receptor for Hedgehog signaling. Without Cdo, smooth muscle fascicles in the lower esophagus cannot achieve proper alignment in mice [36]. Proper organization of the lower esophagus also appears to depend on normal differentiation and proliferation of skeletal muscle cells found in the upper half of the esophagus [37], [38].

2.3 Anatomy and Histology

2.3.1 Histology

The esophagus and stomach share the same general structure as the rest of the gastrointestinal tract, with specialized epithelia surrounded by layers of muscle (Figure 2-1C). The esophageal epithelium in humans consists of non-keratinizing stratified squamous epithelium resting on a basement membrane. Stratified squamous epithelium is consistent with the mechanical function of the esophagus, as it is protective against abrasion from a bolus of food moving through the narrow esophageal lumen. The deepest layer of the epithelium has a basal cell layer of stem cells, which divide asymmetrically and move upward, differentiating into a squamous phenotype as they rise. The basement membrane has a papillary structure similar to that found in the dermis of

the skin, with stem cells in the valleys between the papillae and transit-amplifying cells on the papillary peaks [39], [40]. Under this basement membrane is a loosely organized lamina propria and a muscularis mucosa. The epithelium is occasionally interrupted by the lumen of a submucosal esophageal gland [41]. Near the junction with the stomach, the esophagus also has mucosal glands, which secrete mucous for acid protection. At the z-line, there is a sharp transition between esophageal and gastric cardiac epithelium. The gastric cardia has simple non-ciliated columnar epithelium and is considered a transition zone between the esophagus and the acid-producing stomach. It is defined histologically as a region with only cardiac glands, which protect the stomach epithelium from acid by releasing mucous [42]. The epithelium is perforated with gastric pits, which are lined with columnar cells and extend into the submucosa. Foveolar cells, which are goblet cells that store and release globules of protective mucous, are the dominant cell type. In humans, the average length of the cardiac region is about 7mm [42]. It must be noted that there is an ongoing question as to whether gastric cardiac epithelium is physiologic or a metaplastic adaptation following years of acid insult. [43], [44].

Deep to the epithelial basement membrane lies the lamina propria and a thin layer of muscle known as the muscularis mucosa. The esophageal submucosa contains blood vessels organized into a network known as Heller's plexus. It also contains lymphoid tissue, glands, and the neural tissue of the submucosal (Meissner's) plexus. The stomach submucosa is structured similarly. Below the submucosa lies the muscularis externa, which has two layers in the esophagus but three layers in the stomach.

Although there is skeletal muscle tissue in the proximal esophagus, the distal esophagus and stomach in humans only contains smooth muscle. In the esophagus, inner layer fascicles are arranged circumferentially and spiral about the lumen, while the outer layer is oriented

longitudinally [45]. For these reasons, they are referred to as the inner circular muscle (ICM) and outer longitudinal muscle (OLM). These arrangements are not perfectly circular or longitudinal, as wave-like patterns can be observed in either layer. Between these two muscle sheets is the neural tissue of the myenteric (Auerbach's) plexus. The combination of the myenteric and submucosal plexuses is known as the enteric nervous system (ENS), with the submucosal plexus controlling secretory functions and the myenteric plexus coordinating gross motor function. The stomach has an additional innermost muscle layer between the ICM and the submucosa, which is known as the oblique layer. The myenteric plexus of the stomach is still located between the ICM and the OLM. Finally, the outermost fibro-fatty layer of the esophagus is the adventitia, which contains larger blood and lymphatic vessels. The stomach, which is an intraperitoneal organ, is covered with a tunica serosa rather than adventitia. The tunica serosa secretes a lubricating serous fluid to reduce friction between the abdominal organs.

2.3.2 Vascular Anatomy

Vascularization is vital to healthy tissue, and an understanding of the macroscopic and microscopic vessels which bring blood to the gastroesophageal junction is important for planning tissue-engineered approaches. The native arterial vasculature of the gastroesophageal junction arises from the esophageal and cardiac branches of the left gastric artery, which in turn arise from the celiac trunk on the abdominal aorta [46]. The esophageal and cardiac vessels branch into distributing arteries which run within the serosal and adventitial layer and are continuous proximally with a vascular network surrounding the body of the esophagus, which is fed by other arteries in the thorax. Recent endoscopic and histological studies have yielded insight into the microvascular structure within the GEJ tissue [47]. The distributing vessels outside of the muscularis externa divide into perforating arteries, which dive through the muscle layers to

provide muscular capillary beds and to reach the submucosa. A submucosal vascular plexus runs throughout this layer, and feeds vessels known as inter-papillary capillary loops which extend upward into the mucosa [47]. Within the mucosal layer there are vessels known as inter-papillary capillary loops, which extend upward from a sub-endothelial capillary network [47].

The venous system is interesting in that it drains into both the systemic vascular system and the portal system, which collects blood from the gut and sends it to the liver for processing. Drainage begins at the inter-papillary capillary loops of the mucosa, as well as at other capillary beds in the muscularis externa. Venules combine into larger vessels as they become a network in the submucosa known as the subepithelial plexus [46], [47]. Veins continue to combine as they move outward through the tissue layers, eventually joining a venous network running within the serosal and adventitial layers. Drainage of this network to the systemic system is largely through the azygous vein, leading to the superior vena cava. [48]. The connection to the portal system made through the esophageal branch of the left gastric vein, as well as the short gastric veins connecting to the splenic vein [46]. The venous system in this region is clinically significant because of the varices, or distension of the veins in the subepithelial plexus, which can form if hypertension develops in the portal system. The hypertension leads to a "backup" of blood through the left gastric vein and into the veins of the esophagus and GEJ. If the veins become over-distended and rupture, life-threatening bleeding can ensue. As such, tissue engineers designing a vascular system in this region should consider carefully which veins to drain to and what the pressure and flow characteristics should be to avoid overloading the venous vasculature.

The final component of fluid transport within the tissue at the GEJ is the lymphatic system. Because the GEJ is a non-absorptive region of the gastrointestinal tract, the lymphatic vasculature simply serves to remove excess extracellular fluid and monitor the tissue for insults

requiring an immune response. Lymphatics begin as capillaries within the mucosa or submucosa and combine into larger vessels as they progress outward through the gastroesophageal musculature [45]. Larger lymphatic vessels run along the length of the esophagus and drain into the left gastric, celiac, and phrenic nodes. This anatomy is of great interest to surgeons when esophageal junction cancer is detected, as metastasis through the lymphatics to these nodes may necessitate lymphadenectomy [49]. The edema-limiting role of lymphatics within the esophagus is not specifically known to be of clinical relevance. In theory, however, loss of lymphatic drainage through trauma or occlusion could cause swelling and decreased functionality of tissue in the GEJ. Therefore, tissue engineers should consider how interstitial fluid pressure is controlled within their design.

2.4 The Reflux Barrier

The reflux barrier at the GEJ is made of four distinct units. These units and their contribution to the physiology have been the source of some debate over the past few decades, but recent advances in imaging modalities and close examination of clinical correlations are bringing the field closer to a unified understanding. It has been proposed that the sum of these units be referred to as the Gastro-Esophageal Junction High-Pressure Zone (GEJHPZ) [50]. The proposed components are the Lower Esophageal Circular Muscle Sphincter (LECS), the Upper Gastric Sphincter (UGS), the Crural Diaphragm with its phrenoesophageal ligament, and the Gastroesophageal Flap Valve (GEFV). [50], [51]

2.4.1 Lower Esophageal Circular Sphincter

The LECS is a ring of smooth muscle just proximal to the gastroesophageal junction [52] (Figure 2-3). This component was previously presumed to exist as a ring of thickened, tonically contracted smooth muscle similar to that found in the pylorus. Some anatomical studies showed

thickening of the circular muscle in the distal esophagus [53]. Furthermore, a manometric study selectively paralyzing skeletal and smooth muscle components of the GEJHPZ showed a distinct pressure peak proximal to the peak created by the UGS in the absence of diaphragm contraction [50], [54]. This indicates that there is a ring of tonically contracted smooth muscle located within the region of the phrenoesophageal ligament that is distinct from any gastric muscle fibers. However, recent studies with 3D diffusion tensor imaging (porcine model) and with optical sectioning microscopy (human) provide evidence that there is not a distinct sphincter but rather a loop of smooth muscle fascicles continuous with the sling fibers coming from the stomach [55], [56].

2.4.2 Upper Gastric Sphincter

While the exact structure of the LECS is still debated, there is little doubt about the presence and importance of the intrinsic gastric fascicles forming the UGS [50]. Gastric sling fibers are proposed to be continuous with the innermost oblique layer of the stomach, starting low on the lesser curvature and wrapping up around the esophagus to return to the lesser curvature [57]. These fascicles are opposed on the proximal part of the lesser curvature by gastric clasp fibers, which appear to attach into the oblique sling fibers [56]. The combination of clasp and sling fibers is sometimes referred to as the Collar of Helvetius. As mentioned above, the most recent understanding is that the LECS is actually formed by a continuation of the sling fibers, which cross at the angle of His and loop around the esophagus (Figure 2-3).

2.4.3 Gastroesophageal Flap Valve

The gastroesophageal flap valve (GEFV) is a protrusion inside the GEJ created by the acute angle between the esophagus and the cardia of the stomach (Figure 2-3). It lies on the right side of the GEJ, and it serves as a one-way valve helping to prevent back-flow. The external angle is known

as the angle of His, and generally a more acute angle correlates with a more pronounced flap valve. MRI studies have shown that a large meal expanding the stomach's fundus could make the flap valve more effective [58]. The valve is also affected by the respiratory cycle [58], [59]. During inhalation, the left dome of the diaphragm presses down on the fundus, decreasing the acuity of the angle of His [58], [59]. Expiration allows the angle to reach maximal acuity, thus increasing the flap valve's effectiveness [58], [59]. Clinical relevance of the flap valve can be found in assessment of hiatal hernias, which is when part of stomach is forced upward through the diaphragm via the esophageal hiatus. These hernias are strongly associated with GERD, since the displacement can change the angle of His. The GEFV can be viewed endoscopically and graded by the Hill classification to assess severity [60]. If the flap is decreased by the altered orientation of the stomach, retroflexed endoscopy of the GEJ shows a widened lumen revealing the squamous epithelium of the esophagus [61]. Hill grading of the flap valve correlates with GERD symptoms, further indicating the flap's importance in the anti-reflux barrier [61].

2.4.4 Crural Diaphragm and Phrenoesophageal Ligament

The diaphragm is a key component in maintaining the GEJHPZ competence. The esophageal hiatus of the diaphragm is most commonly formed by a loop of muscle known as the right crus of the diaphragm [62]. It is a space through which the esophagus, the anterior and posterior vagal trunks, and esophageal vasculature can pass from the thorax into the abdomen. A circumferential connecting ligament, known as the phrenoesophageal ligament, loosely joins the right crus muscle to the structures passing through (Figure 2-3). The ligament is viewed as an extension of the fascia on the thoracic and abdominal sides of the diaphragm, although there is some anatomic variation in humans [63], [64]. The endothoracic fascia forms the uppermost part of the ligament and remains as a single sheet as it crosses between the diaphragm and the esophagus [63]. The

sub-diaphragmatic fascia forms two leaflets as it leaves the diaphragm. The upper leaflet extends upward through the esophageal hiatus to either fuse with the endothoracic fascia or attach to the esophagus just below it [63]. The lower leaflet turns downward and attaches to the GEJ region [63]. Loose, fatty tissue lies in the space created between the leaflets and the esophagus, forming the subhiatal fat ring. The structure of the ligament allows the esophagus to slide a few centimeters upward or downward through the hiatus, which accommodates temporary shortening of the esophagus and upward motion of the GEJ during swallowing. Therefore, the position of the GEJ relative to the diaphragm is free to move, and the peristaltic function of the esophagus does not have to be tied to the respiratory cycle [62].

During inspiration, the right crus of the diaphragm contracts, exerting pressure on the lower esophagus just proximal to the GEJ. This additional contraction of the diaphragm complements the tonic contraction of the intrinsic muscles of the GEJ and is credited with maintaining the barrier function during periods of high intra-abdominal pressure [64] An interesting interplay between the GEFV and the crural diaphragm can be inferred. At the end of expiration, the diaphragm is high in the thorax and the orientation of the stomach relative to the esophagus puts the flap valve in its optimal, acute position to act as a one-way valve. At this point, the right crus muscle is at its most relaxed state (although tension may still exist due to elongated position), and the abdominal and thoracic pressures are well balanced. As inspiration begins, the efficacy of the flap valve decreases as the left dome of the diaphragm presses downward on the fundus. Furthermore, the thoracic pressure decreases and abdominal pressure increases as the visceral organs are compressed, leading to a pressure gradient that favors reflux of stomach contents. However, the crural diaphragm contracts at the GEJ, essentially 'making up' for the loss of flap valve function and pinching the GEJ tightly to resist the new pressure gradient [65].

2.5 Neuromuscular Physiology

The GEJHPZ anti-reflux function is due to multiple anatomic elements. However, for tissue engineering, the most relevant control systems are those modulating the contraction of the smooth muscle cells (SMCs) in the junction region of the esophagus and stomach. The upper third to half of the esophagus in humans contains striated muscle in the muscularis externa but transitions to completely smooth muscle well before reaching the GEJ, so its control will not be discussed here. Phrenic nerve control of the diaphragm will also not be discussed.

Unlike the rest of the esophagus, the GEJHPZ is tonically contracted to prevent regurgitation. The smooth muscle cells themselves seem to be in part responsible for this increased basal tone, as some of them tend to contract on their own without stimulation [66]. Before diving into the specifics of the myocytes, however, it would be best to have a general understanding of the key players in the nervous and endocrine systems that modulate the smooth muscle tone.

The enteric nervous system is generally viewed as the self-sufficient controller of the entire gut, although it responds readily to autonomic signals from the central and peripheral nervous systems. The myenteric plexus is largely responsible for producing coordinated movement throughout the gut, without the need for central input, by sequentially inhibiting and stimulating the layers of the muscularis externa. In the esophagus, the most common pattern is anterograde peristalsis, which pushes boluses of food further down the tract. The circular muscle directly proximal to the bolus contracts to prevent backward flow, while the circular muscle in front of the bolus relaxes. This is accompanied by longitudinal muscle shortening at the location of the bolus, driving it forward. These contractions in both layers of muscle travel down the esophagus in paired waves. The muscular control is accomplished through two main motor

neuron populations. Myenteric cholinergic neurons release ACh to stimulate muscarinic receptors on smooth muscle to cause contraction [67]. Myenteric nitrergic neurons release nitric oxide (NO), a well-known inhibitory molecule for smooth muscle, to cause relaxation [68]. These myenteric neurons often synapse onto interstitial cells of Cajal (ICC), which are known as the 'pacemaker cells' of the gut. ICC are electrically coupled to nearby smooth muscle cells, coordinating their contraction [69]. Slow-wave pacing, which has been linked to peristalsis in the stomach and intestines, does not seem to be important in the LES due to the tonic contraction. Rather, ICC appear to be important mediators of effective nitrergic and cholinergic signaling [69], [70]. In an afferent role, ICC are important in mechanosensing in the stomach [69].

The central nervous system modulates the ENS through cranial nerve X, the vagus nerve. In its afferent role, it carries non-painful sensory signals from the esophagus and stomach towards the brain [71]. Efferently, it functions as the major parasympathetic control to the upper gastrointestinal tract [71]. Efferent vagal neurons release acetylcholine (ACh) to activate neurons in the myenteric plexus of the ENS [66]. There are two populations of efferent cells [72]. The first synapse onto myenteric cholinergic neurons, helping to maintain basal tone. This population is centrally inhibited during swallowing, leading to relaxation. The second group becomes active when swallowing and stimulates myenteric nitrergic neurons to further decrease GEJHPZ pressure by releasing NO [73]. This is supported by numerous stimulation studies of the vagus nerve, which found that the pressure decreases for a while, then increases again [66]. Thus, the simplified view of parasympathetics as promoting 'rest and digest' holds true here.

The sympathetic system influences the esophagus and stomach through the greater splanchnic nerve, which contains pre-synaptic nerves from the sympathetic chain and leads to the celiac ganglion [67]. This ganglion is located directly anterior to the aorta near the lesser

curvature of the stomach and is where the presynaptic sympathetic neurons release ACh onto postsynaptic neurons. Postsynaptic sympathetic neurons classically run alongside arteries to their targets, so these fibers follow the celiac trunk of the aorta to the left gastric artery, then to the esophageal branch to reach the GEJ. The sympathetic neurons are adrenergic, primarily releasing norepinephrine (NE) onto either ENS neurons or directly onto smooth muscle cells [66]. While non-painful sensory information travels through the vagus nerve, painful stimuli are transmitted via neurons running alongside these sympathetic nerves [71].

Numerous endocrine and paracrine molecules have been investigated in relation to pressure changes at the GEJ. Gastrin, histamine, and motilin, which are linked to greater acid production and contractions in the stomach, cause increased pressures in the GEJHPZ. More complete lists of endocrine mediators can be found elsewhere [72]

Armed with an understanding of the competing signals converging on the GEJ smooth muscle, we may understand how cellular differences between different muscle groups contribute to the normal physiology. Gastric clasp fibers express voltage-sensitive L-type calcium channels, which have an intrinsic resting tone [72]. Because they are already somewhat contracted, the action of NO causing relaxation at appropriate times is especially important. In contrast, the sling fibers have non-L-type calcium channels and generate less resting tone [72]. Thus, they are a more responsive contractile element than the clasp fibers and readily respond to ACh by increasing their tone [72].

2.5.1 Swallowing-Associated Relaxation

A bolus of food is moved from the mouth into the pharynx by the voluntary phase of swallowing, but, after entering the pharynx, a coordinated involuntary swallowing reflex takes over [74]. In the body of the esophagus, the peristalsis is accomplished by contractions of the muscularis

mucosa and muscularis externa. Peristalsis can be initiated in two ways. Primary peristalsis is the natural response following the swallowing reflex, whereas secondary peristalsis is activated by esophageal distension. Once the swallow is initiated, the GEJHPZ relaxes and stays relaxed while peristalsis is occurring [68], [73]**Error! Reference source not found.** Once peristalsis has completed, basal tone returns to the GEJHPZ.

2.5.2 Transient Lower Esophageal Sphincter Relaxations, Belching, and Vomiting

Transient Lower Esophageal Sphincter Relaxations (TLESRs) are normal, periodic relaxations of the GEJHPZ. They can be initiated by stretch sensors in the stomach, which initiates a reflexive relaxation [75]. The reflex arc depends on the vagus nerve, which eventually leads to activation of nitrenergic postganglionic neurons at the GEJ [73]. One key function is to release air from the stomach in the form of belching. The ability to vent excess gas pressure from the stomach is important to normal human physiology, as evidenced by the development of gas-bloat syndrome in some patients following Nissen fundoplication [76]. The fundoplication procedure, which is used to treat GERD, involves wrapping part of the stomach around the GEJ to prevent reflux. If this constriction is too tight, it can lead to new symptoms in some patients, including pain and bloating from trapped air [75].

TLESRs may have an important role in the development of GERD in certain patients. Numerous etiologies have been investigated, leading to sub-classification of the disease into upright versus supine GERD. [77] Some patients have abnormally frequent TLESRs. This usually presents with symptoms while in an upright position but not while lying supine, possibly due to postural TLESR suppression [77]. GERD due to weakness of the anatomical reflux barrier formed at the GEJ is generally worse while lying down, but symptoms can be present while upright as well [77].

Vomiting is another case in which the GEJHPZ relaxes. Nausea prior to vomiting decreases pressure in the GEJHPZ in human subjects, even when induced by visual stimuli [78]. The process of vomiting has been described as occurring in three stages, with the first two resulting in retrograde flow from the intestine into the stomach and an increase in abdominal pressure [79]. The final stage of vomiting involves GEJHPZ relaxation combined with abdominal muscle contraction for ejection of the gastric fluid [79].

2.6 Mechanical Properties

Criteria for successful tissue engineering of the GEJHPZ should account for both the mechanical properties and forces generated by the native tissue. Detailed reviews of the tissue mechanics of the esophagus and the stomach have been published recently [80], [81]. Because these tissues are multi-layered and anisotropic, there is variability in the experimental and modeling choices made by different groups. Additionally, there are few studies that used human tissues. When modeling the human esophagus as a simple isotropic tissue, an ultimate tensile strain of 140% and ultimate tensile stress of 1.2 MPa were found [80]. Ovine and porcine esophagi have been used for investigating the mechanics of the individual layers. Tensile strength and stiffness are greater in the longitudinal direction of the muscularis externa than in the circumferential direction [82]. Similarly, the stiffness of the combined mucosa/submucosa was greater in the longitudinal direction. This is consistent with the peristaltic role of the esophagus, in which distal circumferential distensibility would reduce the resistance to forward motion of a food bolus, but longitudinal distensibility might decrease the 'pull-forward' effect exerted by longitudinal contraction. The stress-strain profiles are typical of collagenous tissues, showing a low-stiffness 'toe region' dominated by fiber alignment followed by a dramatic increase in the stiffness in the high-strain regions [82]. The submucosa and mucosa are very distensible at low strains in part

due to their highly folded nature, indicating that during normal function, the muscularis externa contributes most of the mechanical properties. However, under high strains, the mucosa/submucosa stiffens and exhibits a much higher failure stress. This suggests that the inner layers of the esophagus protect the muscularis externa from over-distension [82].

When it is not relaxed for the passage of a food bolus, a basal tone must be maintained in the GEJHPZ. Advances in high-resolution, three-dimensional manometry have led to a detailed understanding of the pressure profile in this region. A recent study characterized the pressures averaged across 10 healthy adult patients [83]. Similar to other studies, they found that the profiles at the GEJHPZ were not symmetric. At end-expiration, when the crural diaphragm is relaxed, there is a distinct pressure spike towards the angle of His. This asymmetry was present throughout multiple maneuvers but was most pronounced during forced inhalation (Figure 2-4). While end-expiration and tidal inspiration pressures peaked at 45 and 110 mmHg, respectively, the maximal pressure recorded during forced inhalation reached 216 mmHg. This is consistent with the respiratory motion interplay between the diaphragm and GEFV noted above. They found that administration of edrophonium hydrochloride (Tensilon test) to induce stronger skeletal muscle contraction in the diaphragm led to increased pressures. By subtracting the end-expiration pressures from the inhalation pressures, the authors calculated the pressure contribution of the crural diaphragm. They found that contraction of the right crus increased pressure on all sides of the GEJHPZ but was asymmetric with a peak towards the left anterior region of the junction. These measurements are important sources of information for tissue engineers hoping to recreate the GEJ, since the mechanical forces that must be exerted to match physiological function are quite large.

2.7 Tissue Engineering Progress

Tissue engineering in the foregut has largely focused on the bodies of the esophagus and stomach, rather than the GEJ. Of these three, the esophagus is the easiest to replicate due to its relatively simple muscular structure and squamous epithelium. Indeed, many reviews have been published recently which discuss the various material, cell, and bioreactor choices made to generate problem-specific tissue engineering solutions [15], [19], [39], [84]. The approaches range from acellular scaffolds to bi-layered, recellularized constructs and even scaffold-free organoid bioprinting [85]. Overall, the field has made good progress, with some of the larger animal models living a year or more before the studies were ended [86], [87].

In contrast, there has been a significantly lower volume of work in gastric engineering during the last decade. Much of the earlier work involved acellular patches applied to stomach wall defects. A recent study showed that mesenchymal stem cell (MSC) supplementation to these scaffolds was beneficial for smooth muscle tissue development [88]. One group was able to make small (<70mm) tissue-engineered stomachs by seeding gastric epithelial organoids into nonwoven polymer tube scaffolds [89]. This promising approach was used to replace the native stomachs in rats and resulted in improvements in blood hemoglobin levels when compared to control rats that had undergone a Roux-en-Y procedure to bypass the stomach. However, no significant benefit was found during the six-month study in terms of body weight maintenance when compared to control. The specialized gastric epithelium is difficult to culture with conventional techniques [90]. Using organoid culture techniques with addition of specific factors has been successful in propagating gastric organoids for over one year [91].

The only examples of tissue engineering specifically for sphincteric GI components come from the Bitar lab at Wake Forest University. This group made lower esophageal, pyloric, and

anal sphincter constructs using primary SMCs isolated from the those regions [92], [93]. These SMCs were cast with collagen hydrogels into a dish around a central post. The SMCs proliferated and contracted the gel around the post, orienting themselves circumferentially around it. By adding another gel layer loaded with neural progenitor cells (NPCs) isolated from the small intestine, they created innervated constructs with evidence of cholinergic and nitrergic signaling, as would be expected in a functional ENS [92]. The LES constructs were thin-walled rings with an inner diameter of 8 mm. In loop tensile tests under 20% strain, they generated a basal tone resulting in $\sim 460\mu\text{N}$ measured force. This was significantly higher than the $\sim 110\mu\text{N}$ force generated by similarly constructed rings made from colonic wall SMCs, indicating a preservation of the higher-tone phenotype. The same group used a cell sheet technique on a patterned substrate to make a tissue engineered duodenum using primary SMCs and NPCs [94]. These sheets were wrapped around a chitosan tube, and an engineered pyloric sphincter using the gel compaction method was placed at one end. The entire construct was implanted subcutaneously in a rat abdomen for 4 weeks for vascularization and maturation. Long-axis tensile testing compared to the native intestine showed comparable strength, ultimate strain, and Young's modulus. Loop tensile tests of tubular cross sections showed that the pyloric sphincter exhibited higher basal tone than the nearby duodenal segments. Overall, the work of this group over the past decade is a promising start to recreating the LES.

Given the much smaller volume of literature for tissue engineered LES, it will be beneficial to review findings from the esophagus and stomach. The general principles will apply to future work on the GEJ, but special considerations must be made to recreate the anti-reflux function. The complex muscular structure will be more difficult to replicate. Furthermore, designing the implant to perform the anti-reflux function while still allowing for belching and

vomiting may also be a challenge. What follows are emerging themes from these related bodies of literature.

2.7.1 Lumen Patency

Most tissue-engineered esophagi have been made of decellularized extracellular matrix, epithelium, muscle, or some combination of these. Functional peristalsis has not been a major goal in these constructs, since the first challenge is keeping the lumen open and avoiding anastomotic failures. Strictures are persistent narrowing of the esophageal lumen, which can lead to a complete inability of food to pass through. In the context of tissue engineering, they are caused by fibrous, scar-like tissue that contracts around the lumen. One of the earlier approaches to prevent stricture formation was stenting during the first weeks following implantation, which is a method that is still frequently used.

A protective epithelium is important for preventing stricture formation [19]. This phenomenon has been observed in canine and porcine animal models and is believed to be due to the role of the epithelium in protecting the musculature below from infection, mechanical abrasion, and other exposures [86], [87]. Studies in humans from whom diseased esophageal epithelium is surgically removed have demonstrated the importance of a protective layer, and supplementation of extracellular matrix (ECM) products as a protective layer to aid re-epithelialization has been effective in reducing stricture formation [17].

However, intact epithelium alone is not always sufficient to prevent strictures. It may be that supplying a population of healthy smooth muscle cells prevents overpopulation by fibroblasts, which could eventually lead to stricture [87]. This is consistent with findings in acellular grafts in gastric engineering, which experienced similar contraction, even when protected from luminal contents [90]. Strictures primarily affect full-circumference replacements,

presumably because scar tissue in only one part of the wall is unlikely to cause dramatic narrowing. This is evidenced by a small clinical trial in which acellular porcine urinary bladder ECM was used to patch full thickness wall defects in the esophagus [20]. All patients survived and had full re-epithelialization, with only one requiring subsequent balloon dilation because of stricture formation. Thus, protecting tissue engineered constructs with epithelium, preventing fibroblast overpopulation, and limiting the proportion of wall circumference replacement when possible, should all be important considerations in the design of the gastroesophageal junction.

2.7.2 Scaffolds

Generally, while synthetic materials are more robust and easier to control, well-designed biological scaffolds tend to yield better results for cell differentiation [19], [24], [39]. Decellularized extracellular matrix materials have been gaining traction across the tissue engineering field as a scaffolding strategy that preserves some native signaling from the matrix to the cells. Decellularized esophagus, urinary bladder and small intestinal submucosa have been used recently in esophageal engineering [95]–[98]. Use of decellularized esophagus has been hypothesized to be more appropriate than other tissues as more discoveries are made about the importance of chemical and structural signals within the matrix [24] In-depth reviews on the specifics of scaffold options can be found elsewhere [19], [84]

2.7.3 Vascularization

The limiting distance of 100-200 μm between any engineered tissue and its nearest arterial supply is widely cited, and creating vascularized constructs has historically been a challenge in tissue engineering of thick tissues. Because the human GEJ wall thickness can range from approximately 2 to 6 mm, this vascularization problem must be addressed [99]. One of the most promising new tools for creating artery or large arteriole-sized vessels is 3D bioprinting [100].

Sacrificial materials or molds can be incorporated into the printed constructs for subsequent removal, instantly creating vascular channels as small as approximately 200 μm in diameter. These channels can be subsequently flooded with endothelial cell suspensions to establish a blood-tissue barrier.

Implantation of constructs into the greater omentum or latissimus dorsi muscle as an *in vivo* bioreactor is a proven method for creating functional vasculature [101]. Vessels grow into the implanted tissues from the existing vasculature at the site of implantation. The greater omentum is particularly promising because its fatty, vascularized structure is not dissimilar to the adventitia around the native thoracic esophagus. It is also anatomically close to the GEJ, opening the possibility of simply transposing a flap containing the implanted construct for final placement at the junction. Many of the cellular, tissue-engineered constructs for the esophagus and stomach have relied on this technique [19].

2.8 Conclusion

The valve-like junction between the esophagus and stomach has great clinical importance, since excessive contraction can lead to problems eating and drinking and incompetence can lead to reflux disease and cancer. The structure is fairly simple from a histological perspective, with layers of muscle surrounding an inner mucosa. With recent advances in tissue engineering of the esophagus and stomach, it is plausible that tissue-engineered solutions to replace damaged GEJs can be developed. However, the alignment and innervation of the muscular structures required to maintain the reflux barrier will present a challenge to the field. The primary criterion for tissue engineers should be to prevent reflux through the junction, even with high back-flow pressure gradients. If one-way flow is accomplished, it will represent a large step forward in the management of disease. Due to clinical evidence that backwards flow is desirable for venting the

stomach and vomiting when required, secondary criteria focused on managing these problems should also be considered.

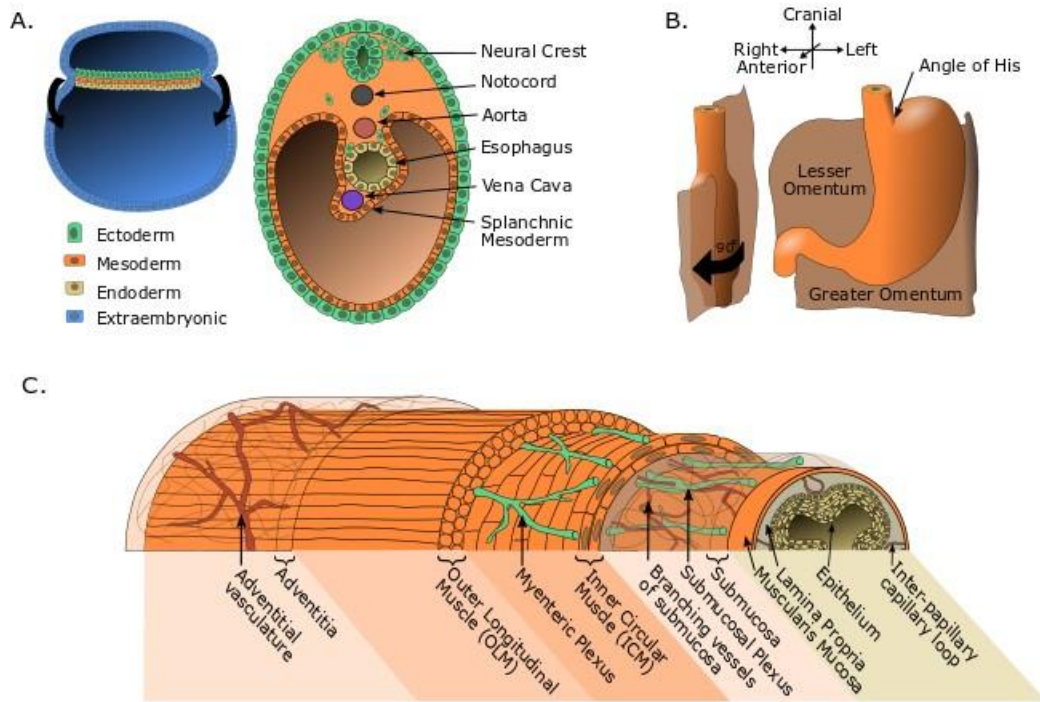


Figure 2-1: Development of the GEJ

Development of the gastroesophageal junction and embryonic contribution to layers of the adult histology. A) The trilaminar disc folding into a “tube within a tube”, as seen on the craniocaudal axis. B) Formation of posterior stomach bulge and 90-degree rotation to final position. C) Key layers of the adult lower esophagus, showing the locations of vasculature (arterial only), innervation, and muscle alignment.

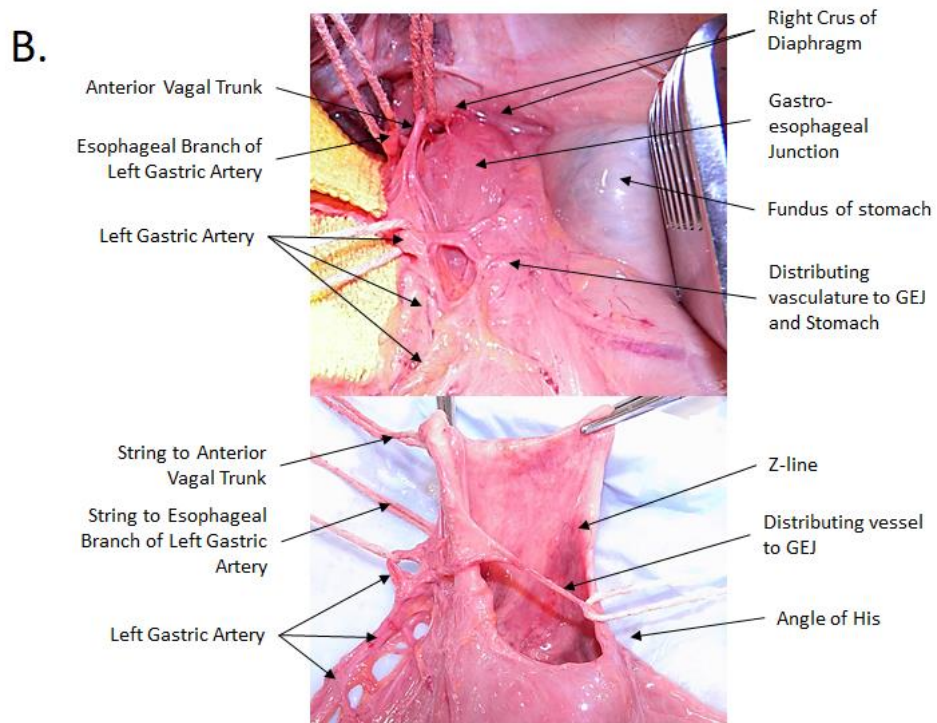
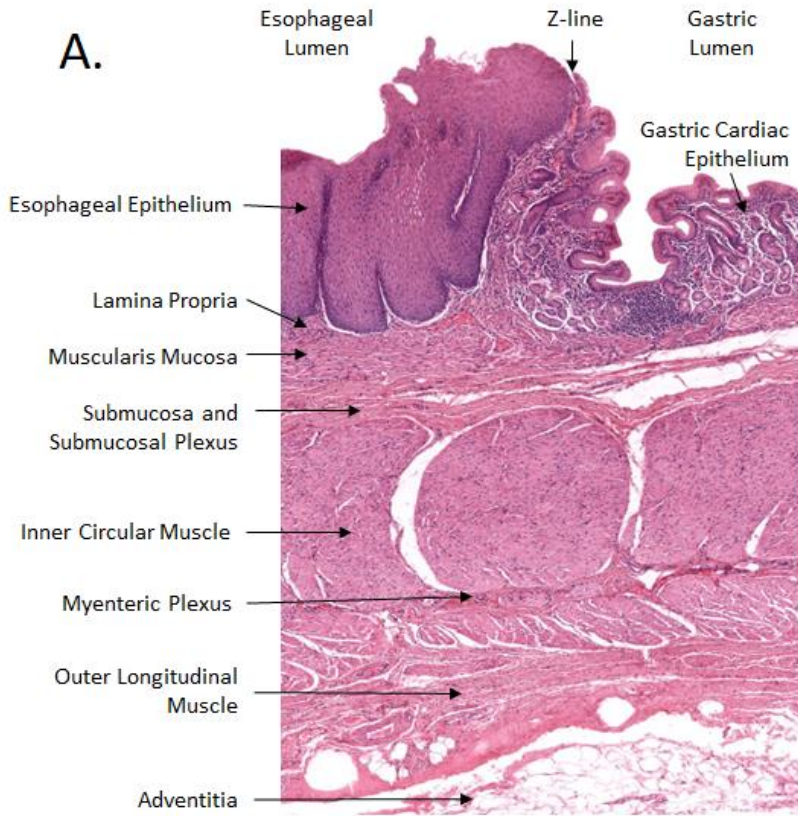


Figure 2-2: Normal Histology and Gross Anatomy of the GEJ

Anatomy and histology of the adult human GEJ. A) A longitudinal section of the GEJ, stained with hematoxylin and eosin. At the top of the image, a sharp division is seen between the esophageal and gastric mucosae. This image was provided by, and edited and reproduced with permission of, Dr. T. Clark Brelje and Dr. Robert J. Sorenson from the University of Minnesota. A high-resolution image is available online at histologyguide.org. B) Human cadaveric gastroesophageal junction, demonstrating its normal position in the abdominal cavity and key anatomical elements. The upper panel shows the anatomy in situ, after removal of the abdominal wall and some visceral adipose tissue. The lower panel shows the GEJ ex vivo, with a longitudinal incision made on the left-anterior surface of the junction to display the z-line. (Figure. 2B are primary images taken by Caleb Vogt).

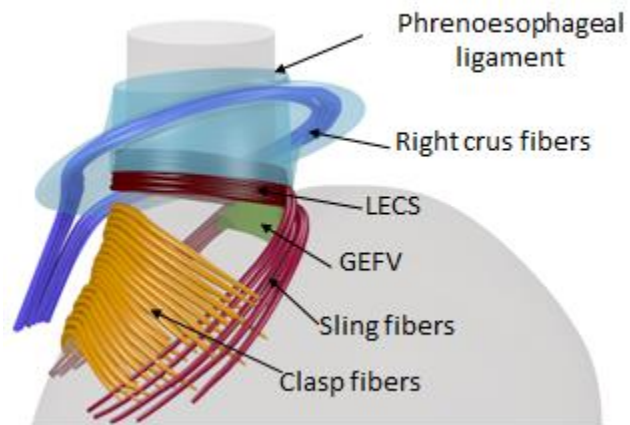


Figure 2-3: Gastroesophageal High Pressure Zone Illustration.

A representative diagram detailing the components of the GEJHPZ, showing the sling and clasp fibers of the UGS, the LECS, and the diaphragm components.

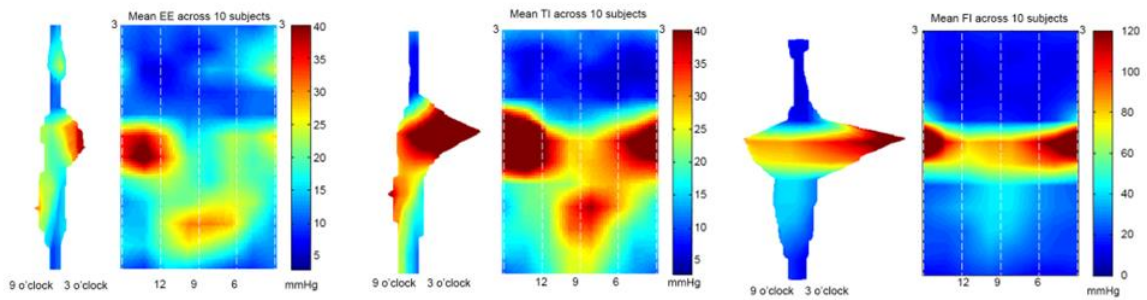


Figure 2-4: Esophageal Manometry

Averaged high-resolution 3D manometry of 10 healthy adult humans, presented as 3D and 2D unraveled images. The 3 o'clock position points to the greater curvature and the 9 o'clock position to the lesser curvature. 12 o'clock is anterior. Left-most image set shows end-expiration (EE) pressures. Middle set shows tidal inspiration (TI). Right-most set shows forced inspiration (FI), note change in color scale bar. Reproduced and adapted with permission from Mittal R.K., et al., Functional morphology of the lower esophageal sphincter and crural diaphragm determined by three-dimensional high-resolution esophago-gastric junction pressure profile and CT imaging, *American Journal of Physiology - Gastrointestinal and Liver Physiology*, 313(3): G212-G219. Copyright 2017 by the American Physiological Society.

3 Modalities and Materials for Tissue Engineering the Stomach and Esophagus

The following chapter contains elements published in 2023 in the Journal of Immunology and Regenerative Medicine. The included material was authored wholly by Caleb D. Vogt.

Vogt, C., Diaz-Gutierrez, I., & Panoskaltsis-Mortari, A. (2023). The gastroesophageal junction – A gap in tissue engineering. Journal of Immunology and Regenerative Medicine, 20, 100073.

<https://doi.org/10.1016/j.regen.2023.100073>

3.1 Introduction

There are a myriad of benign and malignant conditions that may lead a patient to undergo esophageal resection. By definition, an esophagectomy involves transecting both vagi nerves, and removing en bloc the distal esophagus, the GEJ and the proximal portion of the stomach. These changes permanently alter the anatomy and physiology of the GEJ, losing the ability of maintaining a one-way-valve mechanism. Due to vagal denervation, patients often experience functional dysphagia and delayed gastric emptying. These factors contribute to ongoing reflux after esophagectomy, which is a problem that could lead to persistent damage of the esophageal remnant and intestinal metaplasia in 6% of patients [102]. Currently, there are no widely adopted surgical approaches to addressing the lack of a GEJ valve to protect the esophageal remnant, although some experimental techniques are being developed. Despite progress in creating

esophageal replacements, there are unaddressed challenges relating to the gastroesophageal junction (GEJ) [103].

Tissue engineering could provide solutions for surgeons and patients confronted with esophagectomy that destroys the normal GEJ. The goal is to develop tissue replacements that can perform the key roles of the original valve without succumbing to damage from food transit or acid exposure. Significant progress has been made in tissue engineering for the esophagus, with some treatments progressing to clinical trials. However, no progress has been reported in engineering the GEJ. It is expected that application of tissue engineering concepts bolstered by specific knowledge gained from progress in the esophagus and stomach will jump-start development of engineered GEJ constructs. Specific engineering techniques including decellularization, electrospinning and 3D bioprinting are discussed.

3.2 Tissue Engineering Modalities

Many new tissue fabrication techniques have been developed recently that have been applied to the esophagus and stomach. Some, such as decellularization, electrospinning, and 3D printing, can likely be applied in engineering of the GEJ. Others, such as treatment with cell therapy or cell sheets, are better suited for regeneration of single layer defects like those seen after endoscopic mucosal resection (EMR) [104]–[107]. In that procedure, dysplastic or early neoplastic mucosal tissue can be removed without compromising the entire wall [108]. These can be effective at reducing strictures due to inflammation following the surgery [109]. However, approaches that do not aim to replace the full thickness and full circumference of the organ have limited applicability to the needs for GEJ replacement.

3.2.1 Decellularized Scaffolds

The application of decellularized extracellular matrix (dECM) scaffolds in surgical repair and tissue engineering of the esophagus has a long history and fully reviewing the progress made with this material is beyond the scope of this review. However, some notable trends have developed (Table 3-1). Decellularized tissue scaffolds are produced by harvesting whole tissue from a patient or animal, then subjecting it to a series of washes to remove as much cellular and antigenic material as possible while preserving the beneficial microstructure, mechanical properties, and pro-regenerative signals. The preferred method likely depends on tissue-specific parameters. Detergents such as sodium dodecyl sulfate (SDS), and Triton X-100 are commonly used in combination with DNase enzymes, although some hope to find gentler reagents [110], [111]. It is unclear at this point how much tissue homology or allogenicity matter. One group investigated the effect of porcine esophageal versus urinary bladder or intestinal submucosa ECM, but found that beneficial effects of the esophageal ECM found *in vitro* did not translate to differences in tissue healing *in vivo* [112]. While engineered materials are generally more conducive to mass production, some commercial decellularized products such as Alloderm® (cadaveric human skin) and Biostage 4® (porcine small intestinal submucosa, formerly Surgisis®) have been used successfully in animals and humans for esophageal repair [18], [113]–[116].

3.2.2 Engineered Meshes and Films

Numerous synthetic scaffold materials have become popular for tissue engineering in the gastrointestinal system. Compared to biological materials, synthetics are associated with greater mechanical tunability and manufacturing quality control. Recent approaches to gastroesophageal engineering using combinations of synthetic materials through a variety of production methods are outlined in Table 3-1. Electrospinning is a favored technique in which solubilized polymers

are drawn from a metal needle by a large voltage difference between the needle and the collector plate or mandrel. The solvent evaporates during flight, leaving only the polymeric fiber. If the collector is static, unaligned fiber is deposited. In contrast, electrospinning onto a rotating mandrel can be used to create aligned fibers if the mandrel spins fast enough [117], [118]. A recent development is patterned cryogenic electrospinning, which uses the tendency of fibers to be attracted to high points on the collector plate to create patterned fibrous and gap regions in the material [119]. Electrically driven flows have been combined with 3D motion controllers to perform electrohydrodynamic printing, which allows precise control over the deposition of the fiber as seen in conventional 3D printing [120]. One commercial product for tissue engineering repair is the Cellspan Esophageal Implant® system. This is a polyurethane (PU) electrospun tube which provides temporary support for tissue regrowth in esophageal defects [121]. Other manufacturing techniques include melt-drawing, solvent casting, and temperature precipitation. Melt-drawing involves heating a polymer above its melting point extruding it through a nozzle onto a rotating collector [122]. Solvent casting is an evaporative process that leaves behind a polymeric film. This can be patterned by casting onto a textured mold, which can provide alignment cues to cells [123]. Temperature-induced precipitation of a polymer results in a porous, foam-like scaffold [124]. The solvent is lyophilized to remove it while the polymer is in a precipitated state.

As demonstrated in Table 3-2, there has been much focus on use of aliphatic polyesters. Poly(lactic acid) (PLA), poly(glycolic acid) (PGA) and poly(ϵ -caprolactone) (PCL) are frequent candidates due to a long history of use in tissue engineering and somewhat predictable biodegradability through hydrolysis [125]. While implant-specific parameters have an effect, it is generally expected that PGA structures will degrade within a few weeks, PLA will degrade within months, and PCL will degrade within a few years. Properties of these polymers can be

modified by blending of monomeric units in different ratios, as seen with Poly(lactide-co- ϵ -caprolactone) (PLCL) and poly(lactide-co-glycolide) (PLGA) [126]. Alternatively, impregnation of one polymer within another polymer network, as performed by Maemura *et al*, can be another method of tuning a construct's stiffness and degradation [127]. Certain polymers from the polyurethane (PU) class are also biodegradable and have been used in tissue engineering [125], including polyester urethane [128]. Crosslinked polyurethanes (CPU) have been grafted with silk to improve cell attachment and proliferation [123]. Finally, non-resorbable surgical mesh made from polyvinylidene fluoride (PVDF) has been used for esophageal defect repair [129].

3.2.3 3D Printing

Many tissue-engineering methods require molds, forms, or patterns to create the 3D shape required by the final construct. However, 3D printing allows the direct construction of these complex shapes. This technology has been employed at almost every stage of the gastric and esophageal engineering process, from depositing the primary implant material to creating custom molds and delivery devices for use with more traditional tissue-engineering methods. An early application by Maeda *et al* in 2015 demonstrated that cell sheets could be delivered inside the esophagus and adhered to the wall using a custom 3D-printed endoscopic delivery tip with an expandable balloon [130]. This proof-of-concept study did not include long-term monitoring, as the animals were euthanized after 6 hours.

In 2018, Chung *et al* first attempted a combined approach of electrospinning a PCL structure over segmented 3D printed PCL support rings on a mandrel [131]. This construct was matured in the greater omentum for 2 weeks before excision and implantation into a full-circumference defect in a rat. No animals survived beyond 15 days due to obstruction from coprophagy and hair, but epithelialization was found to have begun from the anastomotic ends. The Chung group has since investigated approaches using 3D printing of PCL [132] and

combining 3D PCL printing with electrospun polyurethane coated with fibronectin [133], [134]. They have found that human adipose-derived MSCs (hADMSC) delivered to the scaffold in Matrigel® increases desmin expression and vascularization while decreasing CD68+ macrophage infiltration in a rat esophageal defect model [134]. The fibronectin-coated PU was found to be more conducive to epithelial development and the 3D printed PCL facilitated greater desmin expression. These materials were combined by electrospinning on a rotating mandrel, then printing a reinforcing PCL lattice on top to form an esophageal replacement for a full-circumference rat esophageal defect [133]. Unfortunately, the rats died within 15 days from anastomotic leaks and obstruction, highlighting the added challenge of full-circumferential replacement. Park *et al* found similar beneficial results to adding MSCs to 3D printed PCL patches in a rodent model [135].

In 2021, Yeleswarapu *et al* demonstrated that an esophageal replacement could be fashioned by filling a 3D printed mold with a hydrogel derived from decellularized and solubilized caprine esophageal ECM [136]. The mold consisted of inner and outer walls with pores to encourage transport of media and dissolved gasses, allowing survival of the L929 mouse fibroblasts within the gel. Despite the 4mm thick walls, staining of hypoxia inducible factor 1-alpha (HIF 1- α) did not reveal any significant hypoxia. This work illustrates the usefulness of porous-walled molds and has since been extended into true 3D bioprinting through development of a decellularized ECM bioink [137].

3.2.4 3D Bioprinting

In contrast to the purely synthetic materials used in classical 3D printing, 3D bioprinting uses “bioinks” made from combinations of biological polymers, decellularized ECM components, and synthetic polymers. These bioinks may be acellular, or have cells or spheroids included. While bioprinting is quickly growing in popularity because of its beneficial biological effects and high

degree of spatial control, the multi-field expertise required to make successful constructs can slow its implementation. Nonetheless, three examples of true bioprinting in the esophagus have been published. In 2019, Takeoka *et al* extended their group's previous work in tracheal engineering to develop a scaffold-free bioprinted esophageal construct [85]. Spheroids containing a combination of normal human dermal fibroblasts (NHDFs), human esophageal smooth muscle cells (heSMCs), and either human umbilical vein endothelial cells (hUVECs) or human bone marrow derived MSCs (hBM-MSCs) were produced in U-well plates. An aspiration-assisted pick-and-place printing method placed these spheroids onto an array of needles to temporarily develop the structure, which was removed after 1 week. After 3 more weeks maturation in a bioreactor, these constructs were implanted into rats. Orthotopic, full circumference replacement failed due to aspiration pneumonia. The surgical approach was adjusted by inserting a silicone stent and implanting the bioprinted esophagus alongside the native esophagus. This interposition between the esophagus and stomach allowed the rats to survive, and after 30 days there was evidence of keratinized stratified squamous epithelium and low α -SMA expression in the wall.

Nam *et al* developed a hybrid bioprinting approach which created a porous-walled scaffold using PCL that had three layers [138]. Mucosal and muscular layer bioinks were developed from decellularized porcine esophageal mucosa and muscularis externa, respectively. Human esophageal epithelial cells and smooth muscle cells contained within the inks benefited from the dragging printing method used to increase the wall porosity. These constructs have not yet been investigated *in vivo*. In 2021, Ha *et al* took a similar approach, using PCL to print a stent with open-topped channels running in the walls [139] Porcine esophageal mucosa was developed into a decellularized bioink and loaded with human esophageal Het-1A cells. This bioink was printed into the channels of the stent. Rats were exposed to radiation to induce radiation esophagitis, then the stents were implanted. Compared to non-implanted controls, the cell-loaded stent decreased

inflammatory cytokines and neutrophil infiltration while increasing the CD68+/CD208+ M2 macrophage response.

3.3 Human Trials

Despite the large number of preclinical studies demonstrating the potential of tissue engineering for the esophagus, there are few cases of intervention in humans. Early attempts by Badylak *et al*, Ohki *et al*, and Nieponice *et al* demonstrated that epithelial cell sheets or decellularized matrix material could be applied over the wound following EMR [17], [20], [21]. In 2016, Dua *et al* successfully treated a 24-year-old male patient with a full-thickness defect at the pharyngoesophageal junction [18]. Commercially available Alloderm® was wrapped around a stent and was sprayed with platelet-rich-plasma adhesive gel. The sternocleidomastoid muscle was positioned to cover the graft. The stent was not removed until three years later. Four years after the intervention, the new tissue showed evidence of normal multi-layered structure by endoscopic ultrasound, and manometry demonstrated contractile motility on liquid swallows. In 2021, Aho *et al* used the Cellspan® esophageal graft to treat a full-circumference 4cm segmental resection in a 75-year-old male [140]. ADMSCs isolated from the patient 5 weeks prior to surgery were seeded onto the graft and incubated in a bioreactor for 6 days immediately before the surgery. The post-surgical course was complicated with many hospitalizations and eventual death at 7.5 months due to ischemic strokes and cerebral hemorrhage. Histology of the esophagus showed that the implant site had developed an intact epithelium and muscularis mucosa but lacked a muscularis externa. While the total amount of human experience is low, these limited results are generally consistent with expectations derived from the preclinical studies and point towards feasibility of tissue-engineered esophageal treatments in the near future.

3.4 Future Perspectives on the GEJ

Progress towards developing viable treatments will require a methodical approach. First, a patent conduit with an appropriate epithelium must be achieved. This early part of the development process can rely heavily on prior work for the esophagus and stomach. Once an acceptable approach has been finalized, iterative development of the GEJ valve can begin. Closely mimicking the normal GEJ structure is likely preferable as a long-term goal, due to the balance a healthy GEJPHZ can strike between acting as a valve or conduit in response to stimuli. However, this will require a high degree of control over muscle tissue alignment and neuromuscular circuitry. These are active areas of research [141]–[144] in the tissue-engineering field but acceptable strategies do not yet exist. As an intermediate goal, purely mechanical tissue-engineered valves are a possible option. While not ideal, previous experience with mechanical sphincter augmentation through either surgical procedure or medical device is able to provide some relief to many patients suffering from GERD [145], indicating a possible role in similar strategies minimizing reflux in a tissue engineered GEJ.

The choice of tissue engineering techniques and materials are largely entwined. For example, certain polymeric materials that lend themselves easily to electrospinning are often not amenable to 3D-bioprinting strategies. However, as demonstrated by many successful strategies in esophageal tissue engineering, it is possible to combine elements of decell/recell, electrospinning, 3D printing, and 3D bioprinting technologies. If the goal is to recreate the 3D structure of the GEJ as exactly as possible, 3D printing and bioprinting will likely play major roles. Unlike the esophagus, the GEJ is not as easily approximated as a cylinder that can be built on a mandrel or a rolled sheet which can be layered in a dish. The most basic function of 3D printing and bioprinting is to deposit material in precise locations in space. These techniques can be combined with computed tomography or magnetic resonance imaging to create patient-specific geometries.

Recreating the Angle of His and corresponding GEFV will be especially challenging without using a 3D printer or bioprinter. Unfortunately, 3D bioprinting can suffer from comparatively weak material properties. Assuming that some form of 3D printing will be the foundational approach, it will be possible to add in desirable elements from the other approaches to address these weaknesses.

Direct 3D bioprinting comes in multiple forms with trade-offs in printing resolution and speed. One very precise method uses a laser to deposit bioinks and cells, and has a resolution on the order of 0.1-100 μm [146]. However, building up a 3D tissue using this type of printer is prohibitive in both print time and inflexibility of the method. Exquisite control of the printing parameters must be maintained, and combining this method with other tissue engineering techniques is challenging. Another technique, extrusion bioprinting, is less precise (\sim 100-1000 μm) but is more common due to its increased printing speed and ease of incorporation to other tissue engineering strategies. Extrusion bioprinting uses a liquid or partially gelled bioink which is forced through a nozzle by gas pressure or a piston. Switching between multiple materials or bioinks mid-print is common with this type of printer as many are equipped with multiple printheads. As demonstrated by Nam et al [138], these bioinks can contain site-specific decellularized ECM components and cells to recreate the layered structure of the esophagus. In the context of the GEJ, it is likely that distinct mucosal and muscular inks will be required.

Extrusion bioprinting benefits greatly from its ease of integration with other tissue-engineering strategies. First, multiple options exist for creating small and mid-sized vasculature. One is sacrificial patterning, in which a dedicated acellular bioink is printed in the spaces that channels or voids are desired [147]. Once the printing process is complete, the sacrificial material is evacuated, leaving channels. Another method uses a coaxial printing nozzle to flow a crosslinking solution through the inside of an outer shell made of a bioink. This locks the tube

shape in place and can rapidly produce vessel-like structures [148]. Second, extrusion printing through long nozzles allows for printing in a support bath [149]. Gravity is a challenging problem in additive manufacturing since unsupported overhanging structures will fall. Materials must also be stiff enough that they do not deform under their own weight during the printing process. In conventional plastic 3D printing, these issues are addressed by printing temporary support structures. 3D extrusion bioprinting can be done into a partially gelled bath which is density matched to the bioinks being printed. This bath fluid has a yield stress that allows it to flow out of the way of a moving nozzle but holds the extruded bioink in place as the printing process continues. Thus, the printed construct is produced suspended in a support bath which can be washed away after the printing is complete. This approach could be important for direct printing of the GEJ structure since its unique shape will leave it prone to sagging if printed by more conventional processes.

3.5 Conclusion

Developing tissue-engineered solutions for the GEJ must account for the unique function and environmental stresses related to the stomach contents. A one-way valve mechanism is of critical importance to protect the repaired esophagus and airways from acid exposure. However, an overly competent valve that prevents venting of gastric pressure or vomiting poses its own risks. While overly reductive, engineering the body of the esophagus essentially requires an epithelialized tube that is permissive to flow. The GEJ will either require excellent recapitulation of the native neuromuscular architecture or creative new designs to meet the constraints of its function. The large body of work in esophageal tissue engineering provides a suite of materials that either permit or promote esophageal regeneration using synthetic or biologic materials, respectively. New technologies such as 3D printing and bioprinting will likely have a role in recreating the GEJ structure.

Table 3-1. Applications of decellularized materials in gastric and esophageal tissue engineering.

| Target Organ | Tissue Source | Recipient Animal/ <i>In Vitro</i> Model |
|--|--|--|
| Esophagus | Porcine Esophagus | Pig [150]–[152] |
| | | Rabbit [153] |
| | | Rat [112] |
| | | <i>in vitro</i> [154]–[158] |
| | Rat Esophagus | Rat [159], [160] |
| | | Mouse [161] |
| | Caprine Esophagus | <i>in vitro</i> [110] |
| | Rabbit Esophagus | Rabbit [162] |
| | | <i>in vitro</i> [163] |
| | AlloDerm® or ADM® (Decellularized Skin) | Mini pig [116] |
| | | Dog [115] |
| | Porcine small intestinal submucosa | Pig [164] |
| Rat [111], [165] | | |
| Dog [96], [166], [167] | | |
| Biodesign 4®/Surgisis® (porcine SIS) + Human amniotic membrane | | Mini pig [87], [114] |
| Porcine urinary bladder | | Dog [95] |
| | | Mouse [168] |
| Rat Stomach | Rat [169] | |
| Stomach | Surgisis® (porcine SIS) | Rat [88] |

Table 3-2. Applications of synthetic fiber, film, and mesh materials in gastric and esophageal tissue engineering.

| Target Organ | Method | Material(s) | Recipient Animal/ <i>In Vitro</i> Model | | |
|---------------------|-------------------------|--|--|-------------------------------|--------------|
| Esophagus | Electrospinning | Cellspan® | Pig [170] | | |
| | | Esophageal Implant (PU) | Mini pig [121], [171], [172] | | |
| | | PLCL | Pig [173] <i>in vitro</i> [174] | | |
| | | PLGA + SIS | Rat [175] | | |
| | | PHBV +/- Gelatin | <i>in vitro</i> [118], [176] | | |
| | | PCL +/- Gelatin | | | |
| | | PLGA + PCL | Rat [177] | | |
| | | PLGA | | | |
| | | PCL + Silk | Rabbit [178] Rat [179] | | |
| | | PCL | Rabbit [180] | | |
| | | Patterned Cryogenic Electrospinning | PCL | <i>in vitro</i> [119] | |
| | | Electrohydrodynamic Printing (E-jetting) | PCL + Pluronic F127 | <i>in vitro</i> [181, p. 127] | |
| | | Solvent Casting | | PCL + Gelatin Bilayer film | Rat [182] |
| | | | | Silk-grafted-PU + dECM | Rabbit [128] |
| | Silk-grafted-CPU + dECM | | | <i>in vitro</i> [123] | |
| Silk-grafted-CPU | <i>in vitro</i> [183] | | | | |
| | | Silk fibroin | Mini pig [184], [185] Rat [186] | | |

| | | | |
|---------|-----------------------------------|-----------------------------|-------------------------------------|
| | Melt Drawing | PLCL | <i>in vitro</i> [122] |
| | Temperature Induced Precipitation | PLCL + fibronectin | Pig [124] |
| | | PLCL + chitosan | <i>in vitro</i> [187] |
| | Other | PGA mesh + PLA + collagen I | Mouse [188] |
| | | PVDF surgical mesh | Rabbit [129] |
| | Melt Drawn Knitting | PCL + collagen I | Sheep [189] |
| Stomach | Other | PGA mesh + PLA + collagen I | Pig [190] Rat [127], [191]–[193] |

4 State of 3D Bioprinting for the Esophagus and Hollow Muscular Organs

Note that sections 4.2 – 4.4 were published in 2019 in the journal Translational Research. The included material was authored wholly by Caleb D. Vogt.

Galliger, Z., Vogt, C. D., & Panoskaltis-Mortari, A. (2019). 3D bioprinting for lungs and hollow organs. Translational Research, 211, 19–34. <https://doi.org/10.1016/j.trsl.2019.05.001>

4.1 3D Bioprinting Methodologies

Over the last two decades, four central bioprinting approaches have been developed [194]. We will group these four methods as “extrusion”, “droplet jetting”, “laser-transfer”, and “selective photopolymerization” bioprinting. These methods have been used with great success to create 3D tissue-engineered constructs, owing a part of their success to generally low cost, ease of use, acceptable cell viability, and scalability. All these approaches allow for tuning of the factors that make up the traditional triad of tissue engineering – cells, scaffold, and signals – with some variability in how much tuning can be accomplished [195]. Typically, these printers have been used in a layer-by-layer approach, where 2D slices are stacked to form a 3D structure. Finally, these technologies generally allow for both sequential and parallel manufacturing approaches. Sequential approaches often involve first depositing a scaffold in a desired shape, followed by addition of cells. Parallel approaches combine manufacturing steps to deposit cells, scaffolds, and

signals in one step. Here, we review the specifics of these central approaches in terms of their process, underlying physics, and manufacturing limitations.

4.1.1 Extrusion bioprinting

Extrusion bioprinting is similar in mechanism to the Fused Filament Fabrication style of traditional 3D printers, which feed a continuous of material through a nozzle mounted to a moving head [196]. The bioink is typically loaded in a syringe or reservoir which is connected to the nozzle. Flow can be driven by a piston, gas pressure or a screw (Figure 4-1). However, it was recently found that screw driven printers cause more cell damage than pneumatic systems [197]. The printing nozzles are frequently luer-connected blunt needles or plastic tips which come in a variety of sizes. The smallest tips allow for ~200 μm resolution at modest printing speeds, while larger needles decrease the resolution but drastically increase the volumetric flow. Because of the simplicity of the basic extrusion system, this approach can be adapted with several other technologies. Coaxial nozzles allow for multimaterial extrusion, which has been used for rapid crosslinking using an ink solution and a crosslinking solution [198]. Coaxial nozzles also allow for direct extrusion of vascular structures. Replacing the nozzle with microfluidic print heads allows for tightly-controlled on-demand mixing of bioink solutions and can be used for rapid multimaterial switching during the printing process [199], [200].

4.1.2 Droplet Jetting bioprinting

Inkjet bioprinting approaches have adapted physical principles from traditional inkjet printing to generate high-resolution 3D structures. These systems include at least four components – a bioink reservoir, a droplet generator, a motorized XYZ stage, and a target surface (Figure 4-1). Low viscosity bioinks flow from the reservoir into the droplet generating device, which can use a variety of approaches to generate a droplet on the order of 10s-100s of microns in diameter [201].

The droplet is transferred from the generator to the target surface by a combination of gravity and forces arising from the droplet generation. The manner of droplet generation leads to subclassification into the categories of continuous, drop on demand (DOD), and electrohydrodynamic printing (EHD) [202]. Continuous ink jetting involves pressurized flow of a bioink through a nozzle, with instabilities in the flow resulting in a continuous stream of droplets being ejected from the nozzle. DOD and EHD are able to generate individual droplets, and are thus more easily controlled [202]. Because these droplets are accelerated across a gap to reach the target, these jetting-dependent methods are “contactless”.

The central mechanism of DOD printing is a volume-changing element just upstream of the printing nozzle. The volume element can either cause a localized expansion in the bioink or a constriction of the reservoir geometry. Piezoelectric and electrostatic inkjet systems cause constriction of the reservoir, and thermal inkjet systems cause the volume change in the ink by inducing a small vapor bubble [202]. More recently, laser energy has been used to generate the vapor bubble in a method known as laser-induced side transfer (LIST) [203]. The resulting flow induced by all these methods causes a small volume of the bioink to eject out of the nozzle or orifice towards the target surface. In contrast, EHD printing uses a large electrical field to accelerate fluid droplets from a printing nozzle towards the target [204]. As with electrospinning, the ink is pulled from the nozzle rather than being pushed, theoretically leading to lower forces on the cells [202], [204]. EHD printing is also interesting in that it can generate continuous droplets, leading to higher throughput than what is possible with DOD printers [205].

4.1.3 Laser Transfer bioprinting

Laser transfer bioprinting uses lasers, directly or indirectly, to propel cells or bioinks from the printer onto a substrate. One of the earlier proposed methods was laser direct writing, in which a

laser was used to trap and propel cells toward a surface [206]. This technique was proposed to be used in two ways. First, the laser could be directed into a cell suspension and continuously trap cells as they pass through the beam, directing them towards the target surface [206]. This had benefits over the traditional “pick-and-place” type of manipulation available through optical tweezer technology, because it dramatically increased the rate at which cells could be patterned [207]. The second approach was to use the laser to capture cells in a bioink reservoir and propel them in a continuous stream through a hollow optical fiber to be deposited on the target surface [206].

Laser assisted printer technology has moved away from this earlier form of direct writing to a methodology generally known as Laser Induced Forward Transfer (LIFT). As with inkjet bioprinters printing, LIFT is both contactless and drop-on-demand. However, the system does not use a nozzle. Instead, a very thin layer of cells, proteins, or other bioink is cast or spin-coated onto a donor surface. This donor surface is comprised of an optically clear slide and a laser-absorbing substrate, which transforms the laser energy into thermal energy [146]. A vapor bubble is formed in the bioink layer, causing a droplet to jet towards the printing surface (Figure 4-1). This system can be combined with a microscope, which can allow for user selection of specific cells for forward transfer onto the target surface. Depending on the system, this technique can yield single-cell printing resolution. There have been numerous modifications to this general technique, which are reviewed elsewhere [146]. Some drawbacks of this method include the relatively complicated setup procedure, expensive hardware, and consistency problems as the thin bioink films are prone to rapid drying [146]. It is challenging to bioprint large 3D constructs

using LIFT because the donor bioink surface is only 10s of microns thick, requiring a very large surface area of bioink to build thick tissue constructs [203].

4.1.4 Selective Photopolymerization bioprinting

Stereolithography (SLA) and Digital Light Processing (DLP) are related technologies that rely on a bioink bath rather than a reservoir. While inkjet, laser transfer, and extrusion type printers deposit material in the desired locations, SLA and DLP printers flood the printing area and use light energy to selectively crosslink the material in a layer-by-layer fashion. SLA printers pattern the light energy by directing a crosslinking laser through a series of rotating mirrors, which trace out the desired layer shape (Figure 4-1). DLP printers use light projected via a micromirror array to illuminate corresponding pixel areas on the printing surface, resulting in crosslinked voxels of material wherever the light hits. With properly tuned bioinks, the SLA and DLP technologies can quickly fabricate high-resolution 3D structures which are supported during the manufacturing process by the surrounding ink in the bath. These approaches were adapted to bioprinting later than other 3D printing methods in part because of bioink limitations. Unlike other approaches, SLA and DLP printing rely exclusively on photopolymerizable bioinks. The inks must also include photo-absorbers to prevent off-target crosslinking in layers deep to the current printing layer [208]. Printing with multiple materials is a challenge in these projection-based methods, but some progress has been made in using multiple bioinks at a small scale [209], [210]. An adjacent technology of note is multiphoton lithography, which has the potential to further expand the usefulness of photopolymerization-based fabrication. Development of bioinks capable of crosslinking in response to multi-photon absorption allows for spatially controlled polymerization deep within a bath of bioink, rather than just at the surface as in traditional SLA or DLP [211].

4.2 Esophagus

Many tissue-engineered esophageal solutions have been attempted, but so far very few of them have utilized 3D bioprinting technology. Those that have used 3D printers did so indirectly, creating acellular scaffolds out of PCL, then seeding with cells or implanting into the greater omentum for cellularization and vascularization. The first attempt was in 2016, when Park et al. used a melt extrusion 3D printer to lay down a grid structure of PCL (concept in Figure 4-2a).[135] The resulting scaffold was coated with a solution of fibrin, thrombin, and rabbit Mesenchymal Stem/Stromal Cells (rMSC). After coating, the scaffolds were sutured as an allogeneic implant into a 5x10mm surgical defect in the esophagus of New Zealand white rabbits. The test subjects were tube-fed for 7 days following the surgery to allow the healing process to begin before challenging the barrier and mechanical functions of the esophagus. Both cellular and acellular controls remained patent out to three weeks without leakage or infection. Scaffolds containing rMSCs were completely covered by epithelium and subepithelial tissue, whereas controls did not have coverage on the luminal side. This work is promising for use of PCL as a 3D-printed scaffold and for use of allogeneic MSCs for supporting regeneration. However, no evaluation of the source of regenerated cells was done. MSCs are known for their ability to differentiate into a variety of somatic cell types including fibroblasts and smooth muscle cells.[212] Future experiments in fate tracking using reporter genes should be done to determine whether the MSCs are acting as paracrine signaling cells or are differentiating and proliferating to reconstitute the esophageal tissue. Staining with alpha-smooth muscle actin, vimentin, and desmin would allow for delineation of smooth muscle cells from fibroblasts and myofibroblasts.

More recently, Chung et al. used PCL to create a fully-circumferential esophageal replacement.[213] The goal was to create a suitable acellular graft that could maintain an open lumen (concept illustrated in Figure 4-2b). A 3D printer was used to melt-extrude PCL onto a

rotating mandrel, creating multiple rings. PCL was then electrospun over the rings while still on the mandrel, resulting in a structure approximately 5 mm in length and 1.6mm in internal diameter. Evaluation by scanning electron microscopy (SEM) showed an average microfiber thickness of 2.5 microns and an average pore size of 5 microns. Mechanical testing showed that the ultimate tensile stress and the yield stress were significantly higher than that of a natural rat esophagus, and the elastic modulus appeared to be comparable, below 400% strain. These acellular scaffolds were cultured in a rat omentum for 2 weeks for *in vivo* cellularization and vascularization. Omental tissue was found to have adhered to the outside of the graft and to have obscured the lumen, requiring opening with a needle. The cellularized construct was then orthotopically implanted into a full-circumference surgical defect in the same rat. All rats were euthanized or died by two weeks. Rats that died were found to have luminal obstruction with hair and excrement due to rat grooming behavior and coprophagy. The authors noted that the non-contracting nature of the PCL graft with a small lumen was the most likely problem, as aperistaltic grafts in dogs with larger inner diameters had not resulted in such obstructive problems. Histological evaluation showed loosely-organized, vascularized tissue adherent to the inner and outer surfaces of the graft, but few cells appeared to have infiltrated the nanofibrous structure itself. This may be due in part to the fairly small pore sizes available to the cells, which are generally known to be about 10 microns in length. PCL is also known to be hydrophobic, with poor cellular adhesion if not surface-treated with methods such as plasma deposition or peptide immobilization. [214], [215]. Some epithelial ingrowth from the proximal and distal anastomoses was noted, but its progression may have been halted by the inner supporting PCL rings. Overall, this approach shows promise as a method for vascularizing an acellular tissue via omental implantation. The inclusion of 3D-printed PCL rings to support the nanofibrous structure may be

more useful in large airway engineering, especially since it mimics the ring cartilage of the trachea.

4.3 Stomach, Intestines, and Bile ducts:

The stomach and intestines follow a very similar radial pattern to that of the esophagus, with an inner mucosa and submucosa surrounded by nerve tissue of the ENS and muscle tissue of the muscularis externa. The stomach has an additional layer of muscle compared to the rest of the gastrointestinal tract, as the muscularis externa has an innermost oblique layer of smooth muscle. There are striking differences in the epithelium, with gastric epithelium designed to secrete acid and protect against acid-damage, and intestinal epithelium specialized to absorb nutrients and secrete waste. Compared to the largely mechanical role of the esophagus, the functional roles of these specialized epithelia present a significant challenge to the tissue engineering field.

At this time, 3D bioprinting techniques have not been applied to the stomach. However, a joint research team from Organovo and Merck have used a proprietary 3D bioprinting system to create a flat model of intestinal epithelium sitting on muscle.[216] The goal of this work was to create better tissue models for drug and toxicology studies, and it demonstrated the ability to print cell-laden gels to recreate the complex structure of the intestines. Human intestinal myofibroblasts (hIMFs) and human biopsy-derived intestinal epithelial cells (hIECs) were suspended separately in proprietary bioinks. The fibroblast ink was printed as a layer onto a transwell membrane, then the epithelial ink was printed as a layer on top (Fig 4-2c). The bilayer was matured in culture for 10 days, then examined histologically and tested with multiple drug compounds. The resulting tissue demonstrated multiple epithelial subpopulations, including enterochromaffin cells and secretory goblet cells, both of which are vital to mucosal function. Immunolabeling of tight cellular junctions between the epithelial cells, and of cell membrane

transporters demonstrated that the epithelium had an appropriate structure and polarization. While analysis of the materials and techniques used in this work is limited due to its proprietary nature, this work is promising as it demonstrates the possibility of 3D bioprinting with patient-derived cells. Replication of the laminar structure of the intestine and achievement of epithelialization without relying on inward growth from the anastomosis will allow for longer intestinal segments to be created. This work did not investigate any mechanical properties of the bilayer, however, and consideration of the muscular structure and peristaltic function must be considered in the next steps towards bioprinting an intestinal graft.

Other hollow structures associated with the gastrointestinal tract include the extrahepatic bile ducts and gallbladder, which transport bile salts and acids produced in the liver to the intestinal lumen. The general tissue structure is an inner lumen lined with simple columnar epithelium, surrounded by layers of smooth muscle. Recently, Yan et al used a bioink composed of gelatin, self-assembled nanofibers, and cholangiocytes to demonstrate that bioprinted cholangiocytes were capable of self-organizing into branching tubular structures.[217] Part of the novelty of this work was using peptide amphiphiles with a laminin-like amino acid sequence to make self-assembled nanofibers in the bioink. Laminin is known to be a key component of the basement membrane underlying epithelium, and inclusion of these nanofibers led to much better tubular development when compared to other bioinks. The 3D bioprinted structure was a flat, multilayered grid. Combined with the small tubular organization, the most immediate application may be for intrahepatic bile ductules in liver tissue engineering.

4.4 Ureter, Urethra, and Bladder:

Hollow and tubular structures are integral to the function of the urinary system from the Bowman's capsule and tubules found in the renal nephron down through the urethra. The scale of

tubules found in the kidney is very small, leading to classification of the kidney as a solid organ. The ureter connects proximally to the kidney, and passively transports urine to the bladder in the pelvis. It is also capable of using peristaltic motion to shuttle the urine, due to the smooth muscle layer surrounding the epithelium.[218] The epithelium of the urinary tract is significantly different than that seen in other regions of the body, as the cells take on different shapes depending on the degree of distension applied to the surface. As such, it is known as transitional epithelium, or urothelium. When relaxed, it appears as a stratified cuboidal epithelium, but takes on a stratified squamous appearance when stretched.[219] Urothelium lines the ureters, bladder, and parts of the urethra.[220] The upper portion of the ureter has two layers of smooth muscle, with the inner layer being longitudinally oriented and the outer being circumferential.[221] The distal ureter has a third, outermost muscular layer which is longitudinally oriented. The bladder also has three layers of smooth muscle, which are continuous with the layers of the distal ureters.

Tissue engineering in the urinary tract is one of the first and most successful examples of growing replacement organs, and many promising examples of successful tissue engineering strategies exist.[222] 3D bioprinting has not been extensively applied yet, but some recent publications show promise of the technique. In 2017, Zhang et al used a bioprinting system developed by Atala's group at Wake Forest University to print a multi-layered urethra.[223] This printing system is able to extrude polymer melts and bioinks. By blending PCL with poly(lactide-co-caprolactone) (PLCL), the group was able to capture the desirable high tensile failure properties of PCL and still replicate the modulus of the native rabbit urethra. The optimal polymer geometry for replicating the tissue mechanics was found to be spiraling in structure (Figure 4-2d). Two fibrin bioinks were made, one with rabbit bladder smooth muscle cells (SMCs) and the other with rabbit bladder urothelial cells (UCs). The full tissue-engineered urethra was formed layer-by-layer, printing rings of PCL-PLCL blend, then inner rings of UC

bioink and outer rings of SMC bioink. The result was a vertically-standing three-layered tube, with PCL-PLCL occupying the normal position of the lamina propria and providing mechanical support. The fibrin gel was crosslinked with thrombin solution and the constructs were maintained in static culture for 7 days. Both the SMCs and the UCs were found to proliferate, although the percent viability decreased over time. The authors attributed this to lack of vascularization and use of static culture instead of a dynamic bioreactor. Overall, the use of cells from a biopsy was successful in creating a 3D bioprinted urethra. Future studies in vascularization and *in vivo* function and remodeling will be necessary. This approach could also be applied to the ureters since their general structure is similar to the urethra.

Another, more recent approach to creating tubular urothelial tissues used a coaxial extrusion technique.[198] A bioink was made using a blend of gelatin methacrylate (GelMA), alginate, and poly(ethylene glycol) acrylate (PEGOA) with a tripentaerythritol core. This allowed optimization of fluid properties for printability, and multiple crosslinking options for mechanical tuning after printing. Alginate was used as a thickening agent in the bioink and was crosslinked by calcium ions to support later post-processing steps but was then de-crosslinked by chelation of the calcium with Ethylenediaminetetraacetic acid (EDTA). A coaxial needle with three concentric components made it possible to create hollow tubes having a wall with two concentric layers. To create a urethra, human bladder SMCs were loaded into the outer layer bioink and human UCs were loaded into the inner bioink. These tissues were cultured out to 14 days and showed proliferation and appropriate tight junction proteins in the developing urothelium. Printing tissues in this way is convenient for quickly creating hollow tubes with multiple layers, but limitations to the approach will need further exploration. For example, the inner diameter of these urethras was approximately 650 microns with a total wall thickness of roughly 150 microns. Considering that the normal human urethra diameter is closer to 8 mm inner diameter, it is not known if the

structure will support itself or if it will require additional mechanical elements. Application to larger organs, such as the trachea, esophagus, and intestines will present an even greater challenge.

In 2018, Imamura et al. constructed bladder tissue by applying a similar needle-based technique previously used by the same group for tracheal engineering.[224] Bone marrow mesenchymal cells (STRO-1 positive) from GFP-positive rats were isolated by adherent cell culture, and then formed into spheroids by gravity-induced accumulation in wells. The organoids were bioprinted onto an array of needles, to create a rectangular cuboid with dimensions of 3x3x1 mm. After maturation for 7 days in perfusion culture, the spheroids fused to form a solid tissue that was removed and implanted into a surgical defect in a radiation-injury bladder model in a rat. Four weeks after implantation, vascularization and innervation from the wound edges was seen growing into the tissue-engineered construct. Smooth muscle actin staining also indicated myogenic differentiation of the GFP-labeled donor cells. Compared to sham surgery controls, the treated rats were found to have significantly better bladder function in terms of micturition frequency and volumes. While this biofabrication approach was used to make a patch, it could theoretically be used to make a whole hollow bladder, as the needle array structure allows for free positioning of spheroids in space without need for printing supports.

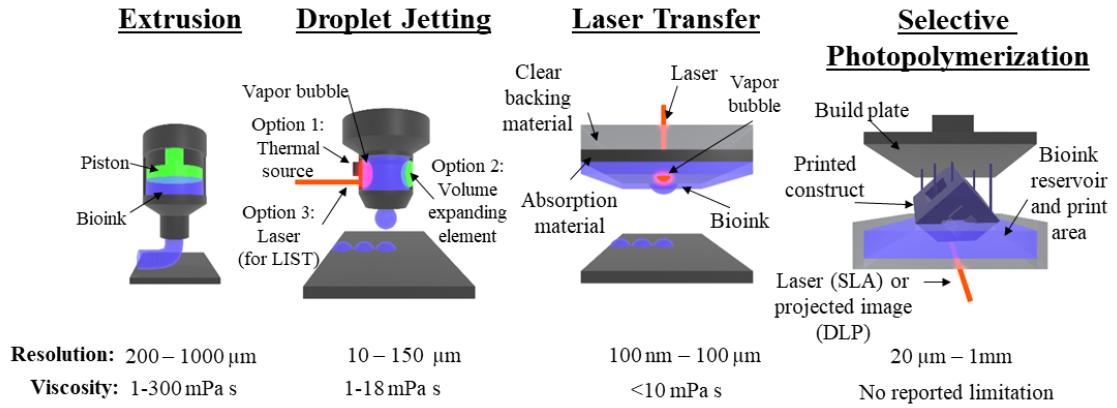


Figure 4-1: Common Bioprinting Methods.

Depictions of the most common methods of bioprinting. Values for printing resolution and bioink viscosity are included [225]–[227].

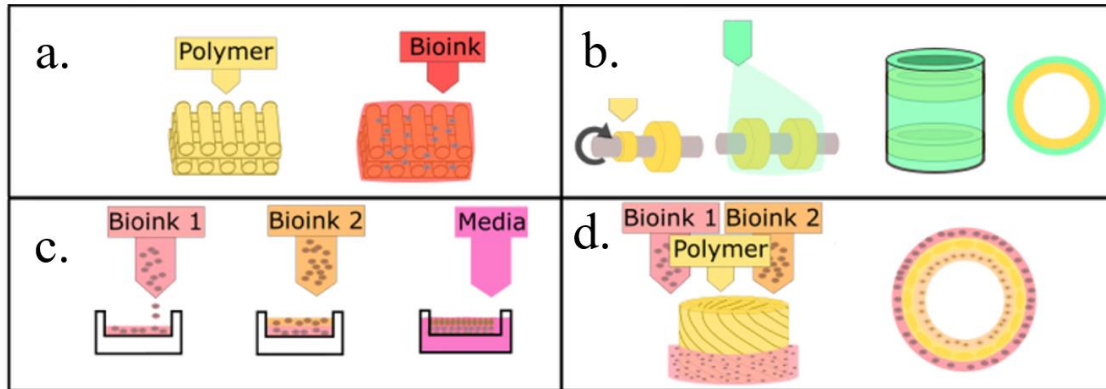


Figure 4-2: Methods of 3D Bioprinting and Biofabrication of Hollow Organs.

(a) Tissue engineered esophagus made by printing PCL in a cross-hatched pattern, then coated with rabbit MSCs in a fibrin hydrogel. (b) Acellular esophagus graft with 3D printed PCL rings on a rotating mandrel, subsequently covered with PCL electrospinning. (c) 3D bioprinting used to create a two-layered intestinal epithelium model in a transwell plate. The first layer contained fibroblasts, which was covered by a second layer of epithelial cells. The tissue matured and organized in culture. (d) 3D bioprinting of a urethra graft by simultaneously printing PCL/PLCL blend, a SMC bioink outside, and a UC bioink inside.

5 Approaches for Microtissue Production

5.1 Introduction

3D bioprinting using pre-aligned microtissues (PAMs) could address current challenges in the tissue engineering field around aligning muscle and other tissues in structures of varying complexity. In such an approach, the pre-aligned microtissues could be formed as anisotropic cylindrical pieces of smooth muscle which could be added into a bioink and 3D printed with an extrusion bioprinter. The flow of the PAM-laden bioink could align the microtissues exiting the nozzle through shear-induced alignment, resulting in direct-writing of the directionality of the cells within the printed tissue. Implementation of such a method will require a highly repeatable and scalable source of microtissues. Parameters like the diameter and length of the microtissues could have effects on the flow of PAM-laden bioinks and the tendency to clog in the nozzle, so a system to produce the PAMs should offer a level of control over such parameters. Scalability is necessary due to the large number of microtissues required to fill a tissue volume. It is not clear what PAM volume fraction will be ideal, but it may be a balance between optimal flow and high tissue density. In this chapter, possible methods for producing PAMs are examined.

5.2 Materials and Methods

5.2.1 Microscale Molding Approach

Microscale wells to cast and mold tissue has been a successful approach for creating aligned tissues by adding retention features into the well [4]. These features can be built as posts with thick caps to prevent tissues from slipping off the posts as they contract and bend the posts inwards. This process was adapted to investigate the effectiveness of the microwell molding for creating PAMs, making arrays of varying-sized microwells. First, 5-inch diameter silicon wafers

were cleaned with methanol, acetone, and air. A dehydration bake was performed at 150 °C for 10 minutes. Wafers were cooled to room temperature for at least 2 minutes. The first layer was soft baked by ramping from 25 °C up to 65 °C at a rate of 5 °C/min and held for 5 minutes. Then, the temperature was ramped by 5 °C/min to 105 °C and held for 20 minutes and then allowed to return to room temperature. A Karl Suss MA6 mask aligner was used to expose at 330 mJ/cm² to create the post features for the first layer. A second spin coat was performed with the positive photoresist at 4000 rpm for 30 seconds. The second soft-bake was performed in the same manner as the first. The second alignment and exposure step was performed to create the larger-diameter cap features to the posts, with an energy of 120 mJ/cm². A hard bake step was performed in the same manner as the soft bakes. After cooling to room temperature, the features were developed using MF-26A developer. The resulting structure consisted of the positive molding features.

Double-molding with polydimethylsiloxane (PDMS) (Sylgard 184, Dow Corning, 4019862) was accomplished using silanization to prevent adhesion. First, the positive mold on the silicon wafer was treated with oxygen plasma for 2 minutes, then quickly placed in a vacuum chamber with 50 µL trichloro(1H,1H,2H,2H-perfluorooctyl)silane (Sigma-Aldrich, 448931) overnight. PDMS base and crosslinker was mixed at a 9:1 ratio, centrifuged at 300g for 1 minute, then poured over silicon wafer. The wafer was placed in a vacuum chamber to remove bubbles from the PDMS, then transferred into an oven at 80 °C overnight. The resulting PDMS negative mold was gently removed from the silicon wafer and was silanized as previously described. PDMS was mixed at 10:1, centrifuged, and poured over the negative PDMS mold. After vacuum treatment to remove bubbles, the PDMS mold was baked overnight, producing the positive features for molding tissues. These final PDMS molds with the arrays of microwells were cut into small pieces and placed into well plates for cell culture. The molds were cleaned with 70%

ethanol for 30 minutes and UV exposure in the biosafety cabinet overnight. Molds were treated with sterile filtered 0.2% Pluronic F-127 in water to decrease cell adhesion.

The process for casting cells into the molds is shown in figure X. Human esophageal smooth muscle cells (Cell Biologics, H6089) were combined with 2mg/mL rat tail collagen type I (Sigma Aldrich, C3867) at a ratio of 1×10^6 cells : 1 mL collagen. The mixture was added to the molds, then centrifuged at 300g for 1 minute to force the collagen and cells into the microwells. The plates were tilted and excess collagen runoff was aspirated. The plates were placed in a 37 °C cell incubator upside down to encourage cell distribution for 10 minutes while the collagen was crosslinking. Sterile deionized water was added to the lid during this step to maintain humidity. The plates were removed from the incubator and culture medium was added gently on top of the microwells. The plates were returned to the incubator for microtissue maturation.

5.2.2 Mesoscale Molding Approach

Larger molds of various forms were produced by single casting PDMS with 3D printed parts. Regular casting was performed by pouring PDMS into 3D printed molds. Impression molding was also employed, where PDMS was cast into well plates and an impression mold was floated on top of the curing rubber to imprint patterns. The molds were produced by fused deposition modeling (FDM), a type of plastic extrusion printing, or by stereolithographic (SLA) printing. FDM materials were polylactic acid (PLA) or acrylonitrile butadiene styrene (ABS). SLA printing used Formlabs Surgical Guide Resin v2. In some cases, silanization of the plastic molds was used to decrease PDMS bonding to the mold during the curing process. Two general mold forms were investigated. First a larger scale version of the posts was created, with typical well widths and depths of 400 μ m. The lengths were typically 10 mm, and the ends of the wells expanded to circular regions with central posts. In some cases, room temperature vulcanizing

(RTV) silicone was extruded by hand through a 27 ga. nozzle to bridge between the tops of the posts and the wall sides, preventing microtissues from slipping up and over the posts during maturation. Second, a “harp” mold was investigated, which consisted of similar 400 x 400 μm channels connected on the ends by perpendicular channels. This allowed the developing microtissues to be held in place by the other microtissues in parallel wells as they all contracted. Finally, rather than casting PDMS rubber, RTV silicone was directly printed to produce harp molds. Cells and collagen were handled in the same manner as with the microscale molds to produce small tissues.

5.2.3 Cast Microtissue Development

Three different concentrations of cells (1, 5, and 10 million cells per mL) in 2 mg/mL collagen gel were cast into harp molds and incubated to observe the compaction dynamics, failure rate, and histology of the developing molded tissues. The compaction of the collagen gel was monitored by brightfield microscopy, comparing the original width of the molding channels to the current width of the microtissue in the mold. Failure was defined as snapping of the microtissue during development and was observed by brightfield microscopy. Samples were taken at the day 5 time point for hematoxylin and eosin staining using a cryosectioning approach.

5.2.4 Nuclear Alignment

The nuclei of cells within molded microtissues were labeled with DAPI or Hoechst nuclear dyes and imaged by epifluorescence and confocal microscopy. Control tissues made from the same cell and collagen mixtures that were not added into the aligning molds were also evaluated. Nuclei that were clearly visible were measured by hand using ImageJ to determine the angle of the primary Feret axis of the nucleus when approximated as an oval. The angle of deviation between the measured axis and the long axis of the nuclei was recorded.

5.2.5 Wet Spinning Approach

Collagen and cells were molded into fibers by entrapment within a temporary core-shell fiber structure produced by wet spinning with sodium alginate and calcium chloride. Cells and collagen ranging in concentration from 2-6 mg/mL were injected as a laminar stream into an outer laminar flow of sodium alginate, which was in turn injected into a stream of 100 mM calcium chloride and 3% sucrose. This was accomplished through custom designed SLA printed spinning devices, which were produced using a Form 3B printer and Surgical Guide v2 resin. Multiple versions of the spinning device were produced, with modifications to the internal dimensions and fluid paths as well as the external shape and tubing attachment features. Various flow rates of the three fluids were also investigated.

5.2.6 Wet Spinning Rheology

The viscosity of various solutions used in the wet spinning process were measured with a DHR-3 Rheometer (Texas Instruments). Flow sweeps were performed using a 2° cone and plate geometry with a 50 μm truncation and 40 mm diameter at 4 °C. Shear rates were tested from 100 to 0.1 s^{-1} .

5.2.7 Mechanical Testing for Fibers

An experiment was performed to investigate the effect of calcium concentration on fiber strength. An acellular fiber (no core) was spun into a 1L crosslinking bath containing different solutions of isotonic (300 mOsm) calcium chloride, with the balance comprised of sodium chloride. Seven different solutions logarithmically spanned from 1 to 100 mM calcium chloride, except for the 1mM solution being substituted for 0 mM (saline only). After spinning, the fibers were incubated in the bath overnight. The tensile strength was tested using the Biomomentum Mach-1 mechanical testing frame in a horizontal testing configuration. A custom 3D-printed chamber

with small cleat features at one end was filled with fluid from each fiber's corresponding crosslinking bath. A length of fiber ~10cm long was cut from the spun fiber in the crosslinking bath and formed into a loop. The two tails of the loop were wound through the cleat to secure the fiber, and a linear axis with a load cell (MA413, 10g, Biomomentum) and hook attachment was positioned to pull on the loop at 0.1 mm/s until failure. The maximum force was recorded. Samples that experienced failure in one of the sides of the loop between the hook and the cleat were analyzed. Samples which broke at the hook or at the cleat were removed from the analysis. Sample size was 3-7 per group.

5.3 Design Calculations

The minimum length of a spinneret within the 3D printed wet spinning devices was assumed to be the entrance length to establish fully developed flow. For laminar flow, this length depends on the Reynolds number (Re) of the flow and the hydraulic diameter (D_h), as shown in equation 5.1

$$\text{Eq. 5.1} \quad L_{h,laminar} = 0.05 Re D_h$$

The Reynolds number for the flow was calculated from the density (ρ), average velocity (u), and viscosity (μ). The characteristic length (L) was defined as the distance between the outer radius of the spinneret and the radius of the channel where the spinneret resides.

$$\text{Eq. 5.2} \quad Re = \frac{\rho u L}{\mu}$$

The hydraulic diameter was calculated for the ring-shaped flow region between the spinneret outer radius (r_i) and the channel radius (r_o) as shown in equation 5.3.

$$\text{Eq. 5.3} \quad D_h = D_o - D_i = 2(r_o - r_i)$$

All length measurements were assumed to be accurately reproduced from the source engineering drawings, ignoring possible errors introduced during the manufacturing process. Fluid parameters were measured by rheometry.

5.4 Results and Discussion

5.4.1 Casting Methods Experience

Both microscale and mesoscale molding approaches were able to form microtissues. Some benefits to molding in general were found. First, due to the 2-dimensional layout of the molds, it was easy to observe the development process during incubation by brightfield microscopy. As a quality control measure, this could allow for automated monitoring of every microtissues using a motorized microscope. The microtissues were held in place by the retention features in the molds, whether they were capped pillars, RTV silicone bridges, or angled wedges in the harp mold walls. This allows for tracking of individual microtissue development across long periods of time. Second, the casting method was very flexible when incorporating new design prototypes and could easily work with different culture dishes or well-plate formats. Directly 3D printing the molds with RTV silicone dramatically increased the speed at which design changes could be implemented for small scale studies. Finally, molding PDMS can be done with a variety of materials produced by different 3D printing methods. FDM modeling with ABS filament produced workable impression molds if the features were $>400\ \mu\text{m}$ in size. PLA was easier to print than ABS but was found to inhibit the curing of the PDMS and deformed under the high temperatures in the curing oven (65-90°C). The best results were obtained using SLA printing with Surgical Guide resin v2 on a Form 3B printer, due to the XY resolution of 25 microns, decreased deformation during PDMS curing, and lack of curing inhibition.

The general molding approach to making microtissues was found to have many significant drawbacks. The microscale approach was technically challenging, due to the high layer thickness and two-layered nature of the design for producing the capped pillars. The need for special photolithography tools and a cleanroom greatly increased the costs and decreased the speed of design iterations. Once the molds were completed and the microtissues were formed, there was no feasible method for removing them from the mold for use in other experiments. The mesoscale approach improved somewhat on the microscale approach, as the molds were easier to load with collagen and cells due to their increased size. It was also possible to cut the tissues free of the molds with a scalpel by cutting off the parts of the tissue attached to the retaining features in the various mold designs. Unfortunately, scalability was hampered by the large surface area required to make the microtissues and the long process times required to make the molds and cut the tissues free after maturation.

Another significant drawback was encountered in the form of tissue tensile failure, where the tissues seemed to generate a greater tension than the matrix could support during development. This was demonstrated using the mesoscale approach, where compaction, failure, and histology could be observed (figure 5-4). Increasing cell concentrations up to 10 million cells/mL increased the compaction rate but also the failure rate as the microtissues began to snap, resulting in $\geq 50\%$ failure by day 3 in some cases. Hematoxylin and eosin staining of the tissues that survived showed that even at the high cell concentration, the confluence within the microtissue was low. It might be possible that increasing the collagen concentration to increase the ECM stiffness could help stabilize the tissues and allow longer maturation times, but the sum of the challenges with scaling up tissue production even in the mesoscale approach led to abandonment of the method in favor of wet spinning tissue fibers.

5.4.2 Casting Nuclear Alignment

While the casting approach in general left much to be desired in terms of process, it could produce aligned cells. This can be seen qualitatively in the hematoxylin and eosin staining of the tissues in figure 5-4c. Quantification of the alignment through staining of the smooth muscle cell nuclei confirms the alignment, with ~80% of the nuclei being less than 20° off from the tissue axis. Thus, the cells demonstrate the expected alignment under anisotropic strain.

5.4.3 Wet-Spinning Approach

Multiple versions of the spinning device were rapidly iterated to investigate different design features. The final design incorporated the following elements, which were key to success either in the printing process for making the device or the wet spinning process for which it was designed. Generally, it was found that decreasing the part size to keep printing times as short as possible led to less clogging of the channels during the printing process. The smallest channel that could be reliably produced was 600 μm, which was the inner channel of the spinneret. To preserve lumen patency, it was necessary to have the smallest channels oriented along the z-axis of the printer's build volume. Once printed, the device was vigorously flushed with isopropanol and compressed air to prevent clogging during the UV curing process. It was found that the spinneret features in the spinning device tended to warp during the UV process due to their high aspect ratio, leading to the spinneret tip deviating towards the side wall of the device. This was managed by inclusion of three radially arranged stabilizing fins near the base of the spinneret feature.

The needle-like spinneret features in the device required a balance between increased length to allow flow development but decreased length to prevent clogging during the manufacturing process. The results of the Rheometry were applied to modeling the entrance

length required for the spinneret features. The calcium chloride and sucrose sheath solution, sodium alginate shell solution, and 4 mg/mL collagen core solution (acellular) all demonstrated moderate shear thinning behavior and low viscosity at 4 °C. For the purposes of modeling the entrance length, the greatest length will occur with the lowest viscosity solution, as the densities of all the solutions are comparable. The solution parameters used to calculate the maximum entrance length required was the calcium chloride and sucrose sheath solution, which at a shear rate of 100 s^{-1} had a viscosity of $1.07 \times 10^{-3} \text{ Pa s}$. and at a shear rate of 0.1 s^{-1} had a viscosity of $5.04 \times 10^{-2} \text{ Pa s}$ (Figure 5-5a). Taking these measurements as upper and lower bounds of the viscosity, and assuming 5 mL/min mass flow rate and 1.036 kg/L density, the entrance length to establish fully developed flow ranges from 0.178 to 8.405 mm. In the final device design, it was found that a spinneret length of 3.64 mm allowed for production of long core-shell fibers.

5.4.4 Fiber Strength

It was found that the 0mM calcium chloride bath was too weak to test. Even careful handling quickly led to the breaking of the fiber. As expected, increasing calcium concentration generally resulted in increased tensile strength (Figure 5.4). Based on these results and subjective assessment of handling with forceps, it was determined that the calcium chloride concentration in the crosslinking bath should be $\geq 10\text{mM}$.

5.4.5 Handling of Wet-Spun Fibers

The ability to create large amounts of tissue encapsulated in a single continuous fiber gives rise to new challenges and opportunities for various applications. While the system described in this work has production constraints due to maximum syringe loads and total spinning time due to collagen crosslinking and cell viability, it was still capable of regularly producing continuous fibers over 30 m long. Even 30 m of fiber quickly becomes difficult to manage with traditional

culture methods. Simply collecting the fiber in a petri dish for incubation causes challenges with media changes and later use of the tissue fiber. The fibers are denser than culture media and can be concentrated at the bottom of plasticware by gravity or centrifugation, but the surprisingly high bending moment resists fiber compaction in a constrained space. This necessitated leaving a large amount of waste media with the fiber to avoid accidental aspiration during changes.

During media changes for loose fibers, a 70 μm conical cell strainer insert was used in conjunction with vacuum aspiration to keep the fibers in the petri dish. Care was taken to aspirate gently and allow waste media to passively cross the filter membrane to avoid damaging the fibers near the membrane. Using the fibers for additional experiments in a loose state also led to challenges. Samples could be taken using forceps to grab clumps of fiber and cut with scissors, but taking consistent volumes of tissue became increasingly difficult as continued sampling led to ever smaller fiber fragments being left in the culture.

To address these challenges, a motorized winding system was developed. Early designs consisted of a stepper motor driving a gear train to rotate a spool. Some early iterations included pre-spooling rollers for the purpose of increasing the fiber “time-of-flight” in the crosslinking bath prior to collection on the spool. These were linked by a gear train to the spool and were size matched to the spool’s functional diameter to ensure consistent fiber tangent velocity on the rollers and the spool itself. If the alginate in the fiber was not well-crosslinked prior to spooling, the tension and close proximity of the fibers on the spool tended to cause irreversible adhesion of neighboring fibers, which could limit the usefulness of the fibers in applications that require unspooling at a later time. It was hypothesized that increased calcium concentration, increased “time-of-flight” pre-spooling, and winding underwater or with a continual misting mechanism could decrease the likelihood of this adhesion. It was also expected that increased calcium

concentrations in the crosslinking bath would increase the fiber strength, which could make handling easier.

The spool was designed to collect the fiber into two aligned sheets that could lay flat inside of a petri dish. This was accomplished by designing two parallel beams which were held in relation to each other by struts. The spool rotated around an axis halfway between the parallel beams, and a spun fiber could be collected on the spool in an aligned manner. The effective diameter of the spool was 10 cm. For ease of handling and sterility, the spool was designed with steel M5 hex nuts embedded in one end that could interface with magnets on the motorized spooling device. The hex nuts were added after the spools were printed by the Form 3B with Surgical Guide v2 Resin, and additional resin was brushed on to seal them in place and protect them from exposure to solutions. This approach allowed the spools to be autoclaved and easily attached and removed from the spooling device. The spooling device's magnetic spooling head was cleaned with 70% ethanol and UV exposure in the biosafety cabinet prior to use in a fiber production process.

5.5 Conclusion

Implementation of proposed 3D bioprinting method requires a source for PAMs that can produce large quantities with high efficiency. Three general approaches were examined to produce these microtissues. The microscale and mesoscale molding approaches had minor benefits in small scale experiments, but were hampered by difficulties in generating large numbers of tissues that could be removed from the molds for use in later processes. These include the long and complicated manufacturing processes for the silicone molds, and the inefficiency of restricting the tissue growth area to 2D surfaces within traditional culture vessels. However, these approaches did demonstrate that human esophageal smooth muscle cells could be aligned by

strain anisotropy induced by the retention features in the mold design. Wet spinning was found to be a more scalable process since the mold for the tissue is produced on demand as a shell of alginate in a core-shell fiber. The core containing collagen and cells can fuse into a continuous tissue fiber, which may be cut into smaller pieces to produce the PAMs for bioprinting. This process will be discussed in greater detail in chapter 6.

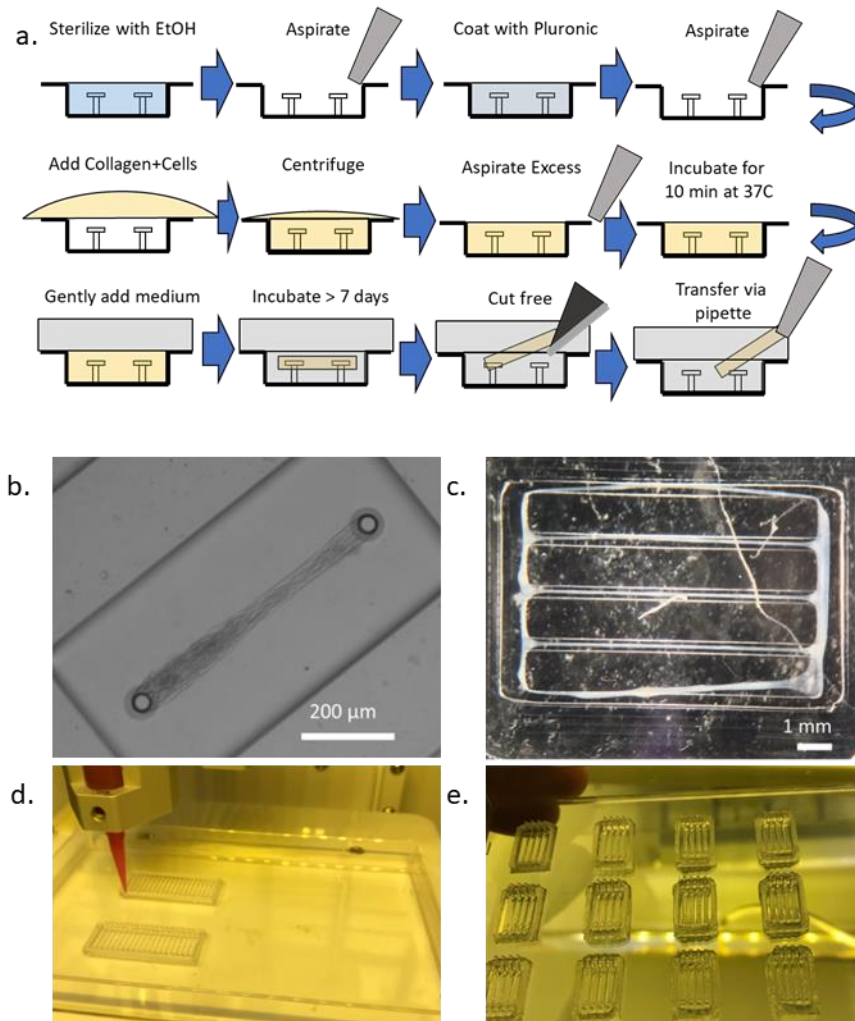


Figure 5-1. Casting Method for Microtissue Production.

(a) Depiction of the molding approach for making microtissues, using a mold style with capped pillars. (b) microscale molding approach with aligned microtissue suspended between capped pillars. (c) Harp style molding approach, with 5 tissues developing in parallel. (d,e) directly printed harp style molds using RTV silicone.

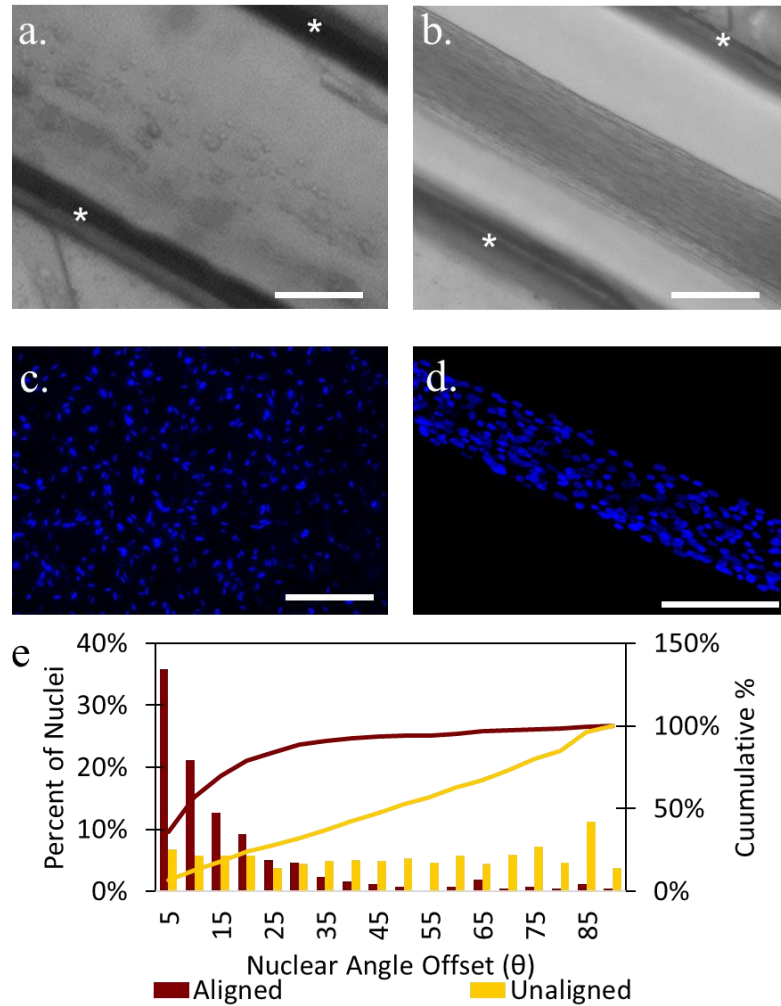


Figure 5-2. Nuclear Alignment of Cast Mesoscale Tissues.

(a) Cells in a mesoscale harp mold with round morphology immediately after casting. Asterisks denote the side walls of the mold. (b) After 7 days maturation, the microtissue has compacted and appears to have aligned cells through brightfield imaging. (c) Nuclear staining of the unaligned control tissue and (d) microtissue show the alignment imparted to the nuclei by the molding process. (e) Quantification of the nuclear alignment by histograms of the nuclear angle offset. The Kolmogorov-Smirnov test on the cumulative distributions found significant difference with $p < .001$. All scale bars are $200 \mu\text{m}$.

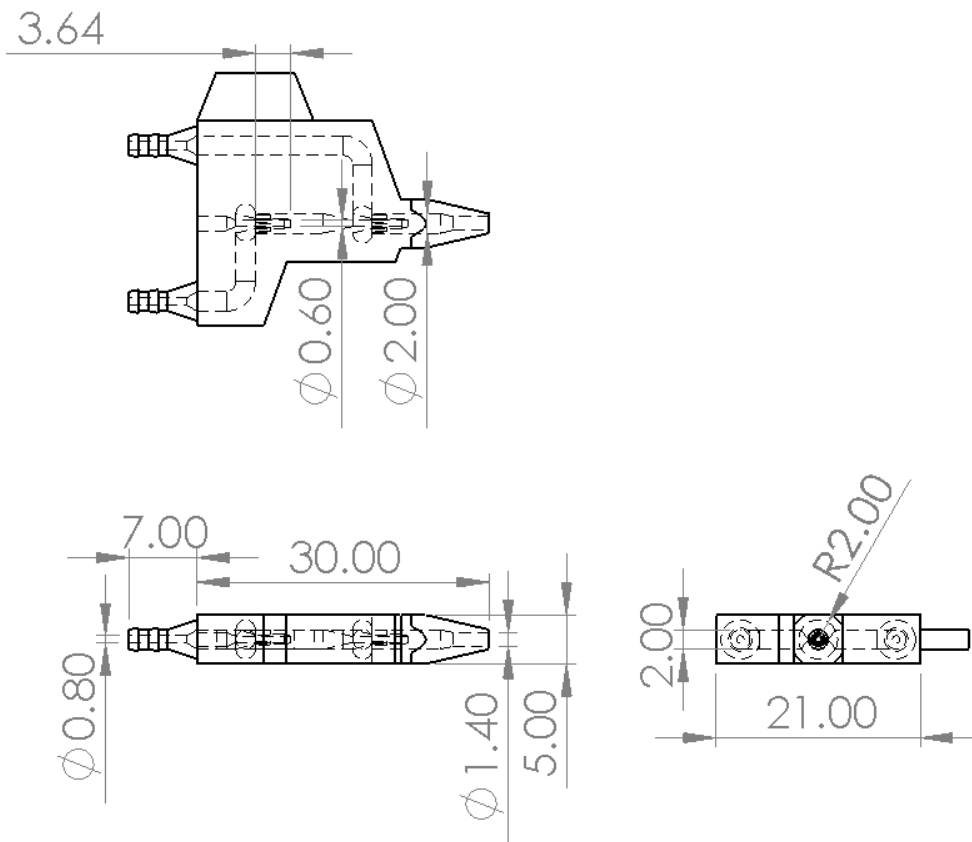


Figure 5-3. Drawing of Microfluidic Spinning Device.

Drawing with millimeter dimensions for the microfluidic fiber spinning device used in this work, which was produced on a Form 3B SLA printer using autoclavable surgical guide resin. The side inlets to the device are barbed for tubing connection. The central channel is designed for interference insertion of microfluidic tubing.

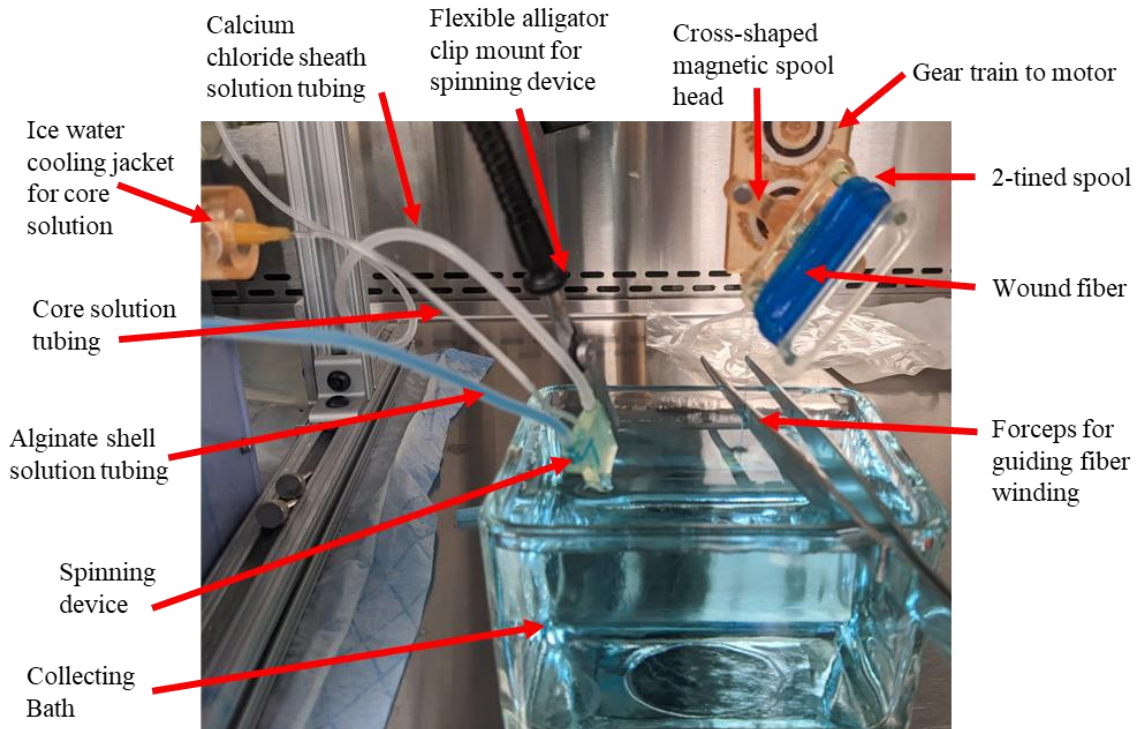


Figure 5-4. Fiber Spinning and Spooling Setup.

A photograph showing key elements of the fiber spinning apparatus. The fluid pumps are not shown, but the tubing from the pumps can be seen entering from the left-hand side and connecting to the spinning device. The motorized spooling device is attached to an aluminum frame to hold it above the collecting bath. The entire system is contained within a biosafety cabinet.

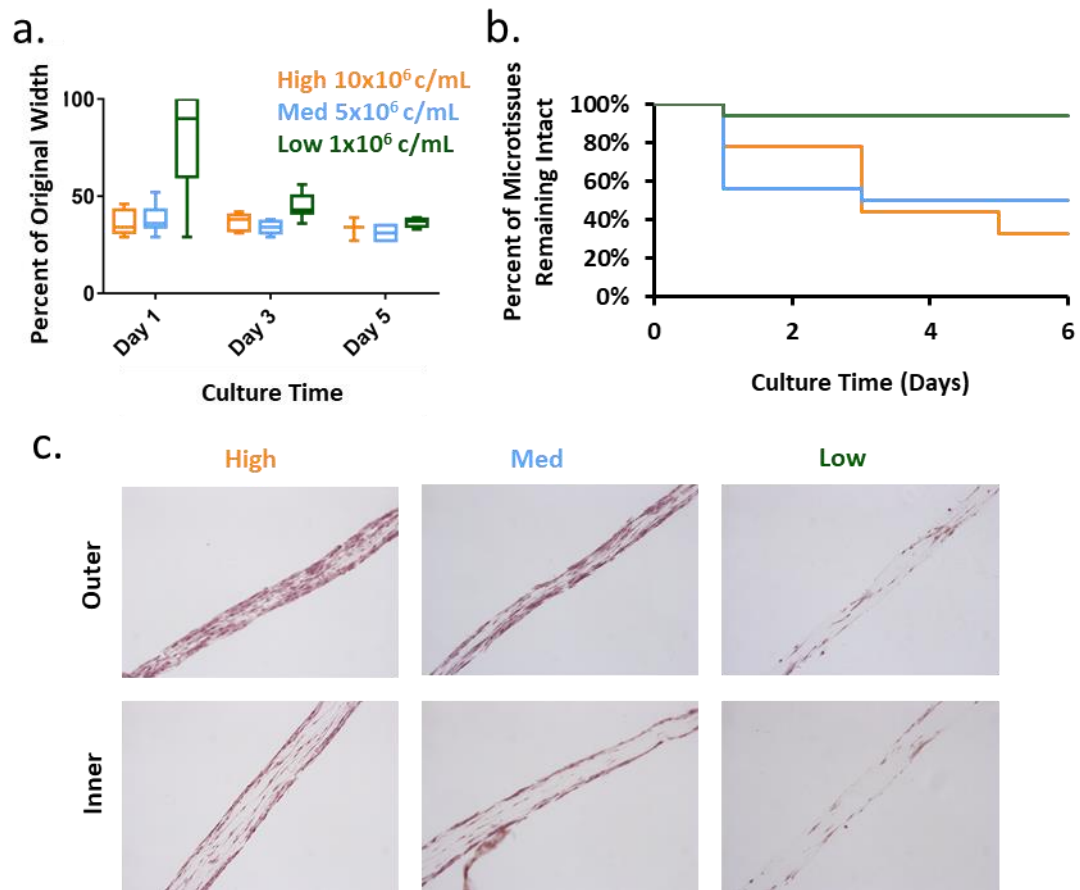


Figure 5-5. Cell Concentration Optimization in "Harp" Molded Tissues.

(a) The compaction of the collagen gel was taken as an indicator of microtissue maturation, and was plotted as a percent change in the tissue from its original width to its current diameter. Increased cell concentration led to faster compaction. (b) Increased cell concentration also led to earlier failure of the microtissues, with at least 50% failure by day 5 in the medium and high cell concentrations. (c) H&E staining shows low cell confluence in all groups, with more cells on the outer surface than in the inner layers.

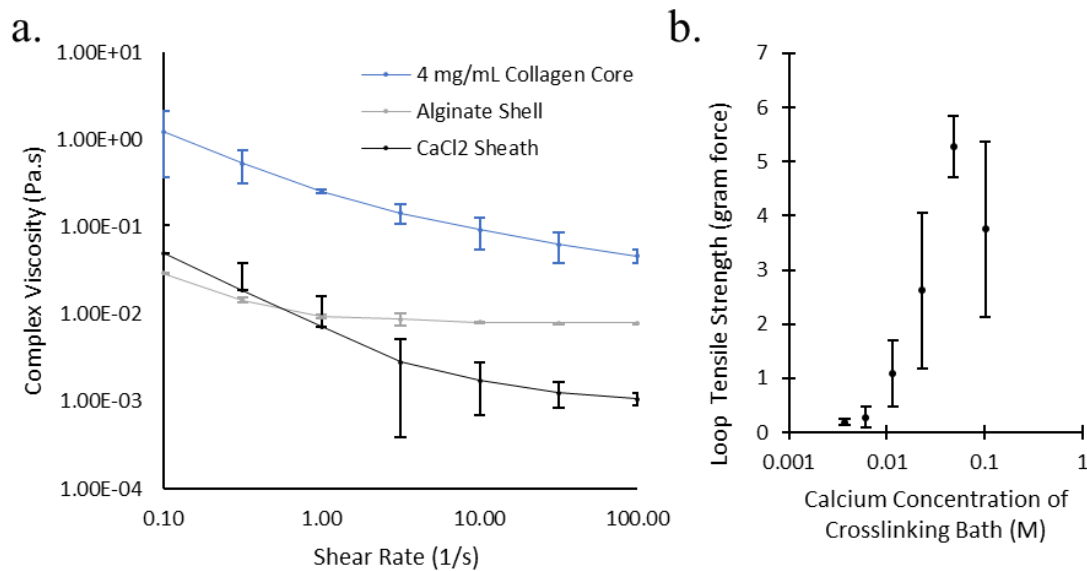


Figure 5-6. Wet Spinning Fluid and Solid Properties.

(a) Viscosity of key spinning solutions as a function of shear rate shows mild shear thinning behavior in all cases, with the lowest viscosities being found in the calcium chloride solution. (b) Ultimate tensile strength of the fiber loops shows increasing strength with increasing calcium chloride concentration in the bath.

6 3D Bioprinting with Pre-Aligned Microtissues

6.1 Introduction

The gastroesophageal junction (GEJ) plays a critical role in disease prevention due to its function as a valve preventing the reflux of caustic stomach contents upwards into the esophagus. Failure of this function can lead to gastroesophageal reflux disease (GERD) and Barrett's esophagus, which is an intestinal metaplasia of the normally stratified squamous esophageal epithelium. Continued exposure can lead to cancer, which frequently necessitates surgical resection [10]. Surgeons are then presented with a new problem – reconstructing the missing esophageal segment. The preferred method is gastric pull-up, in which the stomach is formed into a tube, pulled through the esophageal hiatus into the mediastinum, and anastomosed to the remaining proximal esophagus [11]. This process destroys the normal anatomy of the GEJ, thus predisposing the patient to ongoing reflux events and pulmonary complications [12]. A tissue-engineered solution to reconstitute the GEJ anatomy could greatly decrease morbidity related to this surgery and could provide additional benefits to the treatment of refractory GERD and other diseases of the lower esophagus.

The GEJ has a layered tissue structure like the rest of the alimentary tract, with an inner protective mucosa supported by a submucosa and muscularis externa. Thus, many of the common challenges of tissue engineering, including vascularization and innervation, apply. However, the alignment of the smooth muscle cells within the muscularis externa presents a particular challenge when compared to the rest of the gut tube. The two-layered esophageal muscularis with

an inner circular layer and outer longitudinal layers transition into the three-layered stomach muscularis with an inner oblique, middle circular, and outer longitudinal layer. This transition gives rise to three important components of the high-pressure zone responsible for tight closure of the GEJ, which are the lower esophageal circular sphincter, the gastric sling fibers, and the gastric clasp fibers [50]. The orientations of the cells within these “fibers” are not neatly arranged in a simple coordinate system. Furthermore, there is some evidence that the lower esophageal circular sphincter and the gastric sling fibers could be a single continuous “lasso” of muscle that wraps around the GEJ [55], [56]. Replicating this complex structure presents a challenge for current tissue engineering technology [228].

Creating alignment within tissue-engineered constructs has been of increasing interest in the field. Earlier approaches resulted in the uniaxial alignment of cells by substrate patterning [2], active stretching [3], or mechanical boundary constraints resulting in stress-induced alignment [4]. Combining the principles learned from these studies with new techniques in 3D bioprinting has increased the complexity of the alignment which might be achieved. Extrusion bioprinting, in which a hydrogel bioink is deposited through a nozzle, has been particularly promising for this purpose and has yielded two possible approaches. In one, the macromolecules which make up the hydrogel ink are directed into alignment by controlled material flow during the deposition, guiding cell alignment in the direction of the macromolecular pattern. Another promising approach uses anisotropic microtissues, which are directed into alignment by flow within the extrusion nozzle.

This work presents a novel step towards replicating the complex muscular structure of the GEJ by 3D extrusion bioprinting of pre-aligned microtissues (PAMs). Esophageal smooth muscle cells are combined with collagen to form long fibers of aligned smooth muscle tissue. These fibers are then cut into short (2-4 mm) fragments that are combined with a hydrogel bioink.

Shear-induced alignment of the microtissues through a conical nozzle during 3D extrusion bioprinting results in direct-writing of complex muscular tissue alignment. It is expected that this novel approach, in combination with non-planar bioprinting, could address the challenge of reconstructing the GEJ anatomy.

6.2 Materials and Methods

6.2.1 Cell Culture

Primary human esophageal smooth muscle cells (hESMCs) were purchased from Cell Biologics (H-6089). These hESMCs were immortalized by transduction with recombinant lentiviruses carrying human telomerase (hTERT), cyclin D1 (CCND1), and a variant cyclin-dependent kinase 4 (CDK4R24C) by Capitol Biosciences (Gaithersburg, MD). All genes were transduced in combination with a TET-ON system. These immortalized cells (ihESMCs) were cultured on gelatin-coated tissue culture plastic at 37°C and 5% CO₂ with high-glucose Dulbecco's Modified Eagle's Medium (DMEM) (Gibco 11965-092) supplemented by 10% FBS (Genesee Scientific 25-514), 100 µg/mL Primocin (Invivogen ant-pm-2), and 2µg/mL doxycycline hyclate (Sigma-Aldrich D9891). Doxycycline was only added during cell expansion culture, and not during fiber production or maturation steps. Cell harvest and passage was accomplished by incubation with TryPLE (Gibco, 12563011.). Experiments were performed with cells at passages 5-10. Mycoplasma testing was performed at 6-month intervals and found to be negative.

6.2.2 Microfluidic Spinning Device

Microfluidic devices were created by 3D printing with a Form 3B SLA printer using Surgical Guide Resin v1 (Formlabs RS-F2-SGAM-01). The design featured three fluid channels which converged into two spinnerets in series. Fluids from channels 1 and 2 flowed together at spinneret 1 to form a core/shell flow with fluid from channel 1 in the core. This flow was focused down

into spinneret 2, which injected it into the fluid flow from channel 3. The spinneret features were designed with a 600 μm inner diameter and 200 μm wall thickness and were centered in an outer channel with a diameter of 2 mm. Slicing was performed in PreForm (v3.28.1) with a layer height of 50 μm . Devices were oriented on the build plate to point directly downward, allowing the greatest precision for manufacturing of the key 600 μm channels. Default settings were used except for switching to micro-rafts and 0.45mm touchpoints, which were edited for placement as needed to avoid obstructing fluid inlets. Printing was carefully monitored to allow for immediate cleaning of the devices in 99% isopropanol to remove the uncured resin. Supports were removed, and clean isopropanol was flushed vigorously through all channels in forward and reverse. Parts were immediately dried with compressed air to remove any alcohol in the channels. Visual inspection confirmed a clear and circular central channel. Post-curing was performed in a Form Cure device (Formlabs) at 60°C for 30 minutes. Devices were sterilized by autoclaving at 121°C. To measure internal dimensions of the finished device, three samples were examined by a XT H 225 (Nikon) μCT scanner and reconstructed with CT Pro 3D XT (v3.1.11, Nikon) software. Segmentation of the resultant files was performed in 3D Slicer (v5.2.2) [229], [230], and diameter measurements were performed in FIJI. Visual mapping of printed component deviation from the computer model of the devices was performed with CloudCompare (v2.12.4) [231].

6.2.3 Microtissue production

Smooth muscle PAMs were prepared by the inclusion of a cellular collagen hydrogel core into a calcium alginate fiber. The microfluidic spinning device was attached by flexible tubing to syringes containing core, shell, and sheath solutions. The sheath solution for crosslinking the alginate consisted of 100mM CaCl_2 and 3% (w/v) sucrose. The shell solution contained 1.5% sodium alginate (Wako Chemicals, 194-13321) with or without 100 $\mu\text{g}/\text{mL}$ erioglaurine dye (Sigma-Aldrich 861146-5G). Both the sheath and shell solutions were sterilized

by autoclave. These solutions were loaded into syringes and connected to the microfluidic spinning device and the fluid lines were manually primed prior to beginning production of the core solution, but care was taken to avoid letting the solutions contact each other in the device until the spinning process was started. The core solution was prepared by mixing sterile bovine collagen (TeloCol 10, Advanced Biomatrix, 5226) with a neutralizing buffer to yield a pre-gel solution at the desired concentration. This was immediately mixed with a cell pellet containing the desired number of cells. This solution was gently pipetted to mix the cells, then loaded into a syringe and immediately put into an ice water-cooled jacket mounted on a syringe pump to prevent premature gelation. The core was connected to the spinning device and the tubing was manually primed.

The tip of the spinning device was placed just below the surface of a collecting bath containing 10mM CaCl₂ and 290mM NaCl in water. The syringe pumps were engaged sequentially, starting with the alginate shell. Once the shell solution reached spinneret 2, the sheath solution was started. Any initial plug was cleared with sterile forceps and when the alginate fiber production was stable, the core solution was introduced. As the fiber was produced, it was wound using a custom-built motorized spooling device. The fiber was collected on a sterile 2-pronged spool that was detached from the device after the spinning process and the collected fiber was placed in petri dishes and covered with culture medium. For smaller fiber batches, the fiber was not wound onto spools but was transferred to culture vessels using sterile forceps. The fibers were incubated at 37°C and 5% CO₂ for tissue development. Media was replaced every 2 days. For cultures containing loose, unwound fibers, aspiration of spent media was performed through a 40 µm cell strainer to prevent accidental loss.

Once the cells had formed long strands of aligned tissue, the fiber spool was transferred to a dish with sterilized microscope slides. The fibers were released from the spool with two cuts

along the ends of the spool. The microscope slides were transferred to a sterilized cutting guide, which was 3D printed using FormLabs Surgical Guide resin. This guide allows a razor to pass through every 2 mm. Sterilized single-edge razor blades were used to cut the fibers at the desired lengths and the resulting fiber fragments were transferred to fresh culture medium in the incubator to recover.

The cut tissue fragments were released from their alginate shells to yield the PAMs. Alginate lyase (Sigma-Aldrich, A1603) was prepared and aliquoted as a stock solution of 4mg/mL and stored at -20°C. This was diluted 1:100 in culture media to dissolve the alginate shell over the course of 1 hour at 37°C in the incubator. Prior to and during the shell removal, the fiber fragments were incubated for 1 hour in 50 µM Y-27632 (Cayman Chemical 10005583), a ROCK inhibitor, or 5 µg/mL cytochalasin D (Sigma 2618), a cytoskeletal toxin, to temporarily prevent fiber shortening during the printing process.

6.2.4 Unaligned Controls

iheSMC gels were produced as 3D unaligned controls for comparison to the aligned cell fibers. Cells were prepared in collagen in the same manner as the fiber core, then 10 µL droplets were pipetted into petri dishes. The dishes were incubated at 37°C for 20 minutes before adding culture media.

6.2.5 Immunofluorescence Microscopy

Wide-field epifluorescence was captured with an EVOS FL Auto 2 (Thermo Fischer). Confocal microscopy was performed with a Nikon A1Rsi laser scanning confocal microscope. Nuclear counterstaining was accomplished by treatment with DAPI in DPBS at 5µg/mL for 15 minutes, followed by two 15-minute washes with DPBS. Samples were fixed for 45 minutes with 4% paraformaldehyde at room temperature, then washed 2X for 5 minutes with DPBS and stored at 4°C for analysis. The samples were processed in a modified protocol similar to a previously

described protocol for spheroids [232]. Briefly, samples were washed with a penetrating buffer (20% DMSO, 0.2% Triton X-100, 22.5 mg/mL glycine) for 30 minutes at RT, then blocked for 2 hours at RT with a blocking buffer (10% DMSO, 10 mg/mL BSA, 0.2% Triton X-100). All buffers were made in DPBS. Primary antibodies were added to antibody diluting buffer (5% DMSO, 10 mg/mL BSA, 0.2% Tween 20) and incubated at 4°C overnight. Antibodies used were anti-alpha Smooth Muscle Actin (Sigma, A5288) diluted 1:100. A buffer (10 mg/mL BSA, 0.2% Tween 20) was used to wash the samples 5 times for 5 minutes each before adding secondary antibodies or phalloidin and DAPI (5 ug/mL) diluted in antibody dilution buffer overnight at 4°C. Secondary antibodies conjugated with Cy3 (Jackson ImmunoResearch, 711-165-152) and iFluore488-conjugated phalloidin (Cayman Chemical, 20549) were diluted at 1:500. Samples were washed 5 more times before imaging in DPBS.

6.2.6 Cell Viability

Cell viability in 3D constructs was assessed using LIVE/DEAD (Invitrogen, L3224) staining. Cell fibers (day 7 of incubation) were cut using a razor and cutting guide into 4 mm segments. These PAMs were cultured in media for 1.5 hours. Dead controls were prepared by incubation in methanol for 30 minutes. Samples were washed in DPBS (+Ca) for 5 minutes. Samples for quantification were incubated in ethidium homodimer at 4 μ M in DPBS (+Ca) for 30 minutes at room temperature to label the nuclei of dead cells. Samples for qualitative imaging were also incubated in Calcein AM at 2 μ M to label live cells. Epifluorescence imaging was performed immediately after staining. Using FIJI, the average PI signal was measured from the cut tissue ends along the length of the tissue, binning into regions of interest 50 μ m along the long axis of the fiber and 200 μ m wide. This measurement process was also applied to dead controls, unstained dead controls, and the uncut central region of the living PAMs.

The potential effect of erioglaucine blue dye on iheSMC viability was screened using a CellTite-Glo® 3D (Promega, G9681). iheSMCs were cultured at 10^4 cells/cm² in gelatin-coated 12-well plates in culture medium with various concentrations of erioglaucine dye for 48 hours. Samples were rinsed 3X with 1 mL plain DMEM, then incubated with 0.3 mL DMEM and 0.3 mL CellTiter Glo 3D reagent for 5 minutes. 200 μ L of each sample was transferred to a opaque-walled 96 well plate and luminescence was measured using a Cytation 3 (BioTek) plate reader.

6.2.7 Bioink Formulation

The bioink was formulated as two 2X solutions which were mixed prior to printing. In the first solution, hyaluronic acid (Sigma 53747-1G) was dissolved at 7.5 mg/mL in DMEM with 10% FBS and 100 μ g/mL Primocin, stirring at 50°C overnight. This solution was diluted with 20% glycerol (Sigma-Aldrich, G9012) with stirring at 50°C for 1 hour. Lyophilized gelatin methacrylate (production described previously [233]) was dissolved at 100 mg/mL at 50°C for 1 hour, then lithium phenyl-2,4,6-trimethylbenzoylphosphinate (LAP) photoinitiator was dissolved at 10 mg/mL. This solution was stored at -20°C until the day of use. The second solution was made by dissolving bovine fibrinogen (Sigma-Aldrich, F8630-1G) at 30 mg/mL in pre-warmed 37°C DPBS for 1 hour without agitation on the day of use. The two solutions were combined at 37°C and mixed by pipetting to yield the final bioink, which was sterile filtered with a 0.22 μ m PVDF syringe filter.

6.2.8 Rheometry

Rheometry was performed on a DHR-3 (Texas Instruments) rotational rheometer with a 2° 40mm cone and plate geometry on a Peltier heating/cooling base. Collagen working time at 4°C and gelation time at 21°C were investigated by oscillatory shear under controlled torque of 10 μ N·m. 2 minutes was allowed for mixing of ice-cold collagen and neutralization buffer and for loading

prior to beginning the test. After 30 minutes of testing at 4°C, the temperature was increased to 21°C and the oscillation continued for 30 additional minutes. The gelation point was determined by the crossover of the storage (G') and loss (G'') moduli.

6.2.9 3D Bioprinting

Fibers were incubated and were processed into 4 mm PAMs for bioprinting on Day 8. Following treatment with Y-27632 and release from the alginate shells, the PAMs were centrifuged at 100g for 5 minutes in 50mL conicals to collect the tissue, which was then transferred into a 5mL conical in media and recollected at 100g for 1 minute. After this washing step, the total tissue volume was estimated using the volumetric markings on the conical tube. To this tissue volume, 4 volumes of bioink were added at 37°C and was mixed by pipetting, resulting in approximately 20% tissue volume. This was transferred to a 3mL pneumatic printing syringe barrel and a barrel wiper was added, leaving an equal volume of airspace to the bioink. The capped barrel was immersed in ice and was gently rocked by hand every 15 seconds to reduce settling of the PAMs in the bioink until the ink solidified. Then, the wiper was advanced to remove any airspace, a 20ga tapered tip was added, and the syringe was placed into a temperature controlled printhead on a Bio X (CellInk) bioprinter at 21°C. After 10 minutes, printing was performed using nitrogen pressures of 20-30kPa, which was adjusted to ensure smooth extrusion with approximately 1mm path width at 4 mm/sec movement speed. After printing, the constructs were crosslinked by UV light (405 nm) for 5 seconds, then incubated in 20 U/mL bovine thrombin (Sigma, T7513) in culture medium for 30 minutes at room temperature. Finally, fresh culture medium was added and constructs were placed in the cell incubator at 37°C and 5% CO₂.

6.2.10 Cell and tissue alignment

Cell fibers and unaligned controls were labelled with DAPI and phalloidin to show the cell structure upon confocal microscopy. Maximum intensity projections of the resultant z-stacks were calculated with FIJI. Image processing of whole images of the phalloidin signal through the OrientationJ plugin produced color-coded images in which the color corresponds to directionality of the pixels and saturation corresponds to the coherence. Regional orientation was quantified using the OrientationJ plugin's distribution function, which was applied to 100x100pixels (62x62um) square randomly generated regions of interest along the length (x-axis) of the fiber or within the whole region (x and y axes) of images of the unaligned controls. The local window sigma value was 2 pixels, which was used with the cubic spline method in the plugin. Likewise, color-coded images of the printed constructs stained with phalloidin, but with a sigma value of 10 pixels. These images were captured by the area-scanning mode of the EVOS epifluorescence microscope, and were background subtracted prior to color-coding using FIJI's rolling ball subtraction algorithm and a radius of 100 pixels (originals in supplement).

6.2.11 Statistical Analysis

All statistical tests were performed in JMP v15 (SAS). Where normally distributed data was compared to known or desired value, two-tailed t-tests were used to test for a difference. Any cases of multiple comparisons were analyzed by ANOVA with post-hoc comparisons using Tukey's Honest Significant Difference test to control the family-wise error rate ($\alpha = 0.05$). Linear regressions were performed as least squares regressions with an alpha of 0.05 and a stepwise process for elimination of non-significant factors.

6.3 Results

6.3.1 Spinning Device Characteristics

The 3D printing process to produce the microfluidic spinning devices successfully created the mesoscale internal geometries required for spinning cellular fibers. Semi-quantitative analysis using CloudCompare demonstrated that the μ CT scans of the microfluidic devices generally conformed to the solid model used to create the printer input, although the interior walls tended to have an offset of 0 to 0.1 mm, leading to slightly smaller channels than expected (Fig. 6-2a). The internal key diameters are the internal and external diameters around the interior microfluidic spinnerets (Fig. 6-2b). The internal diameter of 3 devices was 454 μ m (SD = 68 μ m), an offset of 145 μ m from the planned 600 μ m ($p < .0001$, $n = 15$). The external diameter was 1920 \pm 24 μ m, which was 80 μ m smaller than the 2000 μ m planned diameter ($p < .0001$, $n = 15$). Multiple devices could be printed simultaneously, but it was observed that the success rate increased with decreased total print time and immediate, vigorous washing.

Flow rates of the three solutions through the device had a predictable effect on the resulting fiber dimensions. Increasing the total fiber flow rate (combination of core and shell flows exiting the distal spinneret) increased the diameter of the produced fiber while increasing the sheath flow rate led to a diameter decrease (Fig. 6-2c). An equation to predict total fiber diameter (FD) based on total fiber rate (FR) and sheath rate (SR) was calculated by stepwise regression. The regression model ($F(2,41) = 42.13$, $p < 0.0001$, $R^2 = 0.73$) is reported in Eq. 6-1.

$$\text{(Eq. 6-1)} \quad FD = 488.95 - 43.05 SR + 659.19 FR - 362.86 FR^2$$

Likewise, varying the core and shell components had a predictable effect on the composition of the fiber. Three different core-shell ratios were tested at three different fiber/sheath ratios. The core and shell diameters were measured with FIJI on phase contrast images of the fibers. The diameters were converted to area measurements assuming a circular

fiber. As a simple approximation, it was expected that the area ratio (AR) would be proportional to the flow ratio (FR) between the two convergent streams (Fig. 6-2d). A linear model of this form was found to be significant ($F(3,140) = 371.43$, $p < 0.0001$, $R^2 = 0.72$). The resulting equation is shown in Eq. 6-2.

$$\text{(Eq. 6-2)} \quad AR = 0.82 FR - 0.03$$

6.3.2 Fiber Shell and Core Properties

The cellular fibers produced by the spinning process were difficult to see while in solution. The addition of erioglaucine disodium salt (Blue #1) was found to improve visibility, which increased the ease of handling during the spinning process. Visibility increased with increasing dye concentration (data not shown). Concentrations up to 100 μM did not significantly affect the total [ATP] in cell culture compared to no-dye control, but 1000 μM caused a significant decrease (Fig 6-2e). This indicates the cell viability and metabolism was unlikely affected by lower concentrations of erioglaucine.

The collagen solution used to make the core was tested for working time and viscoelastic mechanics. It was found that a neutralized 5 mg/mL solution could be maintained in a liquid state for at least 30 minutes at 4 °C (Fig. 6-2f). After this working time, the gelation time was found to be 9.3 minutes (SD = 0.5 min). After 20 minutes, the G' was 997.3 Pa (SD = 25.4 Pa), and G'' was 108.2 Pa (SD = 8.4 Pa).

6.3.3 Fiber Spinning Parameters

Based on the previous results, the typical flow rate for all following experiments was set to 50 $\mu\text{L}/\text{min}$ core, 500 $\mu\text{L}/\text{min}$ shell, and 5 mL/min sheath. The effects of collagen and cell concentrations were investigated at cell concentrations of 1, 10, 30, and 100 million cells added to 1 mL of 4, 5, or 6 $\mu\text{g}/\text{mL}$ collagen gel (Fig 6-7). Collagen concentrations below 5 $\mu\text{g}/\text{mL}$ resulted in instability and collapse of the fiber into cell clusters contained within the alginate shell, except

in the case where the cells were at a low (1 million:1 mL) density (Fig. 6-2j-1). The typical concentrations for all following experiments were set to 30 million cells: 1 mL of 5 $\mu\text{g/mL}$ collagen. It was found that a fiber “run” could be conveniently planned using 1 mL of core, 10 mL of alginate shell, and 100 mL of sheath solution. The longest recorded continuous fiber was >80 m (estimated from rotation count of the spool), but these typical production runs resulted in approximately 30 m of fiber.

6.3.4 Morphology in Cellular Fibers

Maximum intensity projections of the fibers DAPI and phalloidin signals (Fig. 6-3c,d) demonstrate a high degree of alignment in both the nuclei and actin cytoskeleton compared to the unaligned control (Fig. 6-3d,f). This is especially evident in the phalloidin, where the color-coded images of the fiber are largely monochromatic, compared to the full spectrum visible in the unaligned control. Quantification of randomly selected regions of interest (boxes on Fig. 6-3e,f) were averaged and the mean and standard deviation ($n=10$) are plotted in figure. 6-3g. The primary axis set at zero degrees is taken as the long axis of the cell fiber, and the cells are strongly aligned along this axis in the fiber samples.

6.3.5 Effect of Cutting on PAMs

The 3D-printed cutting guide allowed for the cell fibers to be cut into nominal lengths of multiples of 2 mm. Acellular alginate fibers cut to 2, 4, and 6 mm nominal lengths were measured and found to have mean lengths of 1.98 mm (95% CI [1.68, 2.29]), 3.16 mm (95% CI [2.68, 3.67]), and 4.91 mm (95% CI [4.35, 5.46]), $n=30$, (Fig. 6-4a), respectively.

Inhibition of contraction to preserve PAM length was tested using 2 mm cut PAMs (Fig. 6-4b). Once cut and released from the alginate shell, the untreated PAMs quickly contracted to 32% of their original length ($n=11$). Pre-treatment by cytochalasin D prior to addition of alginate lyase and continued treatment during the lyase incubation produced longer PAMs, only contracting to

55% of their original length. Likewise, Y-27632 reduced the contraction, resulting in 49% preservation of the original length.

When cut, it was found that the cells at the ends of the PAMs had increased uptake of ethidium homodimer localized to the nuclei of the damaged cells. Quantification of the fluorescence signal along the length of the tissue showed that the damage was contained to the first 250 μm from the end of the PAM. (Fig. 6-4e). Representative images of the dead control and cut ends of the PAMs are shown in figures 6-4 f and g, respectively. Compared to the methanol-treated dead control, the average ethidium homodimer signal was significantly lower even at the cut ends, indicating sub-total cell death in the PAMs where the cut was made. This correlates with qualitative imaging of the tissues co-labeled with calcein AM, which shows live cells are still present at the end of the tissue (Fig. 5-4h).

6.3.6 3D Bioprinting with PAMs

Three patterns were printed with the BioX to demonstrate alignment of the PAMs by the printing process. An inside-outward print of progressive circles, a single-layer raster, and a two-layer perpendicular raster. The single-layer raster was produced by truncation of the full two-layer raster code. The paths of the circular and two-layer prints are depicted in figure 6-5a, b, and c. Paraformaldehyde fixation and phalloidin labelling of the f-actin in the printed constructs immediately after the thrombin crosslinking revealed the arrangement of the PAMs within the structure. OrientationJ color mapping was applied to the phalloidin images. In the circular print, a full spectrum of colors is found as the PAMs follow the circular paths (Fig. 6-5e,h). The single-layer raster shows predominantly red hues due to the bulk of the microtissues aligning with the y-axis, except near the edges (Fig. 6-5f,i). The two layer print shows a lower layer of y-axis alignment with red hues and an upper layer of x-axis alignment colored blue/green (Fig. 6-5g,j).

In each image, there are points where knots or clumps of the PAMs interfere with the tissue alignment.

6.4 Discussion

Various tissues throughout the body rely on highly ordered cell alignment for proper function, especially muscle tissue due to the need for force summation of the cells for efficient deformation. The gastroesophageal junction represents both an unmet clinical need in tissue engineering and a challenging structure to replicate in terms of the alignment of the bundles of smooth muscle which impart its valve-like function. Despite the growing number of processes by which cells can be uniaxially aligned, the complex structure at the GEJ necessitates an approach capable of producing alignment in multiple non-orthogonal planes. 3D bioprinting of PAMs could be such an approach.

Of all the available 3D bioprinting methods, extrusion bioprinting has proven to be an easily implemented method that balances the need for precision and manufacturing speed. Moderate viscosity and yield stress hydrogel bioinks are forced through a nozzle by gas pressure, plungers, or rotating screws. The width of the extrusion is typically between 100 and 1000 μm . The popularity of this method has led to multiple modifications attempting to guide cell alignment. An increasingly common strategy is to cause macromolecular alignment of collagen fibrils along the print direction [234]–[236]. This phenomenon has been observed as both by increasing shear rate and imposition of an extensional flow regime during deposition [236]. A related approach has used a “sewing”-like method to prestress a gelatin-based bioink during the printing process, resulting in a high degree of both macromolecular and cellular alignment [237]. Extension of the concept of printed alignment into the mesoscale domain was demonstrated by extrusion printing of densely packed hydrogel microstrands, which became moderately entangled during the printing process but resulted in overall alignment with the printing direction [238].

Recently, a similar approach to the PAM printing presented here was shown with induced pluripotent stem cell derived cardiomyocytes. Microtissues produced by suspension between silicone cantilevers resulted in “dumbbell” shaped microtissues, which aligned well with the printing path and produced significant anisotropy in macroscopic contraction of the printed tissues [239].

The first challenge for implementing the PAM printing method is efficient production of highly aligned microtissues. While suspension between cantilevers has been used frequently in the past, our experience with this in preliminary studies found it to be a challenging method to scale up (data upon request). Production of meter-long cellular fibers through microfluidic core-shell encapsulation showed that smooth muscle-like cells could align during fiber maturation [240]. In this work, the fiber spinning device was modified to be produced by stereolithography printing, which allowed for rapid iteration of prototypes with low time and cost. The resulting spinning system produced tunable fiber properties based on flow rates. The fiber method lends itself to scaled-up production, as no custom molds are required. Although the longest cellular fiber produced in this work was at least 80 meters long, modifications to the system could theoretically allow for significant increases in length and a corresponding increase in the number of PAMs produced. Due to the extreme length of the fibers, a motorized spooling device was created that both increased the ease of handling and maintained the fibers in macroscale alignment for eventual cutting into PAMs. The high degree of cellular alignment within the fibers and small amount of cell death associated with the cutting process confirms that this approach could be a path towards large-scale production of PAMs for bioprinting. When printed at low density in a photocrosslinkable bioink, which was modified from a previously published ink for skeletal muscle printing [241], the PAMs generally aligned with the printing direction. In future

work, it is expected that combining this printing method with non-planar printing in a support bath will facilitate the creation of GEJ-like constructs.

The new fiber spinning approach demonstrated here likely outperforms the previously published cardiac dumbbell microtissue method in a few ways. The dumbbell approach used combinations of iPSC-derived cardiomyocytes and fibroblasts suspended in a 1 mg/mL collagen hydrogel supplemented with 1.25mg/mL fibrinogen. To harvest from the micropillar arrays, it was necessary to leave the micropillars without a retaining cap. This produces an undesirable failure mode by which the microtissues can slip off of the micropillars by deflecting the pillars inward, which resulted in approximately 50% failure rate after 5 days of development. Thus, tissue harvesting was performed at day 3 of development, where most of the microtissues were still adhered. In the new fiber spinning method, stable fibers can be produced with greater development times. While we observed stable fibers out to at least 2 weeks, other groups have maintained fibers for over a month. This is anticipated to allow for more mature tissue development than micropillar molding. Our own experience with similar molding approaches found similarly high failure rates over a 6-day period, leading us to develop the fiber spinning approach.

The scalability of fiber spinning is greater than that of molding due to decreased raw material input, increased packing density, and options to multiplex multiple spinnerets. While the molding approach requires a long double-molding process to make the required plates, wet spinning only requires common syringe pumps and a reusable spinneret device, which we have demonstrated can be rapidly prototyped by stereolithographic printing. Improved process efficiency is realized by the inclusion of a low-cost spooling device to manage long fiber production. The spooled fiber represents a 3D packing density not possible with molding, since

the molds are manufactured as a single layer. The molding approach allowed for 1050 microwells per well plate, with each tissue being 2mm in length. In comparison, an equivalent number of microtissues could be produced by 2.1 meters of wet-spun fiber. As the spinning process typically produced ~30m of fiber per production run (15,000 microtissues at 2 mm cut length) which was stored in a 100 x 25 mm petri dish, the typical microtissue density was approximately 76 microtissues per cubic centimeter during incubation. It has been observed that significantly greater cellular fibers (>80 μ m) can be placed similarly into such a dish, increasing its packing efficiency. This is compared to a 85.9 x 128.0 x 17.3 mm volume of the molding approach, yielding approximately 6 microtissues per cm^3 . Thus, the manufacturing efficiency in terms of required volume is at least 10 times greater with the fiber spinning method. Similarly, it is expected that the production rate will be increased by the wet spinning method, since spinnerets could be multiplexed to form spinning arrays that produce multiple fiber simultaneously. Actual maturation time of the tissues cannot be directly compared between the methods at this time due to the differences in cell types included, but it is expected that the time in incubation to form mature microtissues is comparable between the methods.

Finally, there is a difference between the molding and spinning methods in the morphology of the microtissue ends. In the molding method, an empty space surrounded by seemingly unaligned tissue disrupts the desired alignment pattern. However, the fiber spinning approach requires cutting living cells, which causes damage to the tissue at the ends out to 250 μ m from the cut. While this is an unfortunate reality, the damage is sub-total and does not result in the same unaligned structure at the tissue ends. Further studies will be required to compare the fusion behavior of these two microtissue bioprinting approaches during maturation of the printed tissue constructs.

There are limitations to this study with respect to cellular biology and the bioprinting process. First, the iHESMCs used here, while convenient for their greatly increased expansion potential in 2D culture, will not be appropriate for tissue-engineered treatments. Future work will ideally utilize induced pluripotent stem cells differentiated to a smooth muscle lineage for histocompatibility with treated patients. Second, increased tissue density, optimization of tissue length, and optimization of bioink parameters are necessary for the ideal implementation of this method. For all discussed methods of bioprinting cell alignment, questions remain as to how robust the alignment will be to complex forces that may be experienced within a bioreactor or post-implantation into a patient. Whether pre-maturation of microtissue fragments may be beneficial to faster tissue development and preservation of alignment compared to methods based on matrix-based alignment cues remains to be seen. These questions, as well as combination with non-planar 3D bioprinting techniques, will be addressed in future work.

6.5 Conclusion

In this work, we present a novel process by which the complex muscular alignment found within the gastroesophageal junction may eventually be recreated. Immortalized smooth muscle cells can be formed into aligned tissue by entrapment within a core-shell fiber. This fiber can be cut into fragments, producing microtissues which can be combined with a bioink and extruded by a 3D bioprinter in a manner resulting in alignment of the microtissues and the cells contained within. This work may be extended to other tissues where alignment is key to normal function.

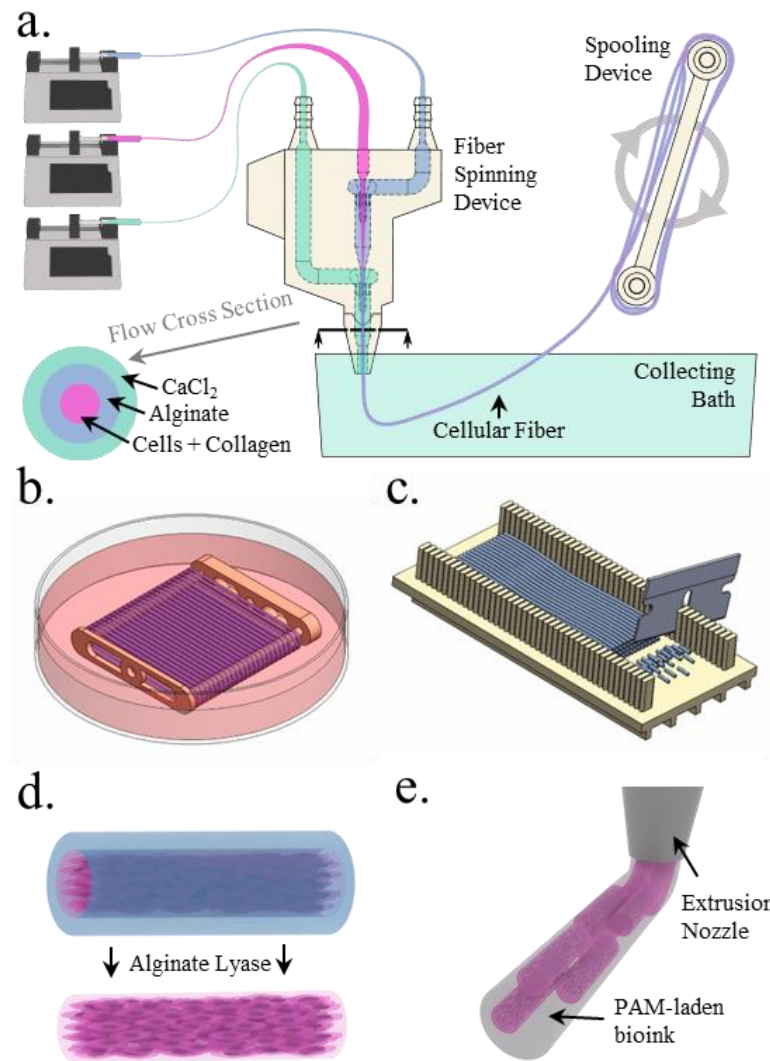


Figure 6-1: Method for production and bioprinting of PAMs

(a) Cellular collagen solution, alginate solution, and CaCl_2 solution are combined in a spinning device to form a solid core-shell fiber, which is wound on a motorized spool. (b) The spool is detached from the motor and the immature fiber is cultured in a dish to form an aligned cellular fiber. (c) The mature fiber is removed from the spool and laid in a cutting device, where it is cut into consistent fragments. (d) Alginate lyase removes the shell from the fragments, releasing the PAMs. (e) PAMs are combined with hydrogel bioink and extruded to lay down the PAMs in alignment with the printing direction.

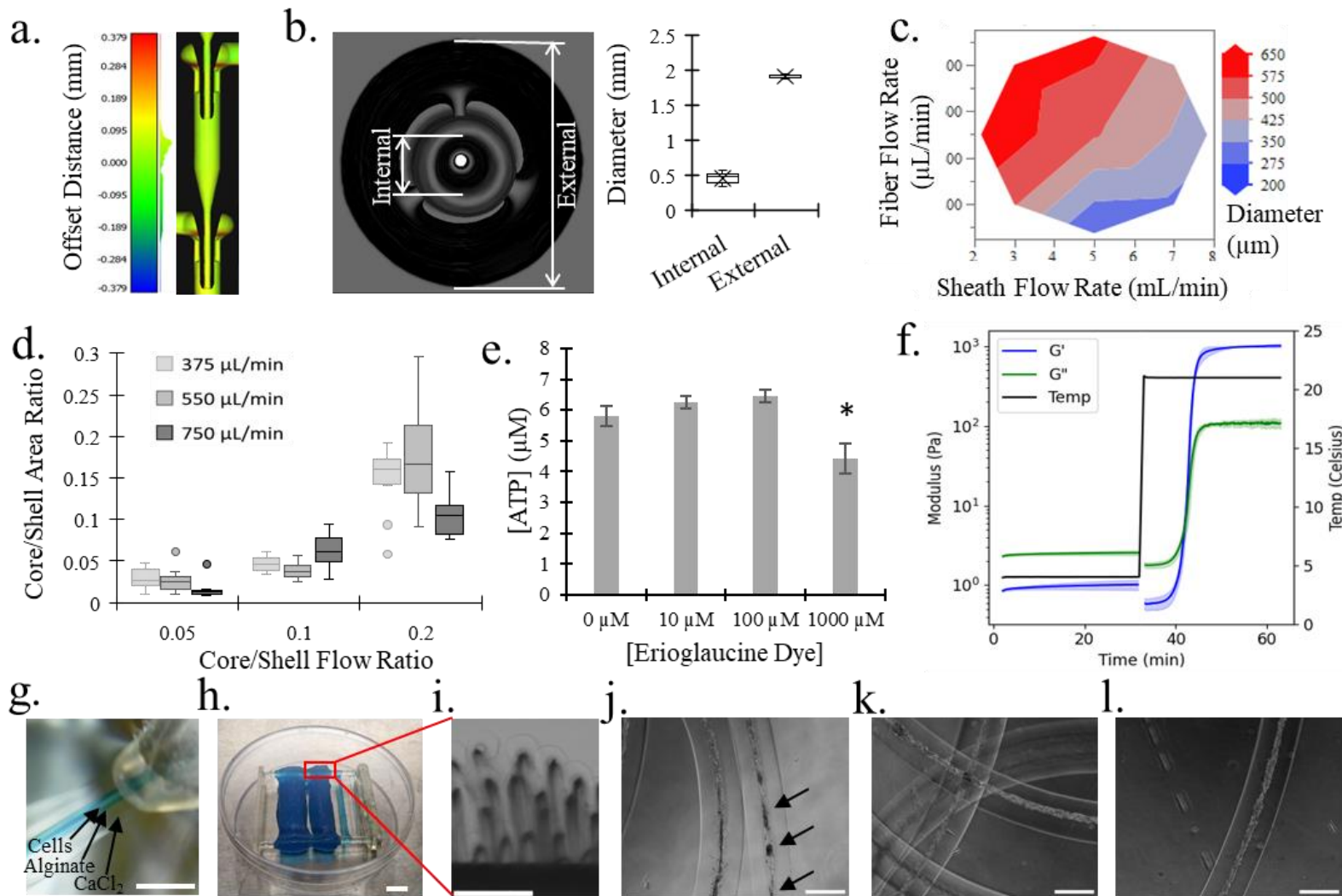


Figure 6-2: Characteristics of the Fiber Spinning System.

(a,b) μ CT of the 3D printed spinning device shows faithful reproduction of the modeled geometry with interior dimensions slightly narrower than designed, including at key diameters in the spinneret region. (c) Total diameter of the spun fiber increases with fiber flow rate and decreases with sheath flow rate. (d) The fiber cross-section is dependent on the ratio of core and shell flow rates. (e) Addition of erioglaucine dye to culture media resulted in less ATP (* $p < .001$) at a 1000 μ M dye concentration compared to all lower concentrations. (f) When maintained cold, the collagen solution has at least 30 minutes of working time for the spinning process and quickly forms a gel when warmed to room temperature. (g-i) The core stream of cells is trapped in the calcium alginate shell and can be wound on a flat spool to maintain alignment of the fibers during incubation and cutting. (j) With a cell concentration of 10 million cells per mL, the 4 μ g/mL collagen gel core resulted in an unstable fiber that began breaking into clusters (arrows) by day 7, unlike fibers made with (k) 5 and (l) 6 μ g/mL collagen cores. Scale bars (g) 2 mm, (h) 10 mm, (i) 1 mm, (j, k, l) 500 μ m.

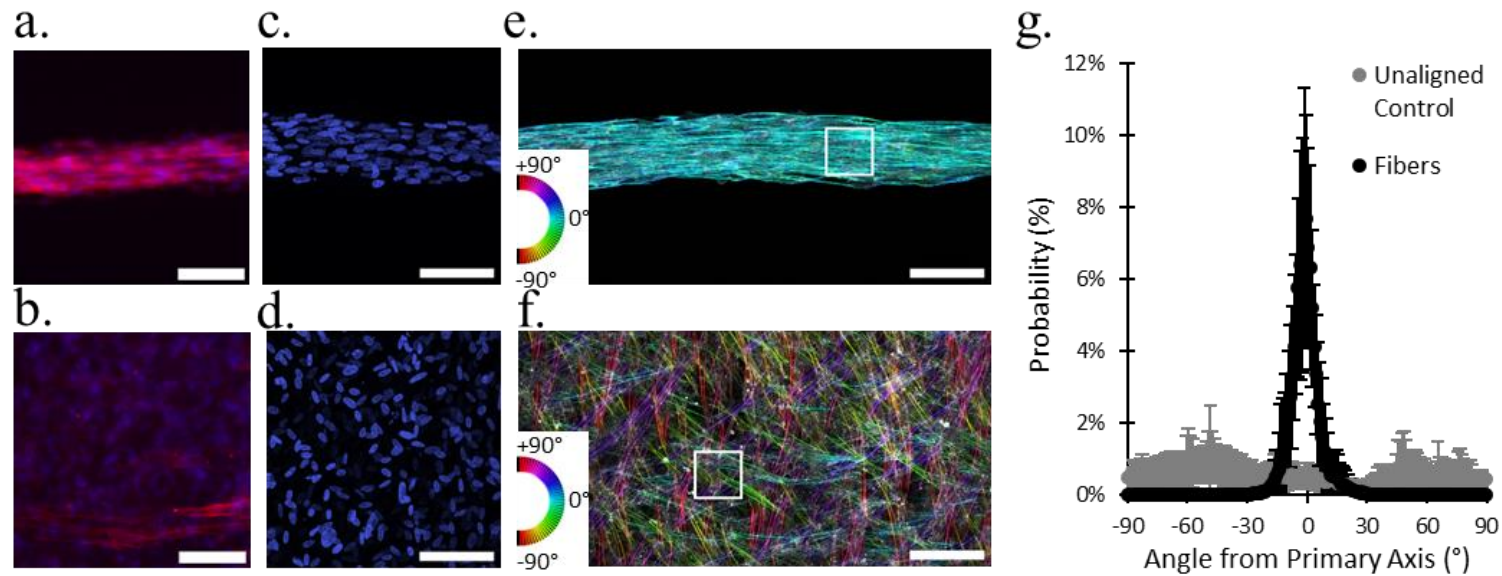


Figure 6-3: Cell alignment and protein expression.

Alpha-smooth muscle actin (red) and nuclei (blue) of (a) aligned fiber and (b) unaligned control imaged with epifluorescence microscopy. Confocal imaging of nuclei in the (c) aligned fiber and the (d) unaligned control demonstrate elongation but only directional alignment in the case of the aligned fiber. False-colored phalloidin labelling showing the alignment of actin fibers with color-coded directionality shows cytoskeletal alignment in the (e) fibers but not in the (f) unaligned control. (g) The probability density of alignment within regions of interest (representative white box insets on (b,d)) shows strong alignment of the cytoskeleton in the fiber (n=10 regions of interest). Scale bars 100 μ m.

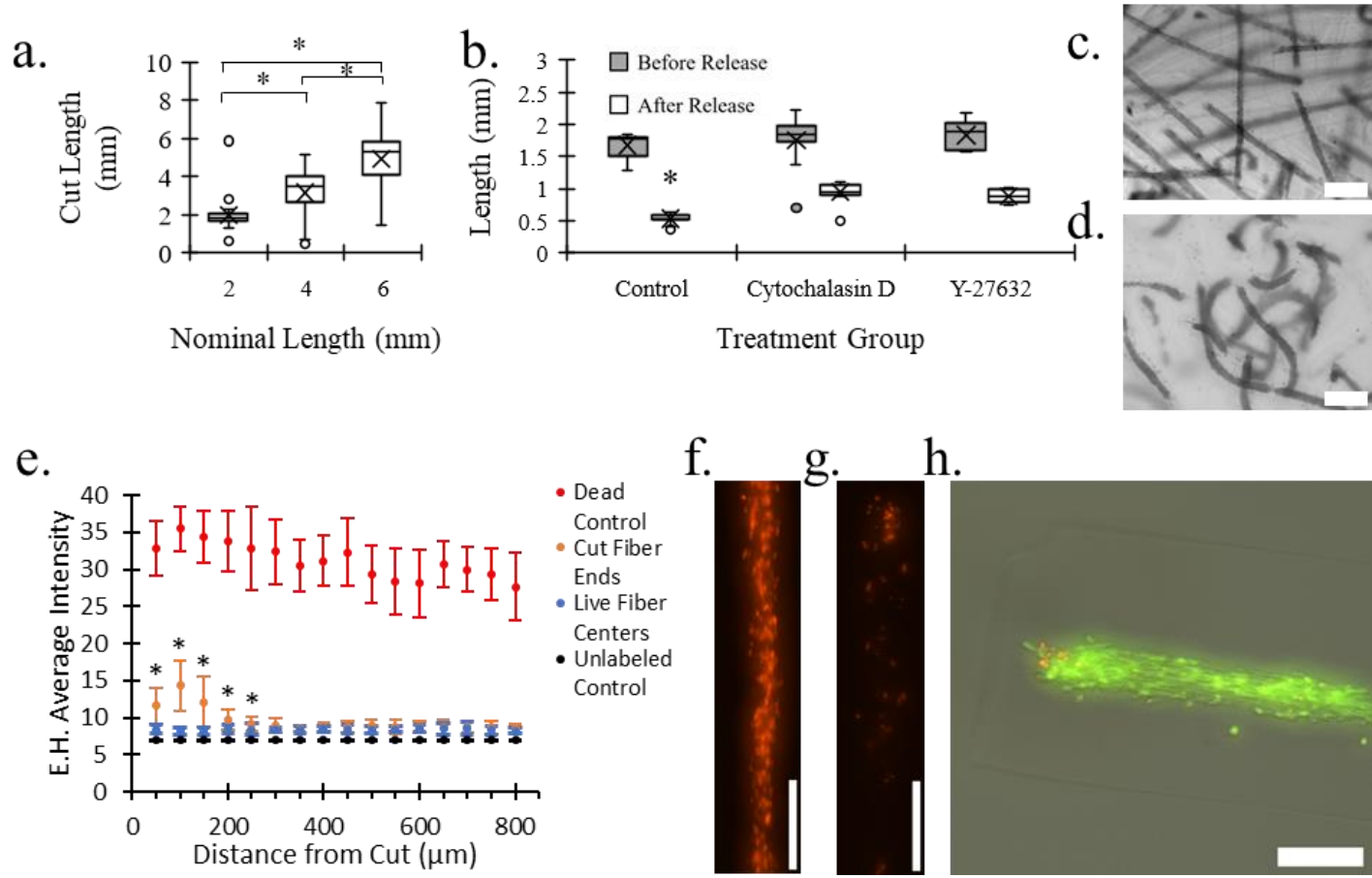


Figure 6-4: Properties of the PAMs after processing.

(a) The cutting guide with razor produces fibers of different lengths depending on the nominal cutting intervals. (b) After cutting, releasing the PAMs from the alginate shell results in contraction, which can be partially ameliorated by cytochalasin D or Y-27632. Representative images of (c) PAMS before release and (d) Y-27632-treated PAMs after release. The cutting process results in moderately increased cell death near the cut compared to the center region of the PAMs. Representative images of (f) methanol-treated dead control and (g) cut fiber end (cut end at top of image) used for quantification. (h) Combination brightfield, ethidium homodimer (red), and calcein AM (green) of PAM before release from alginate shell. (* p-value<.001). Scale bars (c,d) 500 μ m and (f,g,h) 200 μ m.

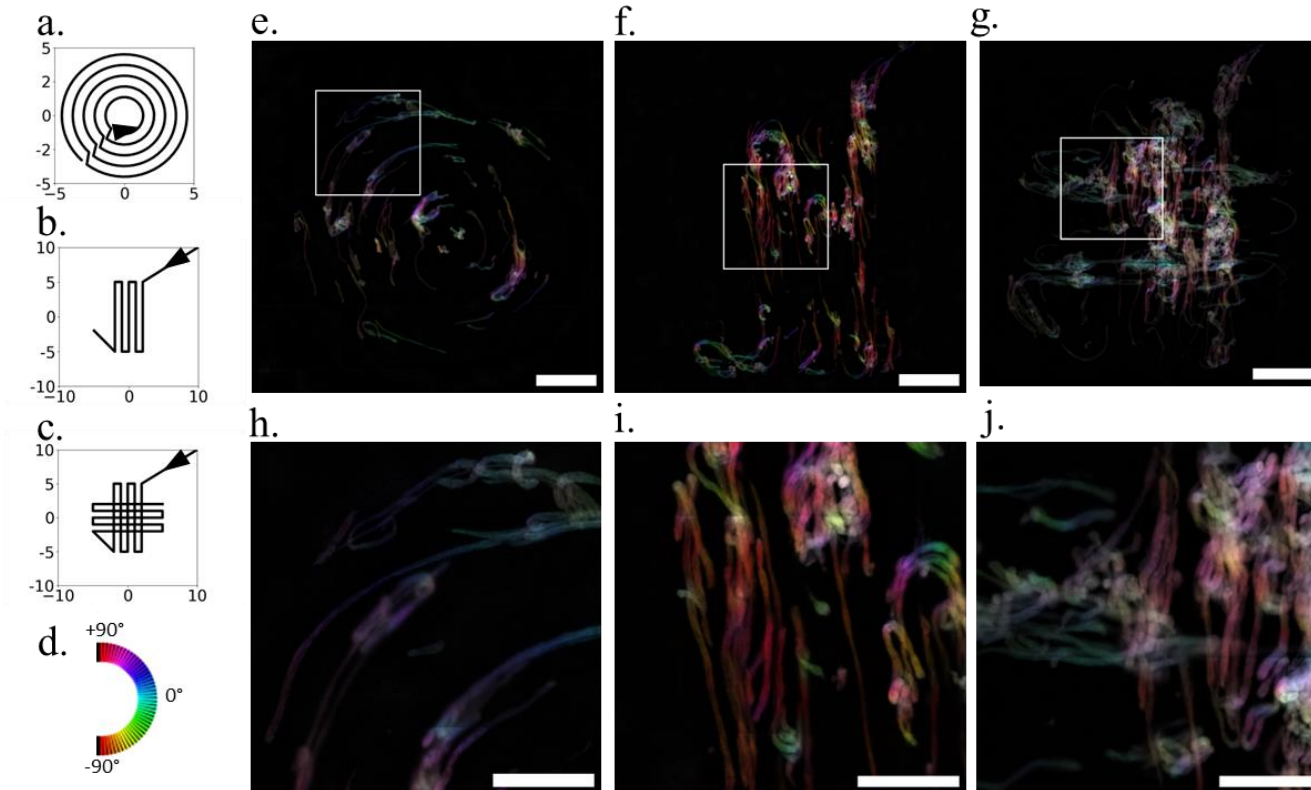


Figure 6-5: Alignment of Bioprinted PAMs.

(a-c) 3D printing paths for (a) circular and (b) one- and (c) 2-layer rectilinear rasters (dimensions in mm, arrow shows start point and print direction). (d) OrientationJ color coding scheme. (e-g) Orientation color-coded images of actin fluorescent images of 3D printed microtissues. (e) circular print (f) single-layer print with y-axis raster (g) two layered print with perpendicular raster pattern, 2mm scale bars. (h-i) inset images with 1 mm scale bars for (e-g), respectively.

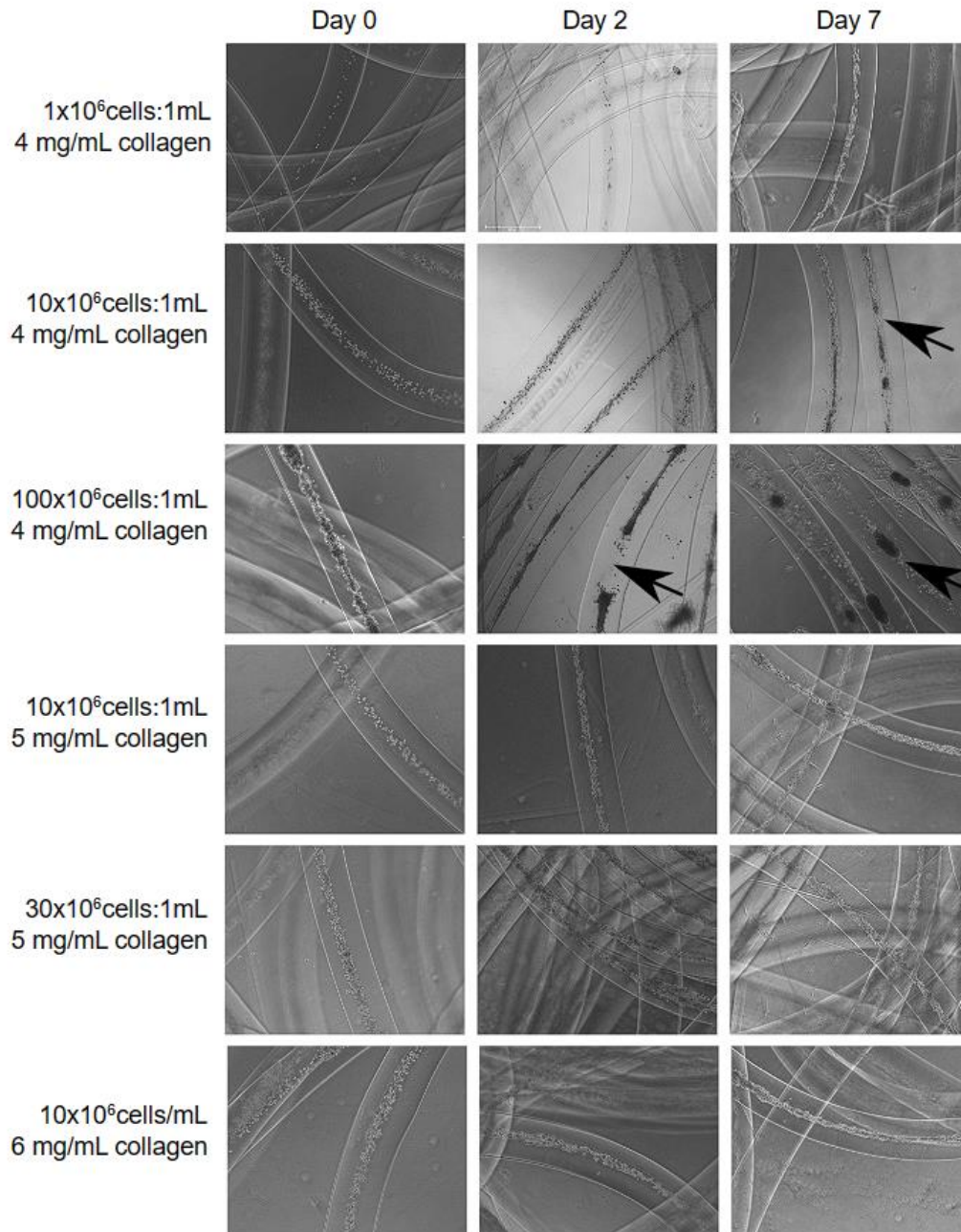


Figure 6-6: Cell and Collagen Concentration Effect on Fiber Morphology.

Phase contrast images taken on EVOS microscope show the structure of the cells within the developing fibers. Arrows point to discontinuities that develop over time in some groups with 4 mg/mL collagen concentrations

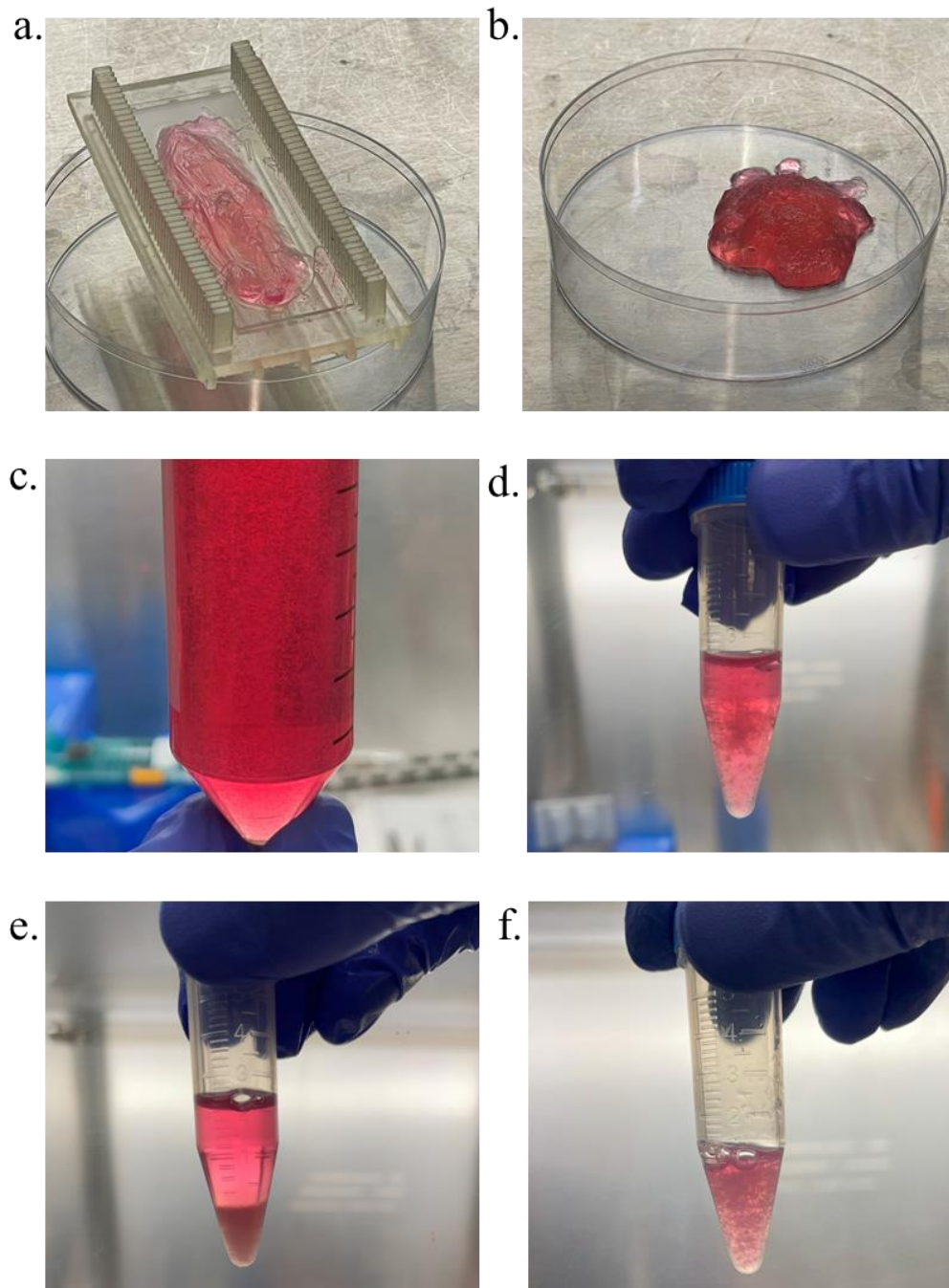


Figure 6-7: Cutting PAMs and Combining with Bioink.

(a) Fibers removed from spool and arranged on cutting frame. (b) fibers post-cutting in 100 mm dish (c) PAMs released from alginate recollected in 50mL tube (d) PAMs transferred to 5 mL tube. (e) PAMs centrifuged for volume measurement. (f) mixing PAMs with bioink.

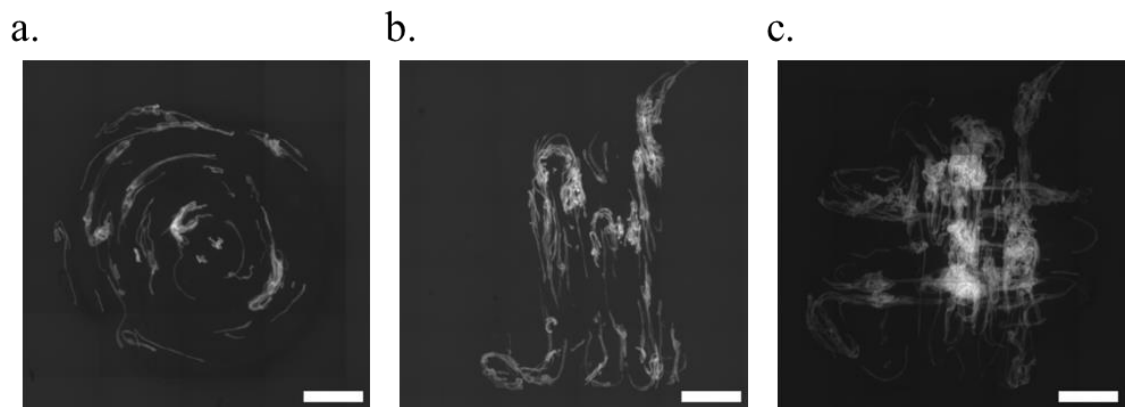


Figure 6-8. Original images of phalloidin-labeled 3D bioprinted constructs.

Stitched field image acquired by EVOS FL Auto 2 prior to background subtraction and OrientationJ alignment analysis.

7 Conclusion

Tissue engineering for the gastroesophageal junction presents both common and unique challenges within the field. To address these, a detailed understanding of the anatomy and physiology within the context of tissue engineering is required. As shown in chapter 2, the vascular supply and interaction of the enteric nervous system with the central nervous system combine with a highly complex muscular structure to allow the coordinated contraction and relaxation of this unique region of human anatomy. Developing tissue-engineered treatments has the potential to positively affect millions of patients with reflux disease, swallowing disorders, and gastric or esophageal cancer.

Very little work has been done to rebuild the GEJ specifically, but a large body of work in engineering the esophagus and other hollow muscular organs provides a base to build upon. In chapter 3, it is shown that a wide range of options exist for future design efforts in terms of material selection, cell source, and engineering strategy. Combination materials of natural and synthetic polymers could provide the structural integrity and biological signaling necessary for reconstitution of the full thickness of the GEJ.

3D bioprinting is expected to play a large role in the future development of these engineered solutions. Chapter 4 highlights the varied modalities that provide a range of manufacturing scales and resolutions and can address different manufacturing challenges. Extrusion bioprinting with hydrogels in particular strikes a balance between manufacturing speed and resolution and is easily combined with other techniques in a larger engineering process.

In this work, a novel approach was developed to combine 3D extrusion bioprinting with pre-aligned muscle microtissues to address the complexity of the muscular structure at the GEJ.

Pre-aligned microtissues made of immortalized esophageal smooth muscle cells can be cut from a fiber made by a core-shell wet spinning technique. These microtissues can be combined with a hydrogel bioink and aligned by flow through a 3D printing nozzle to produce cell alignment in bioprinted constructs that follows the 3D printing path. This method is comparable to a recently published approach by Ahrens *et al.*, where cardiac microtissues were aligned by extrusion bioprinting [239]. However, this new approach to generating PAMs represents a significant improvement in scalability and adjustability due to the rapid and on-demand nature of core-shell fiber wet spinning and the ease of rapid prototyping for the required spinning devices. Furthermore, this dissertation demonstrates the prospect of using PAMs for other types of muscle tissue.

Reproducing the exact structure and function of native tissues and organs is a long term-goal of tissue engineering, and PAM bioprinting is expected to be important for achieving that goal. However, developing the cell sources, integration strategies for the vascular and nervous systems, and path planning for automated manufacturing will likely take decades of additional research. In the short term, it may be possible to treat patients with simpler tissue-engineered constructs that approximate the role of a healthy GEJ. This could serve the dual purpose of alleviating patient suffering while also providing insights into possible surgical approaches for implantation and medical strategies for monitoring the implant. The most basic function of the GEJ is a one-way valve, which might be constructed using currently available tissue-engineering processes. The design could be passive, drawing inspiration from valves found within the cardiovascular system. Such a design would eliminate the need for establishing coordinated muscle movement and innervation, instead only requiring a vascular and lymphatic system for nutrient distribution and fluid transport. The fundamental structure could be composed of non-excitabile cells like fibroblasts for greater simplicity. One requirement will be the establishment of

a protective mucosal barrier, which ideally resembles the mucous producing epithelium of the gastric cardia. A simple tissue engineered GEJ as described would not account for the secondary roles of vomiting and pressure venting through eructation and TLESRs but might be designed in a manner that the one-way valve function could intentionally fail under suitable high stomach pressure.

Future development of PAMs should begin to incorporate other elements necessary for normal tissue function. The immortalized human esophageal smooth muscle cells used in this proof-of concept work are useful for process development but will not be appropriate for patient treatment. Ideally, patient-specific cells would be used to avoid the need for immunosuppressants common with allogeneic transplants. Induced pluripotent stem cells or adipose-derived stem cells have been differentiated into smooth muscle-like phenotypes and are attractive options for future development [242], [243]. The PAM approach could be further improved by incorporating the vascular and nervous systems on the microscale. Pre-vascularized spheroids and organoids have been developed to provide a source for capillary beds in tissue engineered structures [244], [245]. These capillary beds could anastomose with nearby native or engineered medium-sized vessels to reduce time to vascularization and avoid development of an avascular necrotic core inside of thick constructs. It is expected that such pre-vascularization of PAMs could improve their usefulness. Likewise, normal muscle function in the gut is dependent on the enteric nervous system. Including cells like the Interstitial Cells of Cajal might result in a more mature PAM with coordinated smooth muscle contraction and relaxation. Such modifications to the general PAM production method could improve the usefulness of these microtissues as *in vitro* test platforms and *in vivo* treatments.

The wet spinning approach for microtissues alone could allow better *in vitro* models to develop better engineered tissues. As we have demonstrated the ease of rapid prototyping new spinning devices through SLA printing, we expect that the platform could be developed for dynamic mixing of different materials and cells into the core stream to produce mixtures for testing a wide range of parameters in a single strand. If automated cutting systems were developed, these PAMs could also be used for *in vitro* testing of pharmaceuticals. Automated production of short fibers might also be possible through pulsing of the core flow in the spinning device, producing a segmented fiber which would release individual microtissues upon dissolution of the calcium alginate shell.

To realize the full potential of PAM bioprinting, it will be necessary to develop new methods for path planning. Traditional 3D printing relies on intermediate software processing steps to “slice” a computer-designed model into a series of layers along the Z-axis. As discussed in Chapter 2, the orientation of the smooth muscle bundles within the GEJ are not arranged in simple planes, and thus is not amenable to the slicing method of creating Gcode paths. A new approach will be required, possibly using information extracted from diffusion tensor magnetic resonance imaging (DT-MRI) to assemble biologically derived paths for the 3D bioprinter nozzle. Such a strategy could allow the microtissues to be printed in an alignment mimicking the native GEJ structure without manually specifying the printing paths, which might significantly increase the uptake of this new bioprinting approach by the field.

In summary, we have demonstrated that the GEJ is a complicated structure that has been under-investigated in the field of tissue engineering. Creating tissue engineered treatments has the potential to alleviate suffering for large numbers of patients with GEJ dysfunction or esophagectomy, but fully recreating the normal GEJ structure poses some significant challenges.

One key challenge is the complicated structure of the smooth muscle bundles which make up the GEJHPZ. By combining 3D extrusion bioprinting techniques to deposit aligned PAMs, direct writing of this complex alignment could be achieved. Thus, the field of tissue engineering is one step closer to developing treatments for the GEJ.

8 References

- [1] K. Takahashi *et al.*, “Induction of Pluripotent Stem Cells from Adult Human Fibroblasts by Defined Factors,” *Cell*, vol. 131, no. 5, pp. 861–872, Nov. 2007, doi: 10.1016/j.cell.2007.11.019.
- [2] S. Sarkar, M. Dadhania, P. Rourke, T. A. Desai, and J. Y. Wong, “Vascular tissue engineering: Microtextured scaffold templates to control organization of vascular smooth muscle cells and extracellular matrix,” *Acta Biomater.*, vol. 1, no. 1, pp. 93–100, 2005, doi: 10.1016/j.actbio.2004.08.003.
- [3] A. C. Ritchie, S. Wijaya, W. F. Ong, S. P. Zhong, and K. S. Chian, “Dependence of alignment direction on magnitude of strain in esophageal smooth muscle cells,” *Biotechnol Bioeng*, vol. 102, no. a6n, 7502021, pp. 1703–1711, 2009.
- [4] B. Kalman, C. Picart, and T. Boudou, “Quick and easy microfabrication of T-shaped cantilevers to generate arrays of microtissues,” *Biomed. Microdevices*, vol. 18, no. 3, p. 43, Jun. 2016, doi: 10.1007/s10544-016-0067-x.
- [5] A. R. West *et al.*, “Development and characterization of a 3D multicell microtissue culture model of airway smooth muscle,” *Am. J. Physiol.-Lung Cell. Mol. Physiol.*, vol. 304, no. 1, pp. L4–L16, Jan. 2013, doi: 10.1152/ajplung.00168.2012.
- [6] T. Sato and T. Nakamura, “Tissue-engineered airway replacement,” *The Lancet*, vol. 372, no. 9655, pp. 2003–2004, 2008, doi: 10.1016/S0140-6736(08)61599-8.
- [7] J. Pandolfino and A. Gawron, “Achalasia: A systematic review,” *JAMA*, vol. 313, no. 18, pp. 1841–1852, 2015, doi: 10.1001/jama.2015.2996.
- [8] H. B. El-Serag, S. Sweet, C. C. Winchester, and J. Dent, “Update on the epidemiology of gastro-oesophageal reflux disease: a systematic review,” *Gut*, vol. 63, no. 6, pp. 871–880, 2014, doi: 10.1136/gutjnl-2012-304269.
- [9] J. Kramer, M. Shakhathreh, A. Naik, Z. Duan, and H. El-Serag, “Use and yield of endoscopy in patients with uncomplicated gastroesophageal reflux disorder,” *JAMA Intern. Med.*, vol. 174, no. 3, pp. 462–465, 2014, doi: 10.1001/jamainternmed.2013.13015.
- [10] J. C. Flanagan *et al.*, “Esophagectomy and Gastric Pull-through Procedures: Surgical Techniques, Imaging Features, and Potential Complications,” *RadioGraphics*, vol. 36, no. 1, pp. 107–121, Jan. 2016, doi: 10.1148/rg.2016150126.
- [11] L. Haverkamp, M. F. J. Seesing, J. P. Ruurda, J. Boone, and R. van Hillegersberg, “Worldwide trends in surgical techniques in the treatment of esophageal and gastroesophageal junction cancer,” *Dis. Esophagus*, vol. 30, no. 1, pp. 1–7, 2017, doi: 10.1111/dote.12480.
- [12] L. A. Houghton, A. S. Lee, H. Badri, K. R. DeVault, and J. A. Smith, “Respiratory disease and the oesophagus: reflux, reflexes and microaspiration,” *Nat. Rev. Gastroenterol. Hepatol.*, vol. 13, no. 8, pp. 445–460, Aug. 2016, doi: 10.1038/nrgastro.2016.91.
- [13] M. E. Allaix, P. M. Fisichella, I. Noth, F. A. Herbella, B. Borraez Segura, and M. G. Patti, “Idiopathic Pulmonary Fibrosis and Gastroesophageal Reflux. Implications for Treatment,” *J. Gastrointest. Surg.*, vol. 18, no. 1, pp. 100–105, 2014, doi: 10.1007/s11605-013-2333-z.
- [14] B. Z. Atkins *et al.*, “Reducing Hospital Morbidity and Mortality Following Esophagectomy,” *Ann. Thorac. Surg.*, vol. 78, no. 4, pp. 1170–1176, Oct. 2004, doi: 10.1016/j.athoracsur.2004.02.034.

- [15] K. N. Bitar and E. Zakhem, "Bioengineering the gut: future prospects of regenerative medicine," *Nat. Rev. Gastroenterol. Hepatol.*, vol. 13, no. 9, pp. 543–556, Sep. 2016, doi: 10.1038/nrgastro.2016.124.
- [16] M. J. Workman *et al.*, "Engineered human pluripotent-stem-cell-derived intestinal tissues with a functional enteric nervous system," *Nat. Med.*, vol. 23, no. 1, pp. 49–59, Jan. 2017, doi: 10.1038/nm.4233.
- [17] S. F. Badylak, T. Hoppo, A. Nieponice, T. W. Gilbert, J. M. Davison, and B. A. Jobe, "Esophageal Preservation in Five Male Patients After Endoscopic Inner-Layer Circumferential Resection in the Setting of Superficial Cancer: A Regenerative Medicine Approach with a Biologic Scaffold," *Tissue Eng. Part A*, vol. 17, no. 11–12, pp. 1643–1650, Jun. 2011, doi: 10.1089/ten.tea.2010.0739.
- [18] K. S. Dua, W. J. Hogan, A. A. Adam, and M. Gasparri, "In-vivo oesophageal regeneration in a human being by use of a non-biological scaffold and extracellular matrix," *The Lancet*, vol. 388, no. 10039, pp. 55–61, 2016, doi: 10.1016/S0140-6736(15)01036-3.
- [19] K. Kanetaka, S. Kobayashi, and S. Eguchi, "Regenerative medicine for the esophagus," *Surg. Today*, vol. 48, no. 8, pp. 739–747, 2018, doi: 10.1007/s00595-017-1610-y.
- [20] A. Nieponice *et al.*, "Patch esophagoplasty: esophageal reconstruction using biologic scaffolds," *Ann. Thorac. Surg.*, vol. 97, no. 1, pp. 283–288, Jan. 2014, doi: 10.1016/j.athoracsur.2013.08.011.
- [21] T. Ohki *et al.*, "Prevention of Esophageal Stricture After Endoscopic Submucosal Dissection Using Tissue-Engineered Cell Sheets," *Gastroenterology*, vol. 143, no. 3, pp. 582–588.e2, Sep. 2012, doi: 10.1053/j.gastro.2012.04.050.
- [22] R. B. Anderson, D. F. Newgreen, and H. M. Young, "Neural Crest and the Development of the Enteric Nervous System," in *Neural Crest Induction and Differentiation*, J.-P. Saint-Jeannet, Ed., Boston, MA: Springer US, 2006, pp. 181–196. doi: 10.1007/978-0-387-46954-6_11.
- [23] A. Goto *et al.*, "GDNF and Endothelin 3 Regulate Migration of Enteric Neural Crest-Derived Cells via Protein Kinase A and Rac1," *J. Neurosci.*, vol. 33, no. 11, pp. 4901–4912, 2013, doi: 10.1523/JNEUROSCI.4828-12.2013.
- [24] S. Perin, C. J. McCann, O. Borrelli, P. De Coppi, and N. Thapar, "Update on Foregut Molecular Embryology and Role of Regenerative Medicine Therapies," *Front. Pediatr.*, vol. 5, no. 101615492, pp. 1–9, Apr. 2017, doi: 10.3389/fped.2017.00091.
- [25] A. J. Durston, "What are the roles of retinoids, other morphogens, and Hox genes in setting up the vertebrate body axis?," *genesis*, no. 57, p. e23296, Apr. 2019, doi: 10.1002/dvg.23296.
- [26] F. Beck, "Homeobox Genes in Gut Development," *Gut*, vol. 51, no. 3, pp. 450–454, 2002, doi: 10.1136/gut.51.3.450.
- [27] N. Yahagi *et al.*, "Position-specific expression of Hox genes along the gastrointestinal tract," *Congenit. Anom.*, vol. 44, no. 1, pp. 18–26, Mar. 2004, doi: 10.1111/j.1741-4520.2003.00004.x.
- [28] B. M. Carlson, "Digestive and Respiratory Systems and Body Cavities," in *Human Embryology and Developmental Biology*, Cambridge, MA: Elsevier, Inc., 2019, pp. 318–357.e2.
- [29] K. W. McCracken *et al.*, "Wnt/ β -catenin promotes gastric fundus specification in mice and humans," *Nature*, vol. 541, no. 7636, pp. 182–187, Jan. 2017, doi: 10.1038/nature21021.
- [30] S. Hashimoto *et al.*, " β -Catenin-SOX2 signaling regulates the fate of developing airway epithelium," *J. Cell Sci.*, vol. 125, no. 4, pp. 932–942, 2012, doi: 10.1242/jcs.092734.

- [31] L. Raghoebir *et al.*, “SOX2 redirects the developmental fate of the intestinal epithelium toward a premature gastric phenotype,” *J. Mol. Cell Biol.*, vol. 4, no. 6, pp. 377–385, 2012, doi: 10.1093/jmcb/mjs030.
- [32] K. W. McCracken and J. M. Wells, “Mechanisms of embryonic stomach development,” *Semin. Cell Dev. Biol.*, vol. 66, pp. 36–42, 2017, doi: <https://doi.org/10.1016/j.semcd.2017.02.004>.
- [33] S. G. Willet and J. C. Mills, “Stomach Organ and Cell Lineage Differentiation: From Embryogenesis to Adult Homeostasis,” *Cell. Mol. Gastroenterol. Hepatol.*, vol. 2, no. 5, pp. 546–559, 2016, doi: <https://doi.org/10.1016/j.jcmgh.2016.05.006>.
- [34] A. Sukegawa *et al.*, “The concentric structure of the developing gut is regulated by Sonic hedgehog derived from endodermal epithelium,” *Development*, vol. 127, no. 9, pp. 1971–1980, 2000.
- [35] J. Mao, B.-M. Kim, M. Rajurkar, R. A. Shivdasani, and A. P. McMahon, “Hedgehog signaling controls mesenchymal growth in the developing mammalian digestive tract,” *Development*, vol. 137, no. 10, pp. 1721–1729, 2010, doi: 10.1242/dev.044586.
- [36] A. I. Romer, J. Singh, S. Rattan, and R. S. Krauss, “Smooth muscle fascicular reorientation is required for esophageal morphogenesis and dependent on Cdo,” *J. Cell Biol.*, vol. 201, no. 2, pp. 309–323, 2013, doi: 10.1083/jcb.201301005.
- [37] R. S. Krauss, D. Chihara, and A. I. Romer, “Embracing change: striated-for-smooth muscle replacement in esophagus development,” *Skelet. Muscle*, vol. 6, p. 27, 2016, doi: 10.1186/s13395-016-0099-1.
- [38] D. Chihara, A. I. Romer, C. F. Bentzinger, M. A. Rudnicki, and R. S. Krauss, “PAX7 is required for patterning the esophageal musculature,” *Skelet. Muscle*, vol. 5, no. 1, p. 39, Dec. 2015, doi: 10.1186/s13395-015-0068-0.
- [39] R. Londono and S. F. Badylak, “Regenerative Medicine Strategies for Esophageal Repair,” *Tissue Eng. Part B Rev.*, vol. 21, no. 4, pp. 393–410, Aug. 2015, doi: 10.1089/ten.TEB.2015.0014.
- [40] A. D. DeWard, J. Cramer, and E. Lagasse, “Cellular Heterogeneity in the Mouse Esophagus Implicates the Presence of a Nonquiescent Epithelial Stem Cell Population,” *Cell Rep.*, vol. 9, no. 2, pp. 701–711, 2014, doi: <https://doi.org/10.1016/j.celrep.2014.09.027>.
- [41] Y. Van Nieuwenhove, H. Destordeur, and G. Willems, “Spatial Distribution and Cell Kinetics of the Glands in the Human Esophageal Mucosa,” *Eur. J. Morphol.*, vol. 39, no. 3, pp. 163–168, Jul. 2001, doi: 10.1076/ejom.39.3.163.4674.
- [42] Z. M. Stojisic, R. M. Stevanovic, M. M. Stojanovic, A. D. Stanojevic, and D. T. Bacetic, “Histological Features of Gastric Cardia in Adults: an Autopsy and study,” *J. Gastrointest. Liver Dis.*, vol. 20, no. 1, pp. 13–18, 2011.
- [43] G. De Hertogh, P. Van Eyken, N. Ectors, and K. Geboes, “On the origin of cardiac mucosa: A histological and immunohistochemical study of cytokeratin expression patterns in the developing esophagogastric junction region and stomach,” *World J. Gastroenterol.*, vol. 11, no. 29, pp. 4490–4496, 2005, doi: <https://dx.doi.org/10.3748%2Fwjg.v11.i29.4490>.
- [44] A. J. A. Barbosa and R. D. Pereira, “Gastric Cardia and Gastroesophageal Junction — An Ongoing Challenge for the Endoscopist and the Pathologist,” in *Endoscopy - Innovative Uses and Emerging Technologies*, S. Amornyotin, Ed., Rijeka, Croatia: InTechOpen, 2015. doi: 10.5772/60554.
- [45] K. Braden and D. Urma, “Esophagus - anatomy and development,” *GI Motility Online*, 2006. <https://www.nature.com/gimo/contents/pt1/full/gimo6.html>

- [46] D. Liebermann-Meffert, *Pearson's thoracic & esophageal surgery.*, vol. 2. Philadelphia: Churchill Livingstone/Elsevier, 2008.
- [47] R. Maselli *et al.*, "Microvasculature of the esophagus and gastroesophageal junction: Lesson learned from submucosal endoscopy," *World J. Gastrointest. Endosc.*, vol. 8, no. 19, pp. 690–696, Nov. 2016, doi: 10.4253/wjge.v8.i19.690.
- [48] A. Vianna *et al.*, "Normal venous circulation of the gastroesophageal junction," *Gastroenterology*, vol. 93, no. 4, pp. 876–889, Oct. 1987, doi: 10.1016/0016-5085(87)90453-7.
- [49] F. Schlottmann, A. Barbetta, B. Mungo, A. O. Lidor, and D. Molena, "Identification of the Lymphatic Drainage Pattern of Esophageal Cancer with Near-Infrared Fluorescent Imaging," *J. Laparoendosc. Adv. Surg. Tech.*, vol. 27, no. 3, pp. 268–271, Mar. 2017, doi: 10.1089/lap.2016.0523.
- [50] L. Miller, A. Vegesna, M. Ruggieri, and A. Braverman, "Normal and abnormal physiology, pharmacology, and anatomy of the gastroesophageal junction high-pressure zone," *Ann. N. Y. Acad. Sci.*, vol. 1380, no. 1, pp. 48–57, 2016, doi: 10.1111/nyas.13168.
- [51] C. Xie, Y. Li, N. Zhang, L. Xiong, M. Chen, and Y. Xiao, "Gastroesophageal flap valve reflected EGJ morphology and correlated to acid reflux," *BMC Gastroenterol.*, vol. 17, no. 1, pp. 1–8, 2017, doi: 10.1186/s12876-017-0693-7.
- [52] G. Vantrappen, E. C. Texter, C. J. Barborika, and J. Vandenbroucke, "The closing mechanism at the gastroesophageal junction," *Am. J. Med.*, vol. 28, no. 4, pp. 564–577, Apr. 1960, doi: 10.1016/0002-9343(60)90151-0.
- [53] N. Apaydin, A. Uz, A. Elhan, M. Loukas, and R. S. Tubbs, "Does an anatomical sphincter exist in the distal esophagus?," *Surg. Radiol. Anat.*, vol. 30, no. 1, pp. 11–16, 2008, doi: 10.1007/s00276-007-0276-3.
- [54] J. G. Bresseur, R. Ulerich, Q. Dai, D. K. Patel, A. M. S. Soliman, and L. S. Miller, "Pharmacological dissection of the human gastro-oesophageal segment into three sphincteric components," *J. Physiol.*, vol. 580, no. 3, pp. 961–975, 2007, doi: 10.1113/jphysiol.2006.124032.
- [55] D. Liao *et al.*, "3D reconstruction and fiber quantification in the pig lower esophageal sphincter region using in vitro diffusion tensor imaging," *Biomed. Phys. Eng. Express*, vol. 4, no. 2, pp. 1–11, Jan. 2018, doi: 10.1088/2057-1976/aa976e.
- [56] A. Zifan, D. Kumar, L. K. Cheng, and R. K. Mittal, "Three-Dimensional Myoarchitecture of the Lower Esophageal Sphincter and Esophageal Hiatus Using Optical Sectioning Microscopy," *Sci. Rep.*, vol. 7, no. 1, pp. 1–8, Dec. 2017, doi: 10.1038/s41598-017-13342-y.
- [57] D. Liebermann-Meffert, M. Allgower, P. Schmid, and A. L. Blum, "Muscular Equivalent of the Lower Esophageal Sphincter," *Am. Gastroenterol. Assoc.*, vol. 76, no. 1, pp. 31–38, 1979.
- [58] S. Roy, M. R. Fox, J. Curcic, W. Schwizer, and A. Pal, "The gastro-esophageal reflux barrier: biophysical analysis on 3D models of anatomy from magnetic resonance imaging," *Neurogastroenterol. Motil.*, vol. 24, no. 7, pp. 616–e269, Jul. 2012, doi: 10.1111/j.1365-2982.2012.01909.x.
- [59] J. Curcic *et al.*, "Abnormal structure and function of the esophagogastric junction and proximal stomach in gastroesophageal reflux disease.," *Am. J. Gastroenterol.*, vol. 109, no. 5, pp. 658–667, May 2014, doi: 10.1038/ajg.2014.25.
- [60] J. H. Kyung, K. G. Ha, L. N. Kyung, K. Suk, L. B. Eun, and S. G. Am, "Analysis of computed tomographic findings according to gastroesophageal flap valve grade," *Korean J Intern Med*, vol. 33, no. 2, pp. 295–303, 2018, doi: 10.3904/kjim.2016.023.

- [61] I. Hansdotter *et al.*, “Hill classification is superior to the axial length of a hiatal hernia for assessment of the mechanical anti-reflux barrier at the gastroesophageal junction,” *Endosc. Int. Open*, vol. 04, no. 03, pp. E311–E317, Feb. 2016, doi: 10.1055/s-0042-101021.
- [62] A. Gryglewski, I. Z. Pena, K. A. Tomaszewski, and J. A. Walocha, “Unsolved questions regarding the role of esophageal hiatus anatomy in the development of esophageal hiatal hernias,” *Adv. Clin. Exp. Med.*, vol. 23, no. 4, pp. 639–644, 2014, doi: 10.17219/acem/37247.
- [63] N. Apaydin, A. Uz, O. Evirgen, M. Loukas, R. S. Tubbs, and A. Elhan, “The phrenico-esophageal ligament: an anatomical study,” *Surg. Radiol. Anat.*, vol. 30, no. 1, pp. 29–36, Feb. 2008, doi: 10.1007/s00276-007-0279-0.
- [64] T. C. Bombeck, D. H. Dillard, and L. M. Nyhus, “Muscular Anatomy of the Gastroesophageal Junction and Role of the Phrenoesophageal Ligament,” *Ann. Surg.*, vol. 164, no. 4, pp. 643–652, 1966, doi: <https://doi.org/10.1097/00000658-196610000-00011>.
- [65] M. Â. N. e Souza, R. A. Nobre, P. C. Bezerra, A. A. dos Santos, and D. Sifrim, “Anatomical and functional deficiencies of the crural diaphragm in patients with esophagitis,” *Neurogastroenterol. Motil.*, vol. 29, no. 1, pp. 1–8, Jan. 2017, doi: 10.1111/nmo.12899.
- [66] R. Farré and D. Sifrim, “Regulation of basal tone, relaxation and contraction of the lower oesophageal sphincter. Relevance to drug discovery for oesophageal disorders,” *Br. J. Pharmacol.*, vol. 153, no. 5, pp. 858–869, Jan. 2009, doi: 10.1038/sj.bjp.0707572.
- [67] W. L. Neuhuber, M. Raab, J. W. and H. R. Berthoud, “Innervation of the mammalian esophagus,” *Adv. Anat. Embryol. Cell Biol.*, vol. 185, pp. 1–73, back cover, 2006.
- [68] H. Park and J. L. Conklin, “Neuromuscular control of esophageal peristalsis,” *Curr. Gastroenterol. Rep.*, vol. 1, no. 3, pp. 186–197, Jun. 1999, doi: 10.1007/s11894-999-0033-3.
- [69] O. A. Al-Shboul, “The Importance of Interstitial Cells of Cajal in the Gastrointestinal Tract,” *Saudi J Gastroenterol*, vol. 19, no. 1, pp. 3–15, 2013, doi: 10.4103/1319-3767.105909.
- [70] D. Groneberg *et al.*, “Dominant role of interstitial cells of Cajal in nitrergic relaxation of murine lower oesophageal sphincter,” *J. Physiol.*, vol. 593, no. 2, pp. 403–414, 2015, doi: 10.1113/jphysiol.2014.273540.
- [71] P. J. Hornby and T. P. Abrahams, “Central control of lower esophageal sphincter relaxation,” *Am. J. Med.*, vol. 108, no. 4, Supplement 1, pp. 90–98, 2000, doi: [https://doi.org/10.1016/S0002-9343\(99\)00345-9](https://doi.org/10.1016/S0002-9343(99)00345-9).
- [72] N. E. Diamant, “Functional Anatomy and Physiology of Swallowing and Esophageal Motility,” in *The Esophagus*, D. O. Castell, Ed., Oxford, UK: Wiley-Blackwell, 2012, pp. 63–96. doi: 10.1002/9781444346220.ch5.
- [73] R. K. Goyal and A. Chaudhury, “Physiology of normal esophageal motility,” *J. Clin. Gastroenterol.*, vol. 42, no. 5, pp. 610–619, 2008, doi: 10.1097/MCG.0b013e31816b444d.
- [74] G. E. Boeckxstaens, “The lower oesophageal sphincter,” *Neurogastroenterol. Motil.*, vol. 17, no. s1, pp. 13–21, Jun. 2005, doi: 10.1111/j.1365-2982.2005.00661.x.
- [75] A. J. A. J. P. M. S. Bredenoord and A. J. P. M. Smout, “Physiologic and Pathologic Belching,” *Clin. Gastroenterol. Hepatol.*, vol. 5, no. 7, pp. 772–775, 2007, doi: <https://doi.org/10.1016/j.cgh.2007.02.018>.
- [76] S. Sobrino-Cossío *et al.*, “Post-fundoplication symptoms and complications: Diagnostic approach and treatment,” *Rev. Gastroenterol. México Engl. Ed.*, vol. 82, no. 3, pp. 234–247, 2017, doi: <https://doi.org/10.1016/j.rgmexn.2017.02.001>.

- [77] D. J. Mikami and K. M. Murayama, "Physiology and Pathogenesis of Gastroesophageal Reflux Disease," *Surg. Clin. North Am.*, vol. 95, no. 3, pp. 515–525, 2015, doi: 10.1016/j.suc.2015.02.006.
- [78] N. Schaub, K. Ng, P. Kuo, Q. Aziz, and D. Sifrim, "Gastric and lower esophageal sphincter pressures during nausea: a study using visual motion-induced nausea and high-resolution manometry," *Am. J. Physiol.-Gastrointest. Liver Physiol.*, vol. 306, no. 9, pp. G741–G747, 2014, doi: 10.1152/ajpgi.00412.2013.
- [79] C. C. Horn, "The Physiology of Vomiting," in *Nausea and Vomiting*, Cham, Switzerland: Springer International Publishing, 2017, pp. 15–25. doi: 10.1007/978-3-319-34076-0_2.
- [80] M. Mir, M. N. Ali, U. Ansari, and J. Sami, "Structure and motility of the esophagus from a mechanical perspective," *Esophagus*, vol. 13, no. 1, pp. 8–16, May 2015, doi: 10.1007/s10388-015-0497-1.
- [81] S. Brandstaeter, S. L. Fuchs, R. C. Aydin, and C. J. Cyron, "Mechanics of the stomach: A review of an emerging field of biomechanics," *GAMM-Mitteilungen*, vol. 42, no. 3, p. e201900001, Sep. 2019, doi: 10.1002/gamm.201900001.
- [82] G. Sommer *et al.*, "Multiaxial mechanical response and constitutive modeling of esophageal tissues: Impact on esophageal tissue engineering," *Acta Biomater.*, vol. 9, no. 12, pp. 9379–9391, Dec. 2013, doi: 10.1016/j.actbio.2013.07.041.
- [83] R. K. Mittal, A. Zifan, D. Kumar, M. Ledgerwood-Lee, E. Ruppert, and G. Ghahremani, "Functional morphology of the lower esophageal sphincter and crural diaphragm determined by three-dimensional high-resolution esophago-gastric junction pressure profile and CT imaging," *Am. J. Physiol. - Gastrointest. Liver Physiol.*, vol. 313, no. 3, pp. G212–G219, 2017, doi: 10.1152/ajpgi.00130.2017.
- [84] J. Y. Tan, C. K. Chua, K. F. Leong, K. S. Chian, W. S. Leong, and L. P. Tan, "Esophageal tissue engineering: An in-depth review on scaffold design," *Biotechnol. Bioeng.*, vol. 109, no. 1, pp. 1–15, 2012, doi: 10.1002/bit.23323.
- [85] Y. Takeoka *et al.*, "Regeneration of esophagus using a scaffold-free biomimetic structure created with bio-three-dimensional printing," *PLOS ONE*, vol. 14, no. 3, pp. 1–12, Mar. 2019, doi: 10.1371/journal.pone.0211339.
- [86] Y. Nakase *et al.*, "Intrathoracic esophageal replacement by in situ tissue-engineered esophagus.," *J. Thorac. Cardiovasc. Surg.*, vol. 136, no. 4, pp. 850–859, Oct. 2008, doi: 10.1016/j.jtcvs.2008.05.027.
- [87] T. Poghosyan *et al.*, "Circumferential esophageal replacement using a tube-shaped tissue-engineered substitute: An experimental study in minipigs.," *Surgery*, vol. 158, no. 1, pp. 266–277, Jul. 2015, doi: 10.1016/j.surg.2015.01.020.
- [88] H. Nakatsu *et al.*, "Influence of mesenchymal stem cells on stomach tissue engineering using small intestinal submucosa," *J. Tissue Eng. Regen. Med.*, vol. 9, no. 3, pp. 296–304, 2015, doi: 10.1002/term.1794.
- [89] T. Maemura *et al.*, "A Tissue-engineered Stomach Shows Presence of Proton Pump and G-cells in a Rat Model, Resulting in Improved Anemia Following Total Gastrectomy," *Artif. Organs*, vol. 32, no. 3, pp. 234–239, Mar. 2008, doi: 10.1111/j.1525-1594.2007.00528.x.
- [90] T. Maemura, M. Shin, and M. Kinoshita, "Tissue engineering of the stomach," *J. Surg. Res.*, vol. 183, no. 1, pp. 285–295, Jul. 2013, doi: 10.1016/j.jss.2013.02.032.
- [91] S. Bartfeld *et al.*, "In vitro expansion of human gastric epithelial stem cells and their responses to bacterial infection.," *Gastroenterology*, vol. 148, no. 1, pp. 126-136.e6, 2015, doi: 10.1053/j.gastro.2014.09.042.

- [92] S. L. Rego, S. Raghavan, E. Zakhem, and K. N. Bitar, "Enteric neural differentiation in innervated, physiologically functional, smooth muscle constructs is modulated by bone morphogenic protein 2 secreted by sphincteric smooth muscle cells," *J. Tissue Eng. Regen. Med.*, vol. 11, no. 4, pp. 1251–1261, Apr. 2017, doi: 10.1002/term.2027.
- [93] S. L. Rego, E. Zakhem, G. Orlando, and K. N. Bitar, "Bioengineering functional human sphincteric and non-sphincteric gastrointestinal smooth muscle constructs," *Methods*, vol. 99, pp. 128–134, Apr. 2016, doi: 10.1016/j.ymeth.2015.08.014.
- [94] E. Zakhem, M. El Bahrawy, G. Orlando, and K. N. Bitar, "Biomechanical properties of an implanted engineered tubular gut-sphincter complex.," *J. Tissue Eng. Regen. Med.*, vol. 11, no. 12, pp. 3398–3407, Dec. 2017, doi: 10.1002/term.2253.
- [95] S. F. Badylak *et al.*, "Esophageal reconstruction with ECM and muscle tissue in a dog model.," *J Surg Res*, vol. 128, no. 1, pp. 87–97, 2005, doi: 10.1016/j.jss.2005.03.002.
- [96] S. Badylak, S. Meurling, M. Chen, A. Spievack, and A. Simmons-Byrd, "Resorbable bioscaffold for esophageal repair in a dog model," *J. Pediatr. Surg.*, vol. 35, no. 7, pp. 1097–1103, Jul. 2000, doi: <https://doi.org/10.1053/jpsu.2000.7834>.
- [97] M. F. Lopes, A. Cabrita, J. Ilharco, P. Pessa, and J. Patrício, "Grafts of porcine intestinal submucosa for repair of cervical and abdominal esophageal defects in the rat.," *J. Investig. Surg. Off. J. Acad. Surg. Res.*, vol. 19, no. 2, pp. 105–111, Apr. 2006, doi: 10.1080/08941930600569621.
- [98] R.-Q. Wei *et al.*, "Grafts of porcine small intestinal submucosa with cultured autologous oral mucosal epithelial cells for esophageal repair in a canine model.," *Exp. Biol. Med. Maywood NJ*, vol. 234, no. 4, pp. 453–461, Apr. 2009, doi: 10.3181/0901-RM-5.
- [99] H. J. Stein, D. Liebermann-Meffert, T. R. DeMeester, and J. R. Siewert, "Three-dimensional pressure image and muscular structure of the human lower esophageal sphincter," *Surgery*, vol. 117, no. 6, pp. 692–698, 1995, doi: [https://doi.org/10.1016/S0039-6060\(95\)80014-X](https://doi.org/10.1016/S0039-6060(95)80014-X).
- [100] D. Richards, J. Jia, M. Yost, R. Markwald, and Y. Mei, "3D Bioprinting for Vascularized Tissue Fabrication," *Ann. Biomed. Eng.*, vol. 45, no. 1, pp. 132–147, Jan. 2017, doi: 10.1007/s10439-016-1653-z.
- [101] K. S. Chian, M. F. Leong, and K. Kono, "Regenerative medicine for oesophageal reconstruction after cancer treatment," *Lancet Oncol.*, vol. 16, no. 2, pp. e84–e92, Feb. 2015, doi: 10.1016/S1470-2045(14)70410-3.
- [102] E. M. Corsini *et al.*, "Intestinal Metaplasia in the Esophageal Remnant Is Rare After Ivor Lewis Esophagectomy," *J. Gastrointest. Surg.*, vol. 25, no. 9, pp. 2185–2191, Sep. 2021, doi: 10.1007/s11605-021-04909-2.
- [103] C. D. Vogt and A. Panoskaltsis-Mortari, "Tissue engineering of the gastroesophageal junction.," *J. Tissue Eng. Regen. Med.*, vol. 14, no. 6, pp. 855–868, Jun. 2020, doi: 10.1002/term.3045.
- [104] Y. Kawai, R. Takagi, T. Ohki, M. Yamamoto, and M. Yamato, "Evaluation of human keratinocyte sheets transplanted onto porcine excised esophagus after submucosal dissection in an ex vivo model.," *Regen. Ther.*, vol. 15, pp. 323–331, Dec. 2020, doi: 10.1016/j.reth.2020.11.004.
- [105] H. K. Na, J. H. Lee, I. K. Shim, H.-Y. Jung, D. H. Kim, and C. J. Kim, "Allogeneic epithelial cell sheet transplantation for preventing esophageal stricture after circumferential ESD in a porcine model: preliminary results.," *Scand. J. Gastroenterol.*, vol. 56, no. 5, pp. 598–603, May 2021, doi: 10.1080/00365521.2021.1897669.

- [106] T. Ohki *et al.*, “Treatment of oesophageal ulcerations using endoscopic transplantation of tissue-engineered autologous oral mucosal epithelial cell sheets in a canine model,” *Gut*, vol. 55, no. 12, pp. 1704–1710, Dec. 2006, doi: 10.1136/gut.2005.088518.
- [107] N. Yamaguchi *et al.*, “Oral epithelial cell sheets engraftment for esophageal strictures after endoscopic submucosal dissection of squamous cell carcinoma and airplane transportation,” *Sci. Rep.*, vol. 7, no. 1, p. 17460, Dec. 2017, doi: 10.1038/s41598-017-17663-w.
- [108] H. Isomoto, N. Yamaguchi, H. Minami, and K. Nakao, “Management of complications associated with endoscopic submucosal dissection/ endoscopic mucosal resection for esophageal cancer,” *Dig. Endosc. Off. J. Jpn. Gastroenterol. Endosc. Soc.*, vol. 25 Suppl 1, pp. 29–38, Mar. 2013, doi: 10.1111/j.1443-1661.2012.01388.x.
- [109] S. Kobayashi *et al.*, “Prevention of esophageal strictures after endoscopic submucosal dissection,” *World J. Gastroenterol.*, vol. 20, no. 41, pp. 15098–15109, Nov. 2014, doi: 10.3748/wjg.v20.i41.15098.
- [110] R. P. Goyal *et al.*, “Decellularization of caprine esophagus using fruit pericarp extract of *Sapindus mukorossi*,” *Cell Tissue Bank.*, vol. 23, no. 1, pp. 79–92, Mar. 2022, doi: 10.1007/s10561-021-09916-w.
- [111] O. Syed, N. J. Walters, R. M. Day, H.-W. Kim, and J. C. Knowles, “Evaluation of decellularization protocols for production of tubular small intestine submucosa scaffolds for use in oesophageal tissue engineering,” *Acta Biomater.*, vol. 10, no. 101233144, pp. 5043–5054, 2014.
- [112] T. J. Keane *et al.*, “Tissue-Specific Effects of Esophageal Extracellular Matrix,” *Tissue Eng. - Part A*, vol. 21, no. 17–18, pp. 2293–2300, 2015, doi: 10.1089/ten.tea.2015.0322.
- [113] M. I. Bozuk, N. M. Fearing, and P. L. Leggett, “Use of decellularized human skin to repair esophageal anastomotic leak in humans,” *JSLs*, vol. 10, no. 1, pp. 83–85, 2006.
- [114] J. Catry *et al.*, “Circumferential Esophageal Replacement by a Tissue-engineered Substitute Using Mesenchymal Stem Cells: An Experimental Study in Mini Pigs,” *Cell Transpl.*, vol. 26, no. b02, 9208854, pp. 1831–1839, 2017.
- [115] J. A. Isch, S. A. Engum, C. A. Ruble, M. M. Davis, and J. L. Grosfeld, “Patch esophagoplasty using AlloDerm as a tissue scaffold,” *J. Pediatr. Surg.*, vol. 36, no. 2, pp. 266–268, Feb. 2001, doi: 10.1053/jpsu.2001.20685.
- [116] B. Zhang *et al.*, “Acellular Dermal Matrix Prevents Esophageal Stricture After Full Circumferential Endoscopic Submucosal Dissection in a Porcine Model,” *Front. Bioeng. Biotechnol.*, vol. 10, p. 884502, 2022, doi: 10.3389/fbioe.2022.884502.
- [117] P. Kuppan, S. Sethuraman, and U. M. Krishnan, “Interaction of human smooth muscle cells on random and aligned nanofibrous scaffolds of PHBV and PHBV-gelatin,” *Int. J. Polym. Mater. Polym. Biomater.*, vol. 65, no. 16, pp. 816–825, 2016, doi: 10.1080/00914037.2016.1163562.
- [118] P. Kuppan, S. Sethuraman, and U. M. Krishnan, “In vitro co-culture of epithelial cells and smooth muscle cells on aligned nanofibrous scaffolds,” *Mater. Sci. Eng. C Mater. Biol. Appl.*, vol. 81, pp. 191–205, Dec. 2017, doi: 10.1016/j.msec.2017.07.050.
- [119] W. Tian, X. Liu, X. Zhang, T. Bai, and B. Wu, “Self-Assembly of Ultrafine Fibers with Micropores via Cryogenic Electrospinning and Its Potential Application in Esophagus Repair,” *Polymers*, vol. 14, no. 9, May 2022, doi: 10.3390/polym14091924.
- [120] B. Wu, Y. Wu, W. F. Lu, and J. Y. H. Fuh, “Polycaprolactone/Pluronic F127 Tissue Engineering Scaffolds via Electrohydrodynamic Jetting for Gastro Intestinal Repair,” in *Procedia CIRP*, Shih A. and Cao J., Eds., Elsevier B.V., 2017, pp. 184–188. doi: 10.1016/j.procir.2017.04.045.

- [121] L. Meng, M. Frohbergh, M. Villarraga, S. Sundaram, T. Roffidal, and W. Fodor, "Biomechanics of regenerated esophageal tissue following the implantation of a tissue engineered Cellspan(TM) Esophageal Implant.," *J. Biomech.*, vol. 140, p. 111162, Jul. 2022, doi: 10.1016/j.jbiomech.2022.111162.
- [122] Y. J. Tan, W. Y. Yeong, X. Tan, J. An, K. S. Chian, and K. F. Leong, "Characterization, mechanical behavior and in vitro evaluation of a melt-drawn scaffold for esophageal tissue engineering," *J. Mech. Behav. Biomed. Mater.*, vol. 57, no. 101322406, pp. 246–259, Apr. 2016, doi: 10.1016/j.jmbbm.2015.12.015.
- [123] R. Hou *et al.*, "Biological properties of a bionic scaffold for esophageal tissue engineering research.," *Colloids Surf. B Biointerfaces*, vol. 179, pp. 208–217, Jul. 2019, doi: 10.1016/j.colsurfb.2019.03.072.
- [124] L. Hou, J. Jin, J. Lv, L. Chen, Y. Zhu, and X. Liu, "Constitution and in vivo test of micro-porous tubular scaffold for esophageal tissue engineering.," *J Biomater Appl*, vol. 30, no. job, 8813912, pp. 568–578, 2015.
- [125] B. Guo and P. X. Ma, "Synthetic biodegradable functional polymers for tissue engineering: a brief review," *Sci. China Chem.*, vol. 57, no. 4, pp. 490–500, Apr. 2014, doi: 10.1007/s11426-014-5086-y.
- [126] D. Bhattarai, L. Aguilar, C. Park, and C. Kim, "A Review on Properties of Natural and Synthetic Based Electrospun Fibrous Materials for Bone Tissue Engineering," *Membranes*, vol. 8, no. 3, p. 62, Aug. 2018, doi: 10.3390/membranes8030062.
- [127] T. Maemura *et al.*, "Assessment of a tissue-engineered gastric wall patch in a rat model.," *Artif Organs*, vol. 36, no. 8zk, 7802778, pp. 409–417, 2012.
- [128] X. Wang *et al.*, "Differentiation of bMSCs on Biocompatible, Biodegradable, and Biomimetic Scaffolds for Largely Defected Tissue Repair.," *ACS Appl. Bio Mater.*, vol. 3, no. 1, pp. 735–746, Jan. 2020, doi: 10.1021/acsabm.9b01063.
- [129] P. Lynen Jansen, U. Klinge, M. Anurov, S. Titkova, P. R. Mertens, and M. Jansen, "Surgical mesh as a scaffold for tissue regeneration in the esophagus.," *Eur Surg Res*, vol. 36, no. enl, 0174752, pp. 104–111, 2004.
- [130] M. Maeda *et al.*, "Endoscopic cell sheet transplantation device developed by using a 3-dimensional printer and its feasibility evaluation in a porcine model.," *Gastrointest. Endosc.*, vol. 82, no. 1, pp. 147–152, Jul. 2015, doi: 10.1016/j.gie.2015.01.062.
- [131] E.-J. Chung *et al.*, "Development of an omentum-cultured oesophageal scaffold reinforced by a 3D-printed ring: feasibility of an in vivo bioreactor.," *Artif. Cells Nanomedicine Biotechnol.*, vol. 46, pp. 885–895, 2018.
- [132] S. D. Kim *et al.*, "Three-Dimensional Printed Design of Antibiotic-Releasing Esophageal Patches for Antimicrobial Activity Prevention.," *Tissue Eng. Part A*, vol. 27, no. 23–24, pp. 1490–1502, Dec. 2021, doi: 10.1089/ten.TEA.2020.0268.
- [133] W. Kim and G. H. Kim, "3D bioprinting of functional cell-laden bioinks and its application for cell-alignment and maturation," *Appl. Mater. Today*, vol. 19, p. 10588, 2020, doi: doi.org/10.1016/j.apmt.2020.100588.
- [134] H. Park *et al.*, "Experimental investigation of esophageal reconstruction with electrospun polyurethane nanofiber and 3D printing polycaprolactone scaffolds using a rat model.," *Head Neck*, vol. 43, no. 3, pp. 833–848, Mar. 2021, doi: 10.1002/hed.26540.
- [135] S. Y. Park *et al.*, "Tissue-engineered artificial oesophagus patch using three-dimensionally printed polycaprolactone with mesenchymal stem cells: a preliminary report," *Interact. Cardiovasc. Thorac. Surg.*, vol. 22, no. 6, pp. 712–717, Jun. 2016, doi: 10.1093/icvts/ivw048.

- [136] S. Yeleswarapu, S. Chameettachal, and F. Pati, “Integrated 3D Printing-Based Framework-A Strategy to Fabricate Tubular Structures with Mechanocompromised Hydrogels,” *ACS Appl. Bio Mater.*, vol. 4, no. 9, pp. 6982–6992, Sep. 2021, doi: 10.1021/acsabm.1c00644.
- [137] S. Yeleswarapu, S. Chameettachal, A. K. Bera, and F. Pati, “Smooth muscle matrix bioink promotes myogenic differentiation of encapsulated adipose-derived stem cells,” *J. Biomed. Mater. Res. - Part A*, 2022, doi: 10.1002/jbm.a.37433.
- [138] H. Nam *et al.*, “Multi-layered Free-form 3D Cell-printed Tubular Construct with Decellularized Inner and Outer Esophageal Tissue-derived Bioinks,” *Sci. Rep.*, vol. 10, no. 1, p. 7255, Apr. 2020, doi: 10.1038/s41598-020-64049-6.
- [139] D.-H. Ha *et al.*, “Therapeutic effect of decellularized extracellular matrix-based hydrogel for radiation esophagitis by 3D printed esophageal stent,” *Biomaterials*, vol. 266, p. 120477, Jan. 2021, doi: 10.1016/j.biomaterials.2020.120477.
- [140] J. M. Aho *et al.*, “First-in-Human Segmental Esophageal Reconstruction Using a Bioengineered Mesenchymal Stromal Cell-Seeded Implant,” *JTO Clin. Res. Rep.*, vol. 2, no. 9, p. 100216, Sep. 2021, doi: 10.1016/j.jtocrr.2021.100216.
- [141] S. H. Chng and V. Pachnis, “Enteric Nervous System: lessons from neurogenesis for reverse engineering and disease modelling and treatment,” *Curr. Opin. Pharmacol.*, vol. 50, pp. 100–106, Feb. 2020, doi: 10.1016/j.coph.2020.02.001.
- [142] Y. Li *et al.*, “Engineering cell alignment in vitro,” *Biotechnol. Adv.*, vol. 32, no. 2, pp. 347–365, Mar. 2014, doi: 10.1016/j.biotechadv.2013.11.007.
- [143] E. Manousiouthakis *et al.*, “Bioengineered in vitro enteric nervous system,” *J. Tissue Eng. Regen. Med.*, vol. 13, no. 9, pp. 1712–1723, Sep. 2019, doi: 10.1002/term.2926.
- [144] M. E. Prendergast, M. D. Davidson, and J. A. Burdick, “A biofabrication method to align cells within bioprinted photocrosslinkable and cell-degradable hydrogel constructs via embedded fibers,” *Biofabrication*, vol. 13, no. 4, p. 044108, Oct. 2021, doi: 10.1088/1758-5090/ac25cc.
- [145] E. Gong *et al.*, “Efficacy of Endoscopic and Surgical Treatments for Gastroesophageal Reflux Disease: A Systematic Review and Network Meta-Analysis,” *J. Pers. Med.*, vol. 12, no. 4, p. 621, Apr. 2022, doi: 10.3390/jpm12040621.
- [146] N. R. Schiele, D. T. Corr, Y. Huang, N. A. Raof, Y. Xie, and D. B. Chrisey, “Laser-based direct-write techniques for cell printing,” *Biofabrication*, vol. 2, no. 3, 2010, doi: 10.1088/1758-5082/2/3/032001.
- [147] L. E. Bertassoni *et al.*, “Hydrogel bioprinted microchannel networks for vascularization of tissue engineering constructs,” *Lab Chip*, vol. 14, no. 13, pp. 2202–2211, 2014, doi: 10.1039/C4LC00030G.
- [148] W. Jia *et al.*, “Direct 3D bioprinting of perfusable vascular constructs using a blend bioink,” *Biomaterials*, vol. 106, pp. 58–68, 2016, doi: 10.1016/j.biomaterials.2016.07.038.
- [149] A. Lee *et al.*, “3D bioprinting of collagen to rebuild components of the human heart,” *Science*, vol. 365, no. 6452, pp. 482–487, 2019, doi: 10.1126/science.aav9051.
- [150] G. Levenson *et al.*, “Circumferential esophageal replacement by a decellularized esophageal matrix in a porcine model,” *Surgery*, vol. 171, no. 2, pp. 384–392, Feb. 2022, doi: 10.1016/j.surg.2021.07.009.
- [151] G. Luc *et al.*, “Decellularized and matured esophageal scaffold for circumferential esophagus replacement: Proof of concept in a pig model,” *Biomaterials*, vol. 175, pp. 1–18, 2018, doi: 10.1016/j.biomaterials.2018.05.023.
- [152] M. Marzaro *et al.*, “Successful muscle regeneration by a homologous microperforated scaffold seeded with autologous mesenchymal stromal cells in a porcine esophageal

- substitution model,” *Ther. Adv. Gastroenterol.*, vol. 13, no. November 2019, pp. 1–12, 2020, doi: 10.1177/1756284820923220.
- [153] A. Orozco-Vega *et al.*, “Decellularization of porcine esophageal tissue at three diameters and the bioscaffold modification with EETs-ECM gel,” *J. Biomed. Mater. Res. A*, vol. 110, no. 10, pp. 1669–1680, Oct. 2022, doi: 10.1002/jbm.a.37416.
- [154] L. Arakelian *et al.*, “A clinical-grade acellular matrix for esophageal replacement,” *J. Tissue Eng. Regen. Med.*, vol. 13, no. 12, pp. 2191–2203, Dec. 2019, doi: 10.1002/term.2983.
- [155] N. B. Nayakawde, K. Methe, D. Banerjee, M. Berg, G. U. Premaratne, and M. Olausson, “In Vitro Regeneration of Decellularized Pig Esophagus Using Human Amniotic Stem Cells,” *BioResearch Open Access*, vol. 9, no. 1, pp. 22–36, 2020, doi: 10.1089/biores.2019.0054.
- [156] S. Savvidis *et al.*, “Monitoring tissue engineered constructs and protocols with laboratory-based x-ray phase contrast tomography,” *Acta Biomater.*, vol. 141, pp. 290–299, Mar. 2022, doi: 10.1016/j.actbio.2022.01.022.
- [157] S. Sitthisang, M. F. Leong, and K. S. Chian, “Perfusion decellularization of porcine esophagus: Study of two processing factors affecting the folded mucosal structure of the esophageal scaffold,” *J. Biomed. Mater. Res. A*, vol. 109, no. 5, pp. 745–753, May 2021, doi: 10.1002/jbm.a.37060.
- [158] F. Wang, Y. Maeda, V. Zachar, T. Ansari, and J. Emmersen, “Regeneration of the oesophageal muscle layer from oesophagus acellular matrix scaffold using adipose-derived stem cells,” *Biochem Biophys Res Commun*, vol. 503, no. 9y8, 0372516, pp. 271–277, 2018.
- [159] C. Crowley *et al.*, “Non-Invasive Longitudinal Bioluminescence Imaging of Human Mesoangioblasts in Bioengineered Esophagi,” *Tissue Eng. Part C Methods*, vol. 25, no. 2, pp. 103–113, Feb. 2019, doi: 10.1089/ten.TEC.2018.0351.
- [160] S. Eftekharzadeh *et al.*, “Esophagus tissue engineering: from decellularization to in vivo recellularization in two sites,” *Cell Tissue Bank.*, vol. 23, no. 2, pp. 301–312, Jun. 2022, doi: 10.1007/s10561-021-09944-6.
- [161] L. Urbani *et al.*, “Multi-stage bioengineering of a layered oesophagus with in vitro expanded muscle and epithelial adult progenitors,” *Nat. Commun.*, vol. 9, no. 1, p. 4286, Oct. 2018, doi: 10.1038/s41467-018-06385-w.
- [162] N. Hou *et al.*, “Tissue-engineered esophagus: recellular esophageal extracellular matrix based on perfusion-decellularized technique and mesenchymal stem cells,” *Biomed. Mater. Bristol Engl.*, vol. 16, no. 5, Aug. 2021, doi: 10.1088/1748-605X/ac1d3d.
- [163] L. Urbani *et al.*, “Long-term cryopreservation of decellularised oesophagi for tissue engineering clinical application,” *PLoS ONE*, vol. 12, no. 101285081, p. e0179341, 2017.
- [164] T. Doede, M. Bondartschuk, C. Joerck, E. Schulze, and M. Goernig, “Unsuccessful alloplastic esophageal replacement with porcine small intestinal submucosa,” *Artif. Organs*, vol. 33, no. 4, pp. 328–333, Apr. 2009, doi: 10.1111/j.1525-1594.2009.00727.x.
- [165] M. F. Lopes, A. Cabrita, J. Ilharco, P. Pessa, and J. Patrício, “Grafts of porcine intestinal submucosa for repair of cervical and abdominal esophageal defects in the rat,” *J. Investig. Surg. Off. J. Acad. Surg. Res.*, vol. 19, no. 2, pp. 105–111, Apr. 2006, doi: 10.1080/08941930600569621.
- [166] B. Tan *et al.*, “Tissue engineered esophagus by mesenchymal stem cell seeding for esophageal repair in a canine model,” *J Surg Res*, vol. 182, no. k7b, 0376340, pp. 40–48, 2013.

- [167] R.-Q. Wei *et al.*, “Grafts of Porcine Small Intestinal Submucosa with Cultured Autologous Oral Mucosal Epithelial Cells for Esophageal Repair in a Canine Model,” *Exp. Biol. Med.*, vol. 234, no. 4, pp. 453–461, Apr. 2009, doi: 10.3181/0901-RM-5.
- [168] A. Nieponice, T. W. Gilbert, S. A. Johnson, N. J. Turner, and S. F. Badylak, “Bone marrow-derived cells participate in the long-term remodeling in a mouse model of esophageal reconstruction,” *J. Surg. Res.*, vol. 182, no. 1, pp. e1-7, Jun. 2013, doi: 10.1016/j.jss.2012.09.029.
- [169] Y. Urita *et al.*, “Regeneration of the esophagus using gastric acellular matrix: an experimental study in a rat model,” *Pediatr Surg Int*, vol. 23, no. cq0, 8609169, pp. 21–26, 2007.
- [170] S. La Francesca *et al.*, “Long-term regeneration and remodeling of the pig esophagus after circumferential resection using a retrievable synthetic scaffold carrying autologous cells,” *Sci. Rep.*, vol. 8, no. 1, p. 4123, Mar. 2018, doi: 10.1038/s41598-018-22401-x.
- [171] T. Jensen, H. Wanczyk, I. Sharma, A. Mitchell, W. N. Sayej, and C. Finck, “Polyurethane scaffolds seeded with autologous cells can regenerate long esophageal gaps: An esophageal atresia treatment model,” *J Pediatr Surg*, no. jmj, 0052631, 2018, [Online]. Available: <http://ovidsp.ovid.com/ovidweb.cgi?T=JS&PAGE=reference&D=medp&NEWS=N&AN=30429066>
- [172] S. Sundaram *et al.*, “Esophageal regeneration following surgical implantation of a tissue engineered esophageal implant in a pediatric model,” *NPJ Regen. Med.*, vol. 7, no. 1, p. 1, Jan. 2022, doi: 10.1038/s41536-021-00200-9.
- [173] S. Pisani *et al.*, “Engineered Full Thickness Electrospun Scaffold for Esophageal Tissue Regeneration: From In Vitro to In Vivo Approach,” *Pharmaceutics*, vol. 14, no. 2, Jan. 2022, doi: 10.3390/pharmaceutics14020252.
- [174] S. Pisani *et al.*, “Tissue Engineered Esophageal Patch by Mesenchymal Stromal Cells: Optimization of Electrospun Patch Engineering,” *Int. J. Mol. Sci.*, vol. 21, no. 5, Mar. 2020, doi: 10.3390/ijms21051764.
- [175] O. Syed *et al.*, “SIS/aligned fibre scaffold designed to meet layered oesophageal tissue complexity and properties,” *Acta Biomater.*, vol. 99, pp. 181–195, Nov. 2019, doi: 10.1016/j.actbio.2019.08.015.
- [176] P. Kuppan, S. Sethuraman, and U. M. Krishnan, “Poly(3-hydroxybutyrate-co-3-hydroxyvalerate)-based nanofibrous scaffolds to support functional esophageal epithelial cells towards engineering the esophagus,” *J. Biomater. Sci. Polym. Ed.*, vol. 25, no. 6, pp. 574–593, 2014, doi: 10.1080/09205063.2014.884427.
- [177] T. Jensen *et al.*, “Biomimetic and synthetic esophageal tissue engineering,” *Biomaterials*, vol. 57, no. a4p, 8100316, pp. 133–141, 2015, doi: <https://doi.org/10.1016/j.biomaterials.2015.04.004>.
- [178] J. Lv, L. Chen, Y. Zhu, L. Hou, and Y. Liu, “Promoting epithelium regeneration for esophageal tissue engineering through basement membrane reconstitution,” *ACS Appl Mater Interfaces*, vol. 6, no. 101504991, pp. 4954–4964, 2014.
- [179] E.-J. Chung, H. W. Ju, H. J. Park, and C. H. Park, “Three-layered scaffolds for artificial esophagus using poly(ϵ -caprolactone) nanofibers and silk fibroin: An experimental study in a rat model,” *J Biomed Mater Res A*, vol. 103, no. 101234237, pp. 2057–2065, 2015.
- [180] P. Diemer, S. Markoew, D. Q. S. Le, and N. Qvist, “Poly- ϵ -caprolactone mesh as a scaffold for in vivo tissue engineering in rabbit esophagus,” *Dis. Esophagus Off. J. Int. Soc. Dis. Esophagus*, vol. 28, no. 3, pp. 240–245, Apr. 2015, doi: 10.1111/dote.12172.

- [181] B. Wu *et al.*, “Pluronic F127 blended polycaprolactone scaffolds via e-jetting for esophageal tissue engineering.,” *J Mater Sci Mater Med*, vol. 29, no. 9013087, p. 140, 2018.
- [182] O. Cesur *et al.*, “Enhancing esophageal repair with bioactive bilayer mesh containing FGF.,” *Sci. Rep.*, vol. 11, no. 1, p. 19203, Sep. 2021, doi: 10.1038/s41598-021-98840-w.
- [183] Q. Wei *et al.*, “The growth and pluripotency of mesenchymal stem cell on the biodegradable polyurethane synthesized with ferric catalyst.,” *J. Biomater. Sci. Polym. Ed.*, vol. 29, no. 10, pp. 1095–1108, Jul. 2018, doi: 10.1080/09205063.2018.1426424.
- [184] K. Algarrahi *et al.*, “Bi-layer silk fibroin grafts support functional tissue regeneration in a porcine model of onlay esophagoplasty.,” *J. Tissue Eng. Regen. Med.*, vol. 12, no. 2, pp. e894–e904, Feb. 2018, doi: 10.1002/term.2402.
- [185] G. Gundogdu *et al.*, “Evaluation of Bilayer Silk Fibroin Grafts for Tubular Esophagoplasty in a Porcine Defect Model.,” *Tissue Eng. Part A*, vol. 27, no. 1–2, pp. 103–116, Jan. 2021, doi: 10.1089/ten.TEA.2020.0061.
- [186] K. Algarrahi *et al.*, “Bilayer silk fibroin grafts support functional oesophageal repair in a rodent model of caustic injury.,” *J. Tissue Eng. Regen. Med.*, vol. 12, no. 2, pp. e1068–e1075, Feb. 2018, doi: 10.1002/term.2434.
- [187] R. Dorati *et al.*, “Design of a Bioabsorbable Multilayered Patch for Esophagus Tissue Engineering.,” *Macromol Biosci*, vol. 17, no. 101135941, 2017, [Online]. Available: <http://ovidsp.ovid.com/ovidweb.cgi?T=JS&PAGE=reference&D=medc&NEWS=N&AN=28128890>
- [188] R. G. Spurrier, A. L. Speer, X. Hou, W. N. El-Nachef, and T. C. Grikscheit, “Murine and human tissue-engineered esophagus form from sufficient stem/progenitor cells and do not require microdesigned biomaterials.,” *Tissue Eng Part A*, vol. 21, no. 101466659, pp. 906–915, 2015, doi: 10.1089/ten.tea.2014.0357.
- [189] H. R. Hoogenkamp *et al.*, “Seamless vascularized large-diameter tubular collagen scaffolds reinforced with polymer knittings for esophageal regenerative medicine.,” *Tissue Eng. Part C Methods*, vol. 20, no. 5, pp. 423–430, May 2014, doi: 10.1089/ten.TEC.2013.0485.
- [190] F. G. Sala, S. M. Kunisaki, E. R. Ochoa, J. Vacanti, and T. C. Grikscheit, “Tissue-engineered small intestine and stomach form from autologous tissue in a preclinical large animal model.,” *J Surg Res*, vol. 156, no. k7b, 0376340, pp. 205–212, 2009.
- [191] T. Maemura, M. Shin, M. Sato, H. Mochizuki, and J. P. Vacanti, “A tissue-engineered stomach as a replacement of the native stomach.,” *Transplantation*, vol. 76, no. wej, 0132144, pp. 61–65, 2003.
- [192] T. Maemura, K. Ogawa, M. Shin, H. Mochizuki, and J. P. Vacanti, “Assessment of tissue-engineered stomach derived from isolated epithelium organoid units,” *Transplant. Proc.*, vol. 36, no. 5, pp. 1595–1599, Jun. 2004, doi: 10.1016/j.transproceed.2004.05.020.
- [193] T. Maemura, M. Shin, O. Ishii, H. Mochizuki, and J. P. Vacanti, “Initial assessment of a tissue engineered stomach derived from syngeneic donors in a rat model.,” *ASAIO J*, vol. 50, no. bbh, 9204109, pp. 468–472, 2004.
- [194] J. M. Lee, S. L. Sing, M. Zhou, and W. Y. Yeong, “3D bioprinting processes: A perspective on classification and terminology,” *Int. J. Bioprinting*, vol. 4, no. 2, pp. 1–10, 2018, doi: 10.18063/IJB.v4i2.151.
- [195] R. Mhanna and A. Hasan, “1 . 2 Clinical Need for Tissue Engineering,” pp. 3–34, 2017.
- [196] T. Jiang, J. G. Munguia-Lopez, S. Flores-Torres, J. Kort-Mascort, and J. M. Kinsella, “Extrusion bioprinting of soft materials: An emerging technique for biological model fabrication,” *Appl. Phys. Rev.*, vol. 6, no. 1, 2019, doi: 10.1063/1.5059393.

- [197] L. Ning *et al.*, “Process-induced cell damage: pneumatic versus screw-driven bioprinting,” *Biofabrication*, vol. 12, no. 2, 2020, doi: 10.1088/1758-5090/ab5f53.
- [198] Q. Pi *et al.*, “Digitally Tunable Microfluidic Bioprinting of Multilayered Cannular Tissues,” *Adv Mater*, vol. 30, no. 43, p. 1706913, 2018.
- [199] C. Colosi *et al.*, “Microfluidic Bioprinting of Heterogeneous 3D Tissue Constructs Using Low-Viscosity Bioink,” *Adv. Mater.*, vol. 28, no. 4, pp. 677–684, Jan. 2016, doi: 10.1002/adma.201503310.
- [200] M. A. Skylar-Scott, J. Mueller, C. W. Visser, and J. A. Lewis, “Voxelated soft matter via multimaterial multinozzle 3D printing,” *Nature*, vol. 575, no. 7782, pp. 330–335, 2019, doi: 10.1038/s41586-019-1736-8.
- [201] X. Li *et al.*, “Inkjet Bioprinting of Biomaterials,” *Chem. Rev.*, vol. 120, no. 19, pp. 10793–10833, 2020, doi: 10.1021/acs.chemrev.0c00008.
- [202] H. Gudapati, M. Dey, and I. Ozbolat, “A comprehensive review on droplet-based bioprinting: Past, present and future,” *Biomaterials*, vol. 102, pp. 20–42, 2016, doi: 10.1016/j.biomaterials.2016.06.012.
- [203] H. Ebrahimi Orimi, S. S. Hosseini Kolkooh, E. Hooker, S. Narayanswamy, B. Larrivé, and C. Boutopoulos, “Drop-on-demand cell bioprinting via Laser Induced Side Transfer (LIST),” *Sci. Rep.*, vol. 10, no. 1, pp. 1–9, 2020, doi: 10.1038/s41598-020-66565-x.
- [204] M. S. Onses, E. Sutanto, P. M. Ferreira, A. G. Alleyne, and J. A. Rogers, “Mechanisms, Capabilities, and Applications of High-Resolution Electrohydrodynamic Jet Printing,” *Small*, vol. 11, no. 34, pp. 4237–4266, 2015, doi: 10.1002/smll.201500593.
- [205] B. R. Ringeisen, C. M. Othon, J. A. Barron, D. Young, and B. J. Spargo, “Jet-based methods to print living cells,” *Biotechnol. J.*, vol. 1, no. 9, pp. 930–948, 2006, doi: 10.1002/biot.200600058.
- [206] D. J. Odde and M. J. Renn, “Laser-guided direct writing for applications in biotechnology,” *Trends Biotechnol.*, vol. 17, no. 10, pp. 385–389, 1999, doi: 10.1016/S0167-7799(99)01355-4.
- [207] Y. Nahmias and D. J. Odde, “Micropatterning of living cells by laser-guided direct writing: Application to fabrication of hepatic-endothelial sinusoid-like structures,” *Nat. Protoc.*, vol. 1, no. 5, pp. 2288–2296, 2006, doi: 10.1038/nprot.2006.386.
- [208] B. Grigoryan *et al.*, “Multivascular networks and functional intravascular topologies within biocompatible hydrogels,” *Science*, vol. 364, no. 6439, pp. 458–464, 2019, doi: 10.1126/science.aav9750.
- [209] X. Ma *et al.*, “Deterministically patterned biomimetic human iPSC-derived hepatic model via rapid 3D bioprinting,” *Proc. Natl. Acad. Sci. U. S. A.*, vol. 113, no. 8, pp. 2206–2211, 2016, doi: 10.1073/pnas.1524510113.
- [210] A. K. Miri *et al.*, “Microfluidics-Enabled Multimaterial Maskless Stereolithographic Bioprinting,” *Adv. Mater.*, vol. 30, no. 27, pp. 1–9, 2018, doi: 10.1002/adma.201800242.
- [211] K. Parkatzidis, M. Chatzinikolaidou, M. Kaliva, A. Bakopoulou, M. Farsari, and M. Vamvakaki, “Multiphoton 3D Printing of Biopolymer-Based Hydrogels,” *ACS Biomater. Sci. Eng.*, vol. 5, no. 11, pp. 6161–6170, 2019, doi: 10.1021/acsbiomaterials.9b01300.
- [212] R. M. Samsonraj, M. Raghunath, V. Nurcombe, J. H. Hui, A. J. van Wijnen, and S. M. Cool, “Concise Review: Multifaceted Characterization of Human Mesenchymal Stem Cells for Use in Regenerative Medicine,” *STEM CELLS Transl. Med.*, vol. 6, no. 12, pp. 2173–2185, Dec. 2017, doi: 10.1002/sctm.17-0129.
- [213] E.-J. Chung *et al.*, “Development of an omentum-cultured oesophageal scaffold reinforced by a 3D-printed ring: feasibility of an in vivo bioreactor,” *Artif. Cells Nanomedicine*

- Biotechnol.*, vol. 46, no. sup1, pp. 885–895, Oct. 2018, doi: 10.1080/21691401.2018.1439039.
- [214] M. Domingos *et al.*, “Improved osteoblast cell affinity on plasma-modified 3-D extruded PCL scaffolds,” *Acta Biomater.*, vol. 9, no. 4, pp. 5997–6005, 2013.
- [215] L. Y. Santiago, R. W. Nowak, J. Peter Rubin, and K. G. Marra, “Peptide-surface modification of poly(caprolactone) with laminin-derived sequences for adipose-derived stem cell applications,” *Biomaterials*, vol. 27, no. 15, pp. 2962–2969, May 2006.
- [216] L. R. Madden *et al.*, “Bioprinted 3D Primary Human Intestinal Tissues Model Aspects of Native Physiology and ADME/Tox Functions,” *iScience*, vol. 2, pp. 156–167, 2018.
- [217] M. Yan, P. L. Lewis, and R. N. Shah, “Tailoring nanostructure and bioactivity of 3d-printable hydrogels with self-assemble peptides amphiphile (pa) for promoting bile duct formation,” *Biofabrication*, vol. 10, no. 3, 2018.
- [218] D. J. Griffiths, “Flow of Urine Through the Ureter: A Collapsible, Muscular Tube Undergoing Peristalsis,” *J. Biomech. Eng.*, vol. 111, no. 3, pp. 206–211, 1989.
- [219] Š. Polák, S. Žiaran, J. Mištinová, K. Bevízová, L. Danišovič, and I. Varga, “Options for histological study of the structure and ultrastructure of human urinary bladder epithelium,” *Biologia (Bratisl.)*, vol. 67, no. 5, pp. 1018–1025, Jan. 2012, doi: 10.2478/s11756-012-0090-1.
- [220] W. K. Ovalle and P. C. Nahirney, “Netter’s Essential Histology .” Saunders , pp. 357–380, 2013.
- [221] O. Lam Van Ba, S. Aharony, O. Loutochin, and J. Corcos, “Bladder tissue engineering: A literature review,” *Adv. Drug Deliv. Rev.*, vol. 82–83, pp. 31–37, 2015.
- [222] M. Sloff, V. Simaioforidis, R. de Vries, E. Oosterwijk, and W. Feitz, “Tissue Engineering of the Bladder--Reality or Myth? A Systematic Review,” *J. Urol.*, vol. 192, no. 4, pp. 1035–1042, 2014.
- [223] K. Zhang *et al.*, “3D bioprinting of urethra with PCL/PLCL blend and dual autologous cells in fibrin hydrogel: An in vitro evaluation of biomimetic mechanical property and cell growth environment,” *Acta Biomater.*, vol. 50, pp. 154–164, 2017.
- [224] T. Imamura *et al.*, “Biofabricated Structures Reconstruct Functional Urinary Bladders in Radiation-Injured Rat Bladders,” *Tissue Eng. Part A*, vol. 24, no. 21–22, pp. 1574–1587, 2018.
- [225] K. Hölzl, S. Lin, L. Tytgat, S. Van Vlierberghe, L. Gu, and A. Ovsianikov, “Bioink properties before, during and after 3D bioprinting,” *Biofabrication*, vol. 8, no. 3, 2016, doi: 10.1088/1758-5090/8/3/032002.
- [226] C. Mandrycky, Z. Wang, K. Kim, and D. H. Kim, “3D bioprinting for engineering complex tissues,” *Biotechnol. Adv.*, vol. 34, no. 4, pp. 422–434, 2016, doi: 10.1016/j.biotechadv.2015.12.011.
- [227] J. M. Lee and W. Y. Yeong, “Design and Printing Strategies in 3D Bioprinting of Cell-Hydrogels: A Review,” *Adv. Healthc. Mater.*, vol. 5, no. 22, pp. 2856–2865, 2016, doi: 10.1002/adhm.201600435.
- [228] C. Vogt, I. Diaz-Gutierrez, and A. Panoskaltis-Mortari, “The gastroesophageal junction – A gap in tissue engineering,” *J. Immunol. Regen. Med.*, vol. 20, p. 100073, May 2023, doi: 10.1016/j.regen.2023.100073.
- [229] A. Fedorov *et al.*, “3D Slicer as an image computing platform for the Quantitative Imaging Network,” *Magn. Reson. Imaging*, vol. 30, no. 9, pp. 1323–1341, Nov. 2012, doi: 10.1016/j.mri.2012.05.001.
- [230] “3D Slicer Image Computing Platform,” Nov. 22, 2022. <https://www.slicer.org/> (accessed Jun. 19, 2023).

- [231] “CloudCompare.” Jul. 14, 2022. [Online]. Available: <http://www.cloudcompare.org/>
- [232] E. Nürnberg *et al.*, “Routine Optical Clearing of 3D-Cell Cultures: Simplicity Forward,” *Front. Mol. Biosci.*, vol. 7, no. February, pp. 1–19, 2020, doi: 10.3389/fmolb.2020.00020.
- [233] Z. Galliger, C. D. Vogt, H. R. Helms, and A. Panoskaltis-Mortari, “Extracellular Matrix Microparticles Improve GelMA Bioink Resolution for 3D Bioprinting at Ambient Temperature,” *Macromol. Mater. Eng.*, vol. 307, no. 10, p. 2200196, Oct. 2022, doi: 10.1002/mame.202200196.
- [234] B. A. Nerger, P. T. Brun, and C. M. Nelson, “Microextrusion printing cell-laden networks of type i collagen with patterned fiber alignment and geometry,” *Soft Matter*, vol. 15, no. 28, pp. 5728–5738, 2019, doi: 10.1039/c8sm02605j.
- [235] H. Kim *et al.*, “Shear-induced alignment of collagen fibrils using 3D cell printing for corneal stroma tissue engineering,” *Biofabrication*, vol. 11, no. 3, p. 035017, Jul. 2019, doi: 10.1088/1758-5090/ab1a8b.
- [236] A. Ahmed *et al.*, “Local extensional flows promote long-range fiber alignment in 3D collagen hydrogels,” *Biofabrication*, vol. 14, no. 3, p. 035019, Jul. 2022, doi: 10.1088/1758-5090/ac7824.
- [237] Y. Li *et al.*, “3D Prestress Bioprinting of Directed Tissues,” *Adv. Healthc. Mater.*, p. 2301487, Jun. 2023, doi: 10.1002/adhm.202301487.
- [238] B. Kessel, M. Lee, A. Bonato, Y. Tinguely, E. Tosoratti, and M. Zenobi-Wong, “3D Bioprinting of Macroporous Materials Based on Entangled Hydrogel Microstrands,” *Adv. Sci.*, vol. 7, no. 18, p. 2001419, Sep. 2020, doi: 10.1002/advs.202001419.
- [239] J. H. Ahrens *et al.*, “Programming Cellular Alignment in Engineered Cardiac Tissue via Bioprinting Anisotropic Organ Building Blocks,” *Adv. Mater.*, vol. 34, no. 26, p. 2200217, Jul. 2022, doi: 10.1002/adma.202200217.
- [240] A. Y. Hsiao *et al.*, “Smooth muscle-like tissue constructs with circumferentially oriented cells formed by the cell fiber technology,” *PLoS ONE*, vol. 10, no. 3, pp. 1–16, 2015, doi: 10.1371/journal.pone.0119010.
- [241] J. H. Kim *et al.*, “3D Bioprinted Human Skeletal Muscle Constructs for Muscle Function Restoration,” *Sci. Rep.*, vol. 8, no. 1, pp. 1–15, 2018, doi: 10.1038/s41598-018-29968-5.
- [242] M. Stephenson, D. H. Reich, and K. R. Boheler, “Induced pluripotent stem cell-derived vascular smooth muscle cells,” *Vasc. Biol.*, vol. 2, no. 1, pp. R1–R15, Jan. 2020, doi: 10.1530/VB-19-0028.
- [243] M. Shen, T. Quertermous, M. P. Fischbein, and J. C. Wu, “Generation of Vascular Smooth Muscle Cells From Induced Pluripotent Stem Cells: Methods, Applications, and Considerations,” *Circ. Res.*, vol. 128, no. 5, pp. 670–686, Mar. 2021, doi: 10.1161/CIRCRESAHA.120.318049.
- [244] N. S. Rossen *et al.*, “Injectable Therapeutic Organoids Using Sacrificial Hydrogels,” *iScience*, vol. 23, no. 5, p. 101052, May 2020, doi: 10.1016/j.isci.2020.101052.
- [245] L. De Moor *et al.*, “High-throughput fabrication of vascularized spheroids for bioprinting,” *Biofabrication*, vol. 10, no. 3, p. 35009, 2018, doi: 10.1088/1758-5090/aac7e6.